Radio Science Bulletin

ISSN 1024-4530

INTERNATIONAL
UNION OF
RADIO SCIENCE

UNION
RADIO-SCIENTIFIQUE
INTERNATIONALE

Prof. Em. K. ITO
Balthasar Van der Pol
Gold Medal

Prof. S. MACI
John Howard Dellinger
Gold Medal

Prof. R.B. HORNE
Appleton Prize

Prof. J. VOLAKIS
Booker Gold
Medal

Dr. R. MITTRA
Karl Rawer
Gold Medal

Prof. R. HE
Issac Koga
Gold Medal

Dr. X. XU
Santimay Basu
Prize

Prof. K. KOBAYASHI
President's Award

Vol. 2020, No. 374
September 2020

URSI, c/o Ghent University (INTEC)
Technologiepark - Zwijnaarde 126, B-9052 Gent (Belgium)

Contents

Front cover: At the XXXIVth URSI General Assembly and Scientific Symposium in Rome (Italy) this August, the scientists whose pictures are featured on the front cover will be presented with the URSI Awards. For more informatin, please turn to page 100 of this Bulletin.

Radio Science Bulletin Staff

Editor

W. R. Stone
Stoneware Limited
840 Armada Terrace
San Diego, CA 92106, USA
Tel: +1-619 222 1915, Fax: +1-619 222 1606
E-mail: r.stone@ieee.org

Editor-in-Chief

P. Van Daele
URSI Secretariat
Ghent University - INTEC
Technologiepark - Zwijnaarde 126
B-9052 Gent, BELGIUM
Tel: +32 9-264 33 20, Fax: +32 9-264 42 88
E-mail: Pet.VanDaele@UGent.be

Production Editor

I. Lievens
URSI Secretariat / Ghent University - INTEC
Technologiepark - Zwijnaarde 126
B-9052 Gent, BELGIUM
Tel: +32 9-264.33.20, Fax: +32 9-264.42.88
E-mail: ingeursi@ugent.be, info@ursi.org

Senior Associate Editors

A. Pellinen-Wannberg
Department of Physics
Umea University
BOX 812
SE-90187 Umea, SWEDEN
Tel: +46 90 786 74 92, Fax: +46 90 786 66 76
E-mail: asta.pellinen-wannberg@umu.se

O. Santolik
Institute of Atmospheric Physics
Academy of Sciences of the Czech Republic
Bocni II
1401, 141 31 Prague 4, CZECH REPUBLIC
Tel: +420 267 103 083, Fax +420 272 762 528
E-mail os@ufa.cas.cz, santolik@gmail.com

Associate Editors, Commissions

Commission A

Nuno Borges Carvalho
Instituto de Telecomunicaçoes
Universidade de Aveiro, Campus Universitario
3810-193 Aveiro, Portugal
Tel: +351 234377900, Fax: +351 234377901
E-mail: nbcarvalho@ua.pt

Pedro Miguel Cruz
Rua Sao Sebastiao
n34 Hab 33
4520-250 Santa Maria da Feira, Aveiro, PORTUGAL
Tel: +351 225898410
E-mail: pedro.cruz@controlar.pt

Tian Hong Loh
National Physical Laboratory
Hampton Road
Teddington TW11 0LW, United Kingdom
Tel: +44 020 8943 6508
E-mail: tian.loh@npl.co.uk

Nosherwan Shoaib
School of Electrical Engineering and Computer Science (SEECS)
National University of Sciences and Technology (NUST)
NUST Campus H-12, Islamabad, Pakistan
Tel: 051 90852561
E-mail: nosherwan.shoaib@seccs.edu.pk

Commission B

Andrea Michel
Department of Information Engineering
Università di Pisa
Pisa, Italy
E-mail: andrea.michel@iet.unipi.it

John Volakis
College of Engineering and Computing
Florida International University
10555 W. Flagler Street, EC2477
Miami, FL 33174, USA
Tel: +1 305 348 2807
E-mail: jvolakis@fiu.edu

Commission C

Yves Louet
CS 47601, SUPELEC
Avenue de Boulaie
F-35576 Cesson-Sévigné, France
Tel: +33 2 99 84 45 34, Fax: +33 2 99 84 45 99
E-mail: yves.louet@supelec.fr

Commission D

Naoki Shinohara
RISH
Kyoto University
Uji 611-0011, Japan
Tel: +81 774 38 3807 Fax: +81 774 31 8463
E-mail: shino@rish.kyoto-u.ac.jp

Commission E

Virginie Deniau
IFSTTAR
20. rue Elisée Reclus BP 70317
F-59666 Villeneuve d'Ascq Cedex, France
Tel: +33 03 20438991
E-mail: virginie.deniau@ifsttar.fr

Commission F

Haonan Chen
Earth System Research lab, Physical Sciences Division
NOAA
325 Broadway, Boulder, CO 80305, USA
Tel: +1 303 497 4616
E-mail: haonan.chen@noaa.gov

Tullio Tanzi
Télécom ParisTech - LabSoC, c/o EURECOM
Campus SophiaTech Les Templiers
450 route des Chappes 06410 Biot, FRANCE
Tel: +33 0 4 93008411, Fax: 33 0 493008200
E-mail: tullio.tanzi@telecom-paristech.fr

Commission G

Giorgiana De Franceschi
Dept. Arenonomy, Istituto Nazionale di Geofi sica e Vulcanology
Via di Vigna, Murata 605
00 143 Roma, Italy
Tel: +39 06 51860307, Fax: +39 06 51860397
E-mail: giorgiana.defranceschi@ingv.it

Commission H

Jyrki Manninen
Sodankylä Geophysical Observatory
Tähteläntie 62
FIN-99600 Sodanskylä, Finland
Tel: +358 400 151503, Fax +358 16 610248
E-mail: Jyrki.Manninen@oulo.fi

Commission J

Jacob W. Baars
Max Planck Institute for Radio Astronomy
Auf dem Hügel 69
53121 Bonn, Germany
Tel: +49 228 525303
E-mail: jacobbaars@arcor.de

Commission K

Kensuke Sasaki
Applied EM Research Institute
NICT
Koganei, Tokyo, Japan
E-mail: k_sasaki@nict.go.jp

Associate Editors, Columns

Book Reviews

G. Trichopoulos
Electrical, Computer & Energy Engineering ISTB4 555D
Arizona State University
781 E Terrace Road, Tempe, AZ, 85287 USA
Tel: +1 (614) 364-2090
E-mail: gtrichop@asu.edu

Historical Papers

J. D. Mathews
Communications and Space Sciences Lab (CSSL)
The Pennsylvania State University
323A, EE East
University Park, PA 16802-2707, USA
Tel: +1(814) 777-5875, Fax: +1 814 863 8457
E-mail: JDMathews@psu.edu

Et Cetera

T. Akgül
Dept. of Electronics and Communications Engineering
Telecommunications Division
Istanbul Technical University
80626 Maslak Istanbul, TURKEY
Tel: +90 212 285 3605, Fax: +90 212 285 3565
E-mail: tayfunakgul@itu.edu.tr.

Women in Radio Science

A. Pellinen-Wannberg
Department of Physics and Swedish Institute of Space Physics
Umeå University
S-90187 Umeå, Sweden
Tel: +46 90 786 7492
E-mail: asta.pellinen-wannberg@umu.se

Ethically Speaking

R. L. Haupt
Colorado School of Mines
Brown Building 249
1510 Illinois Street, Golden, CO 80401 USA
Tel: +1 (303) 273 3721
E-mail: rhaupt@mines.edu

A. J. Shockley
E-mail: aj4317@gmail.com

Solution Box

Ö. Ergül
Department of Electrical and Electronics Engineering
Middle East Technical University
TR-06800, Ankara, Turkey
E-mail: ozgur.ergul@eee.metu.edu.tr

Telecommunications Health & Safety

J. C. Lin
University of Illinois at Chicago
851 South Morgan Street, M/C 154
Chicago, IL 60607-7053 USA
Tel: +1 312 413 1052, Fax: +1 312 996 6465
E-mail: lin@uic.edu

Historical Column

G. Pelosi
Department of Information Engineering
University of Florence
Via di S. Marta, 3, 50139 Florence, Italy
E-mail: giuseppe.pelosi@unifi.it

Early Career Representative Column

S. J. Wijnholds
Netherlands Institute for Radio Astronomy
Oude Hoogeveensedijk 4
7991 PD Dwingeloo, The Netherlands
E-mail: wijnholds@astron.nl

Education Column

Madhu Chandra
Microwave Engineering and Electromagnetic Theory
Technische Universität Chemnitz
Reichenhainerstrasse 70
09126 Germany
E-mail: madhu.chandra@etit.tu-chemnitz.de

URSI Officers and Secretariat

Current Officers triennium 2017-2020

President

M. Ando
Senior Executive Director
National Institute of Technology
701-2, Higashi Asakawa, Hachioji,
Tokyo 193-0834, Japan
Tel:+81-42-662-3123,
Fax: +81-42-662-3131
E-mail: ando@kosen-k.go.jp,
mando@antenna.ee.titech.ac.jp

Vice President

O. Santolik
Institute of Atmospheric Physics
Electrical Eng. Dept
Academy of Sciences of the Czech Republic
Bocni II, 1401
141 31 Prague 4, CZECH REPUBLIC
Tel: +420 267 103 083
Fax: 420 272 762 528
E-mail: os@ufa.cas.cz, santolik@gmail.com

Past President

P. S. Cannon
Gisbert Kapp Building
University of Birmingham
Edgbaston , Birmingham, B15 2TT,
UNITED KINGDOM
Tel: +44 (0) 7990 564772
Fax: +44 (0)121 414 4323
E-mail: p.cannon@bham.ac.uk

Vice President

A. Sihvola
Electronic Science Department
Aalto University
School of Electrical Engineering
PO Box 13000
FI-00076 AALTO
FINLAND
Tel: +358 50 5871286
E-mail: Ari.Sihvola@aalto.fi

Secretary General

P. Van Daele
URSI Secretariat
Ghent University - INTEC
Technologiepark - Zwijnaarde 126
B-9052 Gent
BELGIUM
Tel: +32 9-264 33 20
Fax: +32 9-264 42 88
E-mail: Pet.VanDaele@UGent.be

Vice President

P. L. E. Uslenghi
Dept. of ECE (MC 154)
University of Illinois at Chicago 851
S. Morgan Street
Chicago, IL 60607-7053
USA
Tel: +1 312 996-6059
Fax: +1 312 996 8664
E-mail: uslenghi@uic.edu

Vice President

W. Baan
Astron
Asserweg 45
9411 LP Beilen
THE NETHERLANDS
Tel: +31 521-595 773/100
Fax: +31 521-595 101
E-mail: baan@astron.nl

URSI Secretariat

Secretary General

P. Van Daele
URSI Secretariat
Ghent University - INTEC
Technologiepark - Zwijnaarde 126
B-9052 Gent
BELGIUM
Tel: +32 9-264 33 20
Fax: +32 9-264 42 88
E-mail: Pet.VanDaele@UGent.be

Assistant Secretary General AP-RASC

K. Kobayashi
Dept. of Electr and Commun. Eng,
Chuo University
1-13-27 Kasuga, Bunkyo-ku
Tokyo, 112-8551, JAPAN
Tel: +81 3 3817 1846/69
Fax: +81 3 3817 1847
E-mail: kazuya@tamacc.chuo-u.ac.jp

Assistant Secretary General

Stefan J. Wijnholds
Netherlands Institute for
Radio Astronomy
Oude Hoogeveensedijk 4
7991 PD Dwingeloo
The Netherlands
E-mail: wijnholds@astron.nl

Executive Secretary

I. Heleu
URSI Secretariat
Ghent University - INTEC
Technologiepark - Zwijnaarde 126
B-9052 Gent
BELGIUM
Tel. +32 9-264.33.20
Fax +32 9-264.42.88
E-mail info@ursi.org

Assistant Secretary General Publications & GASS

W. R. Stone
840 Armada Terrace
San Diego, CA 92106
USA
Tel: +1-619 222 1915
Fax: +1-619 222 1606
E-mail: r.stone@ieee.org

Administrative Secretary

I. Lievens
URSI Secretariat
Ghent University - INTEC
Technologiepark - Zwijnaarde 126
B-9052 Gent
BELGIUM
Tel: +32 9-264.33.20
Fax: +32 9-264.42.88
E-mail: ingeursi@ugent.be

Editor's Comments

W. Ross Stone
Stoneware Limited
840 Armada Terrace
San Diego, CA 92106, USA
Tel: +1-619 222 1915, Fax: +1-619 222 1606
E-mail: r.stone@ieee.org

Special Section on EMTS 2019 Young Scientist Award Papers

This issue of the *URSI Radio Science Bulletin* contains papers by six of the 20 Young Scientist Awardees from the Commission B triennial Electromagnetic Theory Symposium, held May 27-31, 2019, in San Diego, California, USA. The guest Editors for this special section are Kazuya Kobayashi, the Chair of URSI Commission B, and Sembiam Rengarajan, Chair of the EMTS 2019 Local Organizing Committee and Chair of the US Committee for URSI. Their efforts are greatly appreciated.

Note that in all cases, the Young Scientist awardee is the first author of each of the following papers.

A dual-polarized high-gain planar antenna usually requires multiple complex feeding networks. The paper by Yue Li describes a method of using magnetic-current arrays to achieve dual-polarized, high-gain, low-profile antennas using higher-order-mode microstrip antennas without a complex feeding network. The theory and design of these antennas is described. Two prototype antennas were built using this approach, and impressive results were achieved. As an example, a dual-polarized 36-element (3×6×2) magnetic-current array antenna with a simple differential feed was implemented within a total size of $2.92\,\lambda_0 \times 2.92\,\lambda_0 \times 0.085\,\lambda_0$. It achieved a maximum gain of 15.5 dBi within an operating bandwidth of 12.39 GHz to 12.68 GHz.

Designing an efficient, compact circularly polarized cylindrical waveguide feed horn antenna is a challenge. Ghanshyam Mishra, Satish Sharma, and Jia-Chi Chieh describe a new approach for such an antenna, based on building the polarizer into the horn using nine pairs of circular cavities to generate circular polarization. The theory and design of the feed horn is described. A prototype was built, and used with a 10-cm-diameter offset parabolic reflector having an $f/D = 0.25$. The whole feed/reflector assembly was integrated inside a 1U volume of a 6U-CubeSat chassis.

Alessio Monti, Andrea Alù, Alessandro Toscano, and Filiberto Bilotti describe a metasurface as "an extremely thin layer supporting electric and magnetic current densities that introduce an abrupt change in the amplitude and phase of the transmitted and reflected electromagnetic field." Their paper presents a review of their recent results on both the theoretical modeling and practical applications of such surfaces, focusing in particular on optical metasurfaces made of arrays of spheroidal nanoparticles. They provide an excellent and easily understood introduction to the electromagnetics of such surfaces, and explain how the properties of such surfaces can be modeled. They then look at applications including the cancellation of scattering and perfect absorption, and the use of such surfaces as perfect optical mirrors.

The paper by Grigorii A. Ptitcyn, Mohammad Mirmoosa, Viktar Asadchy, and Sergei Tretyakov provides a fascinating examination of the limits of energy storage and controlled energy release in a circuit. The authors consider the energy stored in reactive elements connected to a time-harmonic source after steady state is reached. Assuming the system to be lossless, they show that that using a time-varying load it is possible to control reflected waves and accumulate electromagnetic energy without limit. They also show that proper choice of the time-varying load permits release of the stored energy in the form of an arbitrarily shaped pulse.

"Same Frequency – Simultaneous Transmit and Receive" (SF-STAR) allows for concurrent transmission and reception of RF signals across the entire available bandwidth to double throughput and significantly increase spectrum utilization. A major challenge in implementing SF-STAR is the required very high isolation between the collocated transmitter and receiver. The paper by Satheesh Bojja Venkatakrishnan, Alexander Hovsepian, and John Volakis presents an interference-cancellation circuit that works with any antenna to provide the needed high degree of cancellation across relatively wide bandwidths. The approach works with both single-antenna and dual-antenna

systems. Cancellation of 60 dB across a bandwidth of 400 MHz was demonstrated, and the authors believe the system should be capable of achieving ~100 dB or more across a 1 GHz bandwidth.

Being able to simultaneously and independently control the amplitude, phase, and polarization modulation of an electromagnetic wave interacting with a metasurface would enable tremendous flexibility in the application of metasurfaces. The paper by He-Xiu Xu, Menghua Jiang, Guangwei Hu, Lei Han, Ying Li, and Cheng-Wei Qiu describes a novel method of achieving such control. The design is based on vertical-mode cross-coupling for polarization control, and spatial variations in the orientation and structure of split-ring resonators to achieve independent amplitude and phase modulation. The approach was demonstrated by designing and building two dual-focus metalenses.

Our Other Contributions

You will note that two of the papers in this issue deal with metasurfaces. George Trichopoulos has provided us with a very timely review of the book, *Surface Electromagnetics With Applications in Antennas, Microwave, and Optical Engineering*, edited by Fan Yang and Yahya Rahmat-Samii. This is obviously a very current topic in radio science, and this book is a good resource in the field.

Tayfun Akgul is still dealing with the pandemic in his Et Cetera column. I appreciate his efforts to bring some smiles amidst all the gloom.

Each triennium, the scientific Commissions of URSI provide reports of their activities for the past triennium. The reports of Commissions D and J appear in this issue.

Stefan Wijnholds has provided a report on the activities of the Early Career Representatives Committee. This includes a discussion of the Young Scientist Awards and Student Paper Competition at the GASS 2020, along with lists of the recipients of the awards in both of those events.

Randy Haupt and Amy Shockley take a look at sliver linings in the Ethically Speaking column. It's a timely topic.

Heinrich Hertz provided experimental evidence of the existence of electromagnetic waves in a laboratory setting, and Guglielmo Marconi used those waves in radio links. Giuseppe Pelosi's Historical Corner presents an article by Stefano Maddio and Stefano Selleri that compares the equipment they used, and provides some calculations of the basic operating parameters of their apparatus. I think you'll find this fascinating reading.

Özgür Ergül's Solution Box column brings a contribution by Özgür Eriş and Özgür Ergül that considers electromagnetic interactions with near-zero-index triangular prisms. The geometries and wavelengths involved make this a computationally complex problem, and also produce some very interesting results.

Jim Lin's Telecommunications Health and Safety column looks at what today's news is calling the "Havana Syndrome." This is a set of very serious physiological symptoms first reported by diplomats stationed in Havana. Some of the major symptoms involve auditory effects. This column looks at the reasons why these may well could have been produced by pulsed microwave radiation.

Asta Pellinen Wannberg's Women in Radio Science column looks at the life and career (to date) of Nicole Meyer-Vernet. She tells a fascinating story of (as she characterizes it) freedom, research, and serendipity. I think you'll enjoy reading this.

URSI GASS 2021

The URSI General Assembly and Scientific Symposium will be held August 28-September 4, 2021, in Rome, Italy, at the Sapienza Faculty of Engineering. This will be a on-site conference, with provision for online participation and presentations. Full information is available at the Web site: www.ursi2021.org.

Correction

In the paper by Valentina Palazzi, "Phase-Controlled Beamforming Network Intended for Conformal Arrays," which appeared in the *Radio Science Bulletin* No. 373, June 2020, pp. 12-21, the wrong figures were published for two of the figures. The correct figures and their captions appear below. The *Bulletin* regrets the errors.

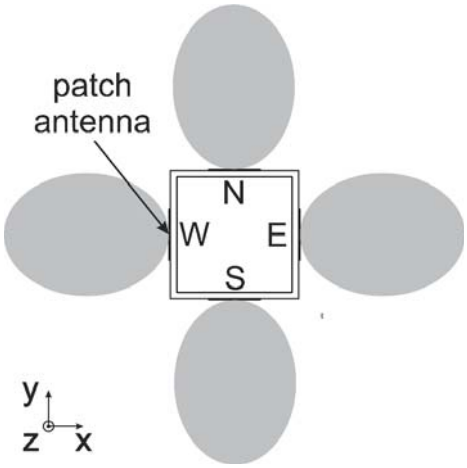

Figure 1a. A sketch of the proposed antenna system: radiation patterns (in gray) generated by single radiating elements. The four radiating elements are marked with their corresponding cardinal directions: N, E, S, and W.

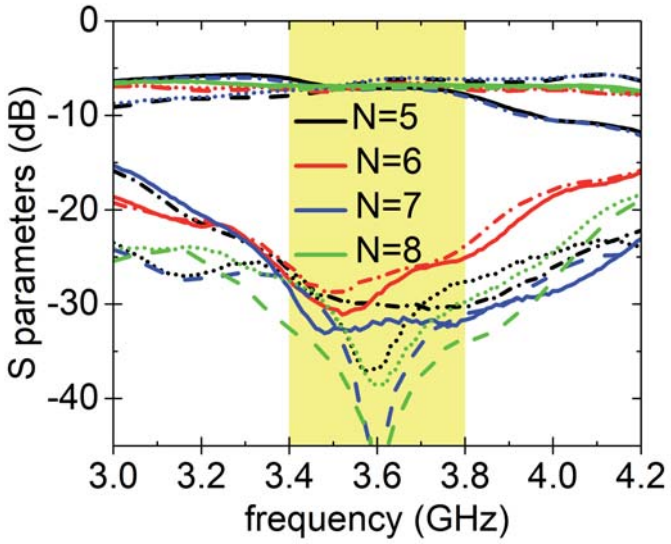

Figure 6c. The magnitude of the transmission coefficients of the complete 1 × 4 network as functions of frequency for the cases $N = 5,...,8$. The plots shows measurement. The solid line refers to $|S_{21}|$, the dashed line to $|S_{31}|$, the dotted line to $|S_{41}|$, and the dashed dotted line to $|S_{51}|$ (after [13]).

Dual-Polarized Magnetic-Current Array Antennas with High Gain and Low Profile

Yue Li

Department of Electronic Engineering
Tsinghua University
Beijing 100084, China (CIE)
E-mail: lyee@tsinghua.edu.cn

Abstract

Two sets of feeding networks are usually needed to achieve a dual-polarized high-gain planar antenna, not only leading to a complicated configuration but also to reduced efficiency. A simple feed structure and strategy are therefore in high demand for dual-polarized high-gain planar antennas. Directed at this requirement, we first present a series-fed dual-polarized slot array with a single-layered substrate. Two orthogonal magnetic-current arrays were positioned at the opposite sides of a single-layered substrate, leading to high gain and high port isolation. A novel scheme to achieve dual-polarized, high-gain, and low-profile antennas using the higher-order-mode microstrip antenna was then demonstrated. By loading half-wavelength slots at the electric-field nulls of a higher-order-mode microstrip antenna, a multiple-element in-phase magnetic-current array was constructed within a low-profile cavity with a simple feeding strategy. As a proof of the concept, two dual-polarized high-gain microstrip magnetic-current array antennas, utilizing the TM_{50} and TM_{90} modes of a microstrip antenna were investigated. These magnetic-current array antennas had the merits of having a low profile, simple feeding, and high isolation, promising a huge potential in diversity and MIMO applications.

1. Introduction

Fifth-generation (5G) communication has raised increasing demands on the capacity, reliability, and spectrum efficiency of wireless-communication systems [1-3]. Under this scenario, antennas with dual-polarized operation are drawing great interest, because of their capability to boost the data transmission rate and to better resist multipath fading via polarization diversity [4]. Different types of dual-polarized antennas have been reported in the literature, including crossed dipoles [5-7], magneto-electric dipoles [8-10], slot antennas [11, 12], and microstrip antennas [13-17]. The key point to designing a dual-polarized antenna lies in keeping high isolation between the two excitation ports, which benefits the polarization purity. Another aspect favored by modern antenna systems is high-gain performance that can be employed to compensate for path loss and add coverage range [17-22]. An antenna with high directivity can also be employed in satellite-to-ground communications [23, 24] and radar systems [25]. Furthermore, in the emerging technique of massive MIMO, a high-gain antenna array or lens serves the purpose of directing the beam to different sectors [26].

Nevertheless, there still remain great challenges in realizing high-gain antennas with dual-polarization operation. To a large extent, this stems from the high insertion loss and prohibitive cost of the complex feeding networks. Additionally, traditional schemes for arranging the radiating apertures and feeding lines at different layers [27-30] inevitably yield high profiles and inconvenience for integration with planar circuits. To address these thorny problems, we suggest a new scheme [31-33]: magnetic-current arrays, which offer dual-polarized and high-gain performance on single-layer substrates. In previous work [32], two orthogonally placed E-shaped slot arrays were series fed by coplanar waveguides connected to the same ground, while in [33] and [34] the high-order mode of a thin cavity was employed to excite the in-phase radiation of a magnetic-current array. Decent isolation levels between two polarizations were realized via the proper arrangement of radiating elements or feed lines. With compact structures and robust performance, the proposed magnetic-current arrays may open a new horizon for dual-polarized and high-gain antennas deployed in high-speed reliable wireless communications.

2. Dual-Polarized Magnetic-Current Array Antenna Using Series-Fed Slot Array

In this section, a dual-polarized slot antenna array etched on only a single layer of substrate is described, capable of being two-dimensionally scaled [32]. The geometry of this array is shown in Figure 1a. Two identical single-polarized slot arrays were arranged orthogonally on two sides of the substrate layer, which are represented in the figure by two different colors. Each row of elements on the

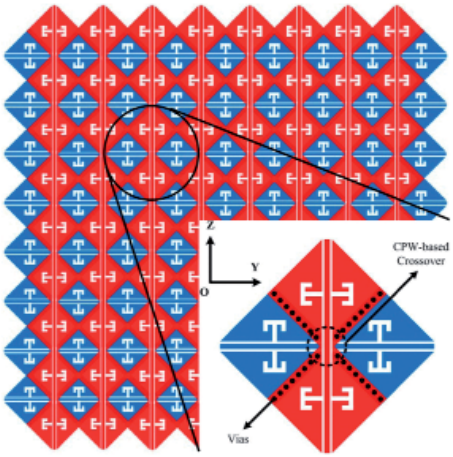

Figure 1a. A single-layer two-dimensional scalable dual-polarized series-fed slot array: the geometry and detailed view of the proposed array.

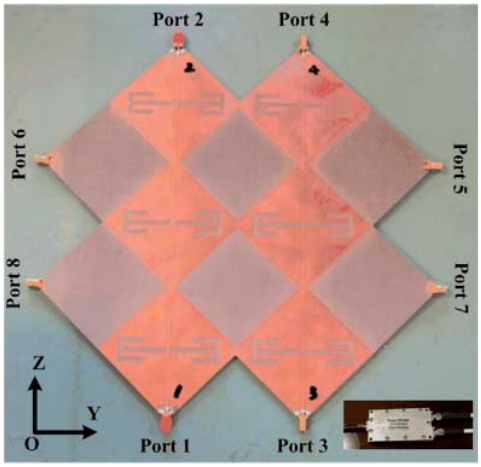

Figure 1b. A single-layer two-dimensional scalable dual-polarized series-fed slot array: a photograph of the proposed array.

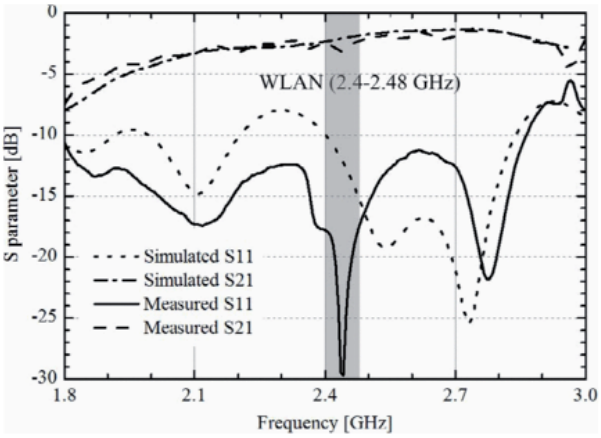

Figure 1c. A single-layer two-dimensional scalable dual-polarized series-fed slot array: the simulated and measured *S* parameters of the proposed array.

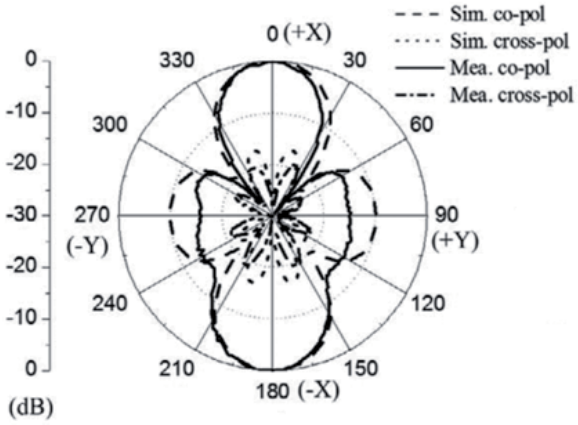

Figure 1d. A single-layer two-dimensional scalable dual-polarized series-fed slot array: the simulated and measured normalized radiation pattern at 2.4 GHz.

horizontal polarized slot array was series-fed by coplanar waveguide (CPW), and all the rows were excited by the power divider. Perpendicularly, the vertical polarized array was also series-fed using the same method. The unit cell of the whole slot array is shown in the detail view of Figure 1a. It was composed of slot elements, coplanar waveguide feeds, and a coplanar waveguide-based crossover. The half-wavelength slot element was grooved on the outer conductor of the coplanar waveguide, which was designed as an H-shaped slot due to size restrictions. Two adjacent slot elements on the one side were at a distance of one guided wavelength at 2.4 GHz. All elements could thus be excited in-phase at 2.4 GHz, so that each group of slot elements operated as a standing-wave array. This design eliminated the open stop band and rejected the absorbing loads at the end. At the intersection of two color areas, that is, the front and back sides of the unit cell, four lines of vias were designed to connect two sides of the substrate board and to make all the slots equipotential. By using the vias and the coplanar-waveguide-based crossover, the unit cell a achieved lower reflection coefficient (S_{11}), higher transmission coefficient (S_{21}), and better port isolation (S_{31} and S_{41}).

To prove the proposed structure as shown in Figure 1b, a 12-element slot array with a 3×2 element array for each polarization was processed and measured. Figure 1c shows the simulated and measured *S* parameters of the proposed array, where Port 1 was excited and the other ports were loaded. In the WLAN band, a reflection coefficient lower than −18 dB was achieved, with a transmission coefficient from −2.6 dB to −3.2 dB. Apart from this, the isolation of all of the ports was lower than −20 dB in the frequency band of 2.4 GHz to 2.48 GHz. To excite the proposed array, a 1-to-2 divider was used to feed through Port 1 and Port 3. The simulated and measured normalized radiation patterns in the *xoy*-plane at 2.4 GHz are shown in Figure 1d, in which bidirectional patterns were obtained with a sidelobe level

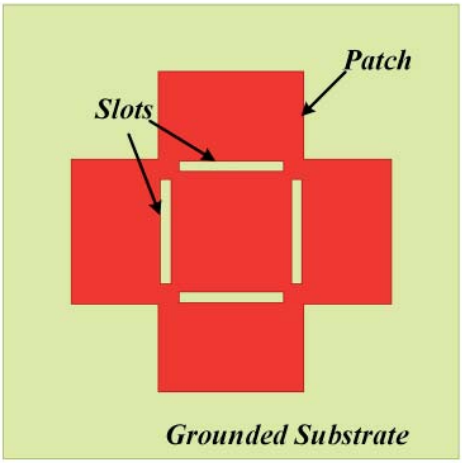

Figure 2a. The proposed dual-polarized, high-gain, and low-profile microstrip antenna based on the hybridized higher-order TM_{50} mode: a top view of the structure and the geometry.

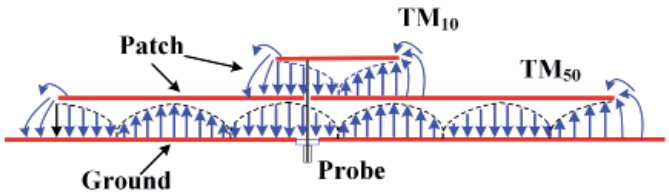

Figure 2b. A sketch of sectional electric vector field distribution of the dual-mode stacked microstrip antenna as in [31] for the antenna in Figure 2a.

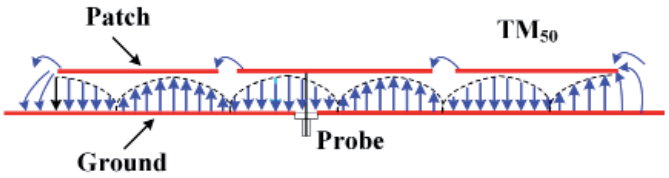

Figure 2c. A sketch of the electric vector field distribution of the proposed antenna shown in Figure 2a.

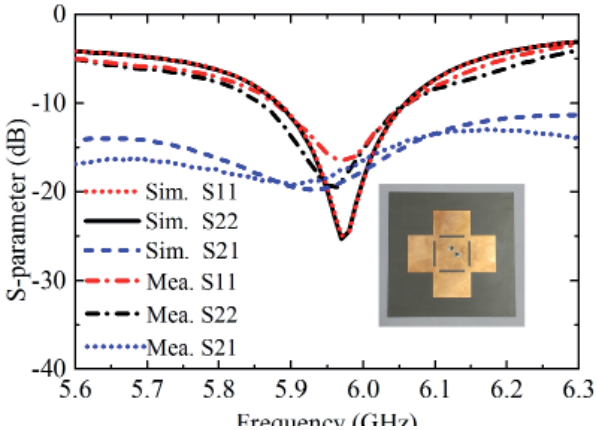

Figure 2d. The fabricated prototype and measured *S* parameters for the antenna in Figure 2a.

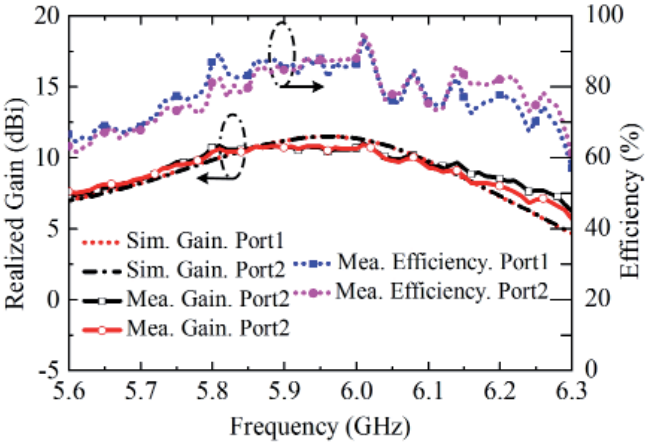

Figure 2e. The simulated and measured efficiency and gain of the two feeding ports for the antenna in Figure 2a.

lower than −10 dB. The radiation efficiency was 97.7% that getting rid of the mismatch, which could be reduced using a matching network. Compared with the structure of a conventional of dual-polarized array, this design used only one substrate board and coplanar-waveguide-based crossovers for compact construction, and can be two-dimensionally expanded without additional complexity.

3. Dual-Polarized Magnetic-Current Antenna Using the TM_{50} -Mode Microstrip Antenna

In this section, a higher-order TM_{50} mode was excited to obtain a dual-polarized microstrip antenna with significant gain enhancement [33], especially when compared with those conventional microstrip antennas operating at the TM_{10} mode. The geometry of this antenna is shown in Figure 2a. It was composed of a pair of orthogonal patches, four etched slots, and a single-layer grounded substrate. The operating principle is described through Figures 2b-2c. Because the dual-polarized antenna had a symmetric structure, only the polarization along the *y*-axis was analyzed as an example. Staring from a hybrid-mode single-polarized stacked microstrip antenna, inspired from the design concept in [31], the side view and a sketch of the sectional electric vector field distribution are shown in Figure 2b. The lower patch operated in the TM_{50} mode, and the upper suspended patch operated in the TM_{10} mode. It can be seen from the E-field distribution that the radiating edges of the two patches had in-phase superposition, which resulted in gain enhancement in the broadside direction. To modify the dual-layer structure into a single-layer structure, as shown in Figure 2c, two slots were etched on the lower patch to replace two radiating magnetic-currents of the upper patch, and a four-element in-phase single-polarized magnetic-current array was achieved. In the proposed

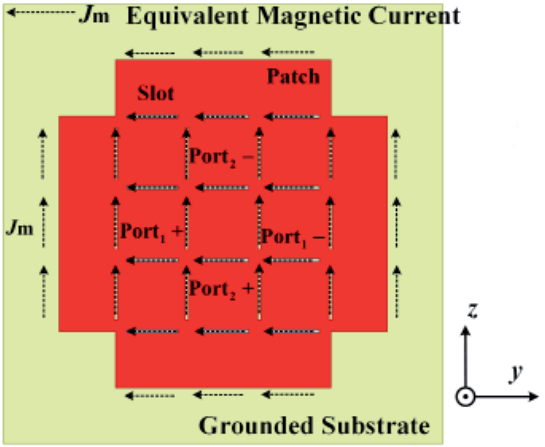

Figure 3a The proposed dual-polarized, high-gain, and low-profile magnetic-current array antenna based on a TM_{90}-mode microstrip antenna: the general structure and working principles.

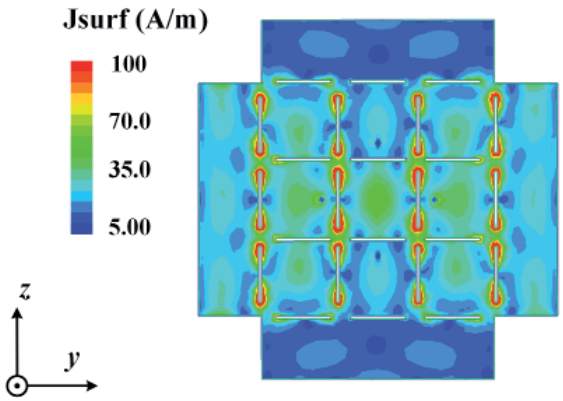

Figure 3b. The amplitude of the surface-current distribution for the antenna in Figure 3a.

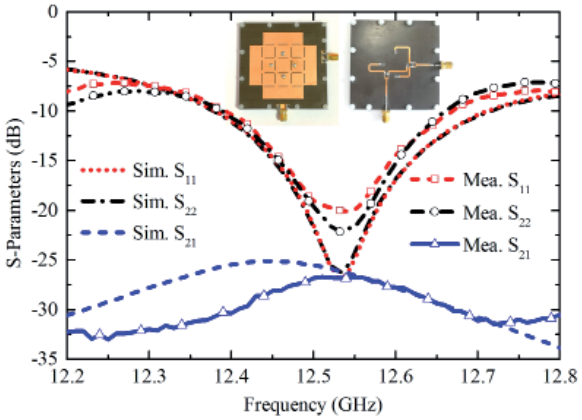

Figure 3c. The fabricated prototype and the measured and simulated *S* parameters for the antenna in Figure 3a.

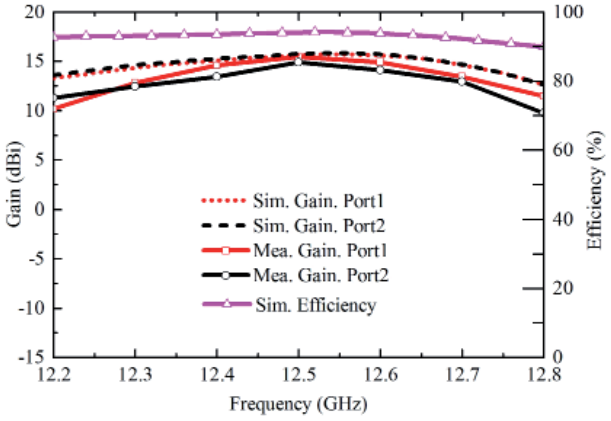

Figure 3d. The measured and simulated gains and efficiencies for the antenna in Figure 3a.

structure, a higher broadside gain was therefore realized by combining the radiating fields of two slots and the TM_{50}-mode patch. The polarization along the *z* axis operated under the same mechanism, and the dual-polarized antenna was easily constructed by combining these two polarizations.

The proposed antenna was fabricated. Its top view is shown in the inset of Figure 2, which also presents the simulated and measured *S* parameters. Two polarizations both achieved a −10 dB bandwidth of 5.88 GHz to 6.06 GHz, and obtain a good isolation of less than −14 dB. As shown in Figure 2, it was observed that the measured peak broadside gain of this antenna was 10.9 dBi, which is much higher than that of conventional microstrip antennas. Providing the merits of dual polarization, high broadside gain, simple feeding, and a single-layer structure, the proposed microstrip antenna using the slot-loaded TM_{50} mode has obvious potential applications in MIMO and 5G communication systems.

4. Dual-Polarized Magnetic-Current Array Using the TM_{90}-Mode Microstrip Antenna

In this section, a dual-polarized high-gain microstrip magnetic-current array antenna based on the higher-order TM_{90} mode is described [34]. Figure 3 shows the structure of the proposed dual-polarized high-gain antenna fed by two simple orthogonal differential ports. As can be seen in Figure 3a, 3×4×2 slots were located at the maximum point of the current on a patch antenna operating with the TM_{90} mode to achieve an in-phase 3×6 magnetic-current array for single-polarized high-gain radiation. By rotating the slotted patch 90° and combining together these two antennas, a dual-polarized high-gain antenna could be constructed. The antenna was fed by a simple feeding network with two differential pairs. Each pair contained a Wilkinson power divider and a microstrip delay line to generate two anti-phase excitations. The operating principle could be explained

through the current distribution shown in Figure 3b. Fed by port 1, the patch was excited at its TM_{90} mode. At the edges of the patch were the maximums of the electric fields, and two equivalent magnetic currents were formed. 3×4 slots, each of a half wavelength, were located perpendicular to the current at the nulls of electric fields, producing an additional 12 magnetic currents. A 3×6 magnetic-current array could therefore be excited by port 1, which was also compliant with the vertical feeding situations.

A prototype of the antenna was fabricated and measured. A photo of this prototype and the measured *S* parameters are depicted in Figure 3c, which shows agreement with simulated results. The impedance bandwidths of the two polarizations were from 12.38 GHz to 12.72 GHz. The gain and efficiency of the antenna is shown in Figure 3d. The maximum gain was 15.5 dBi at 12.52 GHz, and the radiation efficiency was above 90% over the operating bands.

5. Conclusion

In this paper, two different kinds of dual-polarized high-gain low-profile magnetic-current array antennas with a simple feeding strategy have been presented. For the first kind, by positioning two sets of coplanar waveguide-fed slot arrays orthogonally on opposite sides of a single substrate, a 2×3×2-element dual-polarized magnetic-current array was achieved with the merits of two-dimensional scalability, a simple feed, a single substrate layer, and high isolation. For the second kind, by loading half-wavelength slots on the electric-field nulls of a higher-order-mode microstrip antenna, a multiple-element in-phase magnetic-current array could be formed within a low-profile cavity with a simple feed and high isolation. As a validation for the proposed method, a dual-polarized 2×4-element in-phase magnetic-current array operating at 5.8 GHz was then designed using a TM_{50}-mode microstrip antenna, with the merits of a single feed, a single-layered configuration, and high isolation. The maximum gain reached 10.9 dBi within a compact volume of $1.65\,\lambda_0 \times 1.65\,\lambda_0 \times 0.04\,\lambda_0$. Last but not least, a dual-polarized 36-element (3×6×2) magnetic-current array antenna with a simple differential feed was experimentally implemented within a total size of $2.92\,\lambda_0 \times 2.92\,\lambda_0 \times 0.085\,\lambda_0$. This antenna achieved high isolation – better than 25 dB – and a maximum gain of 15.5 dBi within an operating bandwidth of 12.39 GHz to 12.68 GHz. In summary, these proposed antennas have the advantages of a low profile, a simple feed, and high isolation, exhibiting promising applications in diversity and MIMO systems, and in 5G communications.

6. References

1. M. A. Jensen and J. W. Wallace, "A review of antennas and propagation for MIMO wireless communication," *IEEE Trans. Antennas Propag.*, **52**, 11, 2004. pp. 2810-2824.

2. P. S. Kildal and K. Rosengran, "Correlation and capacity of MIMO systems and mutual coupling, radiation efficiency, and diversity gain of their antennas: Simulations and measurements in a reverberation chamber," *IEEE Commun. Mag.*, **42**, 12, 2004, pp. 102-112.

3. S. C. K. Ko and R. D. Murch, "Compact integration diversity antenna for wireless communications," *IEEE Trans. Antennas Propag.*, **49**, 6, 2001, pp. 954-960.

4. R. G. Vaughan, "Polarization diversity in mobile communications," *IEEE Trans. Veh. Technol.*, **39**, 3, 1990, pp. 177-186.

5. K. Mak, H. Wong, and K. Luk, "A shorted bowtie patch antenna with a cross dipole for dual polarization," *IEEE Antennas Wireless Propag. Lett.*, **6**, 2007, pp. 126-129.

6. Y. Gou, S. Yang, J. Li, and Z. Nie, "A compact dual-polarized printed dipole antenna with high isolation for wideband base station applications," *IEEE Trans. Antennas Propag.*, **62**, 8, 2014, pp. 4392-4395.

7. Y. Cui, X. Gao, H. Fu, Q.-X. Chu, and R. Li, "Broadband dual-polarized dual-dipole planar antennas: Analysis, design, and application for base stations," *IEEE Antennas Propag. Mag.*, **59**, 6, 2017, pp. 77-87.

8. Q. Xue, S. Liao, and J. Xu, "A differentially-driven dual-polarized magneto-electric dipole antenna," *IEEE Trans. Antennas Propag.*, **61**, 1, 2013, pp. 425-430.

9. Q. Wu and K. M. Luk, "A broadband dual-polarized magnetoelectric dipole antenna with simple feeds," *IEEE Antennas Wireless Propag. Lett.*, **8**, 2009, pp. 60-63.

10. S. G. Zhou, Z. H. Peng, G. L. Huang, and C. Y. Sim, "Design of a novel wideband and dual polarized magnetoelectric dipole antenna," *IEEE Trans. Antennas Propag.*, **65**, 5, 2017, pp. 2645-2649.

11. Y. Li, Z. J. Zhang, J. F. Zheng, and Z. H. Feng, "Compact azimuthal ominidirectional dual-polarized antenna using highly isolated collocated slots," *IEEE Trans. Antennas Propag.*, vol. **60**, 9, 2012, pp. 4037-4045.

12. Y. Li, Z. Zhang, W. Chen, Z. Feng, and M. F. Iskander, "A dual-polarization slot antenna using a compact CPW feeding structure," *IEEE Antennas Wireless Propag. Lett.*, **9**, 2010, pp. 191-194.

13. K. D. M. Pozar and D. H. Schaubert, *Microstrip Antennas: The Analysis and Design of Microstrip Antennas and Arrays*, New York, USA, IEEE Press, 1995.

14. Q. Li, S. W. Cheung, and C. Zhou, "A low-profile dual-polarized patch antenna with stable radiation pattern using ground-slot groups and metallic ground wall," *IEEE Trans. Antennas Propag.*, **65**, 10, October 2017, pp. 5061-5068.

15. X. Zhang and L. Zhu, "Gain-enhanced patch antennas with loading of shorting pins," *IEEE Trans. Antennas Propag.*, **64**, 8, August, 2016, pp. 3310-3318.

16. D. Sun, Z. Zhang, X. Yan, and X. Jiang, "Design of broadband dual polarized patch antenna with backed square annular cavity," *IEEE Trans. Antennas Propag.*, **64**, 1, January 2016, pp. 43-52.

17. Z. Tang, J. Liu, Y.-M. Cai, J. Wang, and Y. Yin, "A wideband differentially fed dual-polarized stacked patch antenna with tuned slot excitations," *IEEE Trans. Antennas Propag.*, **66**, 4, April 2018, pp. 2055-2060.

18. P. S. Hall and C. M. Hall, "Coplanar corporate feed effects in microstrip patch array design," *IEE Proc. H-Microw., Antennas Propag.*, **135**, 3, 1988, pp. 180-186.

19. J. Huang, "A Ka-band circularly polarized high-gain microstrip array antenna," *IEEE Trans. Antennas Propag.*, **43**, 1, January 1995, pp. 113-116.

20. H. D. Chen, C. Y. D. Sim, J. Y. Wu, and T. W. Chiu, "Broadband high gain microstrip array antennas for WiMAX base station," *IEEE Trans. Antennas Propag.*, **60**, 8, August 2012, pp. 3977-3980.

21. Y. Wang and Z. Du, "Dual-polarized slot-coupled microstrip antenna array with stable active element pattern," *IEEE Trans. Antennas Propag.*, **63**, 9, September 2015, pp. 4239-4244.

22. R. Lian, Z. Wang, Y. Yin, J. Wu, and X. Song, "Design of a low profile dual-polarized stepped slot antenna array for base station," *IEEE Antennas Wireless Propag. Lett.*, **15**, 2016, pp. 362-365.

23. E. Arnieri, L. Boccia, G. Amendola and G. Di Massa, "A Compact High Gain Antenna for Small Satellite Applications," *IEEE Transactions on Antennas and Propagation*, **55**, 2, February 2007, pp. 277-282.

24. W. Hong et al., "Multibeam Antenna Technologies for 5G Wireless Communications," *IEEE Transactions on Antennas and Propagation*, **65**, 12, December 2017, pp. 6231-6249.

25. M. I. Skolnik, *Introduction to Radar Systems*, New York, NY, USA, McGraw-Hill, 1980.

26. E. Rammos, "New wideband high-gain stripline planar array for 12 GHz satellite TV," *Electronics Letters*, **18**, 6, March 1982, pp. 252-253.

27. D. Pozar and S. Targonski, "A shared-aperture dual-band dual-polarized microstrip array," *IEEE Trans. Antennas Propag.*, **49**, 2, February 2001, pp. 150-157.

28. H. Wong, K. G. Lau, and K. Luk, "Design of dual-polarized L-probe patch antenna arrays with high isolation," *IEEE Trans. Antennas Propag.*, **52**, 1, January 2004, pp. 45-52.

29. S. Gao and A. Sambell, "Low-cost dual-polarized printed array with broad bandwidth," *IEEE Trans. Antennas Propag.*, **52**, 12, December 2004, pp. 3394-3397.

30. G. Vetharatnam, C. Kuan, and C. Teik, "Combined feed network for a shared-aperture dual-band dual-polarized array," *IEEE Antennas Wireless Propag. Lett.*, **4**, 2005, pp. 297-299.

31. P. Juyal and L. Shafai, "A high gain single feed dual mode microstrip disc radiator," *IEEE Trans. Antennas Propag.*, vol. 64, 6, June 2016, pp. 2115-2126.

32. Y. Li, Z. Zhang, C. Deng, Z. Feng and M. F. Iskander, "2-D Planar Scalable Dual-Polarized Series-Fed Slot Antenna Array Using Single Substrate," *IEEE Trans. Antennas Propag.*, **62**, 4, April 2014, pp. 2280-2283.

33. Y. He, Y. Li, W. Sun, Z. Zhang and P. Chen, "Dual Linearly Polarized Microstrip Antenna Using a Slot-Loaded TM_{50} Mode," *IEEE Antennas Wireless Propag. Lett.*, **17**, 12, December 2018, pp. 2344-2348.

34. Y. He, Y. Li, W. Sun and Z. Zhang, "Dual-Polarized, High-Gain, and Low-Profile Magnetic Current Array Antenna," *IEEE Trans. Antennas Propag.*, **67**, 2, February 2019, pp. 1312-1317.

Analysis and Design of a *W*-Band Circular Polarized Feed Horn with Built-In Polarizer for Low f/D Offset-Reflector Antenna

Ghanshyam Mishra[1], Satish K. Sharma[1], and Jia-Chi S. Chieh[2]

[1]Electrical and Computer Engineering
San Diego State University
5500 Campanile Dr.
San Diego, CA, USA
E-mails: gmishra-sw@sdsu.edu; ssharma@sdsu.edu

[2]Advanced Integrated Circuits Technology
Naval Info. Warfare Center Pacific
San Diego, CA, USA
E-mail: sam.chieh@navy.mil

Abstract

A novel low-axial-ratio *W*-band left-hand-circularly-polarized (LHCP) cylindrical waveguide feed horn antenna is described using a built-in polarizer. The built-in polarizer section of the horn consisted of nine pairs of circular cavities to generate circular polarization, eliminating the need for an external orthomode transducer or a complex septum. The polarizer was analyzed using the differential dispersion effect from the cavities along the length of the waveguide. The antenna had impedance matching ($|S_{11}| < -15$ dB) and an axial ratio below 1.2 dB from 79.5 GHz to 88 GHz. The horn antenna was then used as a feed source to illuminate an offset parabolic reflector of 10 cm diameter and a low $f/D = 0.25$. The feed-reflector assembly was also integrated inside a 1U volume of a 6U-CubeSat chassis. The radiation performance was analyzed using the Multilevel Fast Multipole Method (MLFMM) along with the Method of Moments (MoM) in TICRA *GRASP*. The measurement of the prototyped feed horn and the offset parabolic reflector antenna validated the analysis and simulation results.

1. Introduction

Satellite communications use high-gain circularly polarized (CP) antennas for reliable high-data-rate communication links. High-gain compact antennas can be easily installed inside the small satellites at high frequencies in the *W* band. In addition, *W*-band frequencies offer a low-attenuation absorption window and are thus suitable for high-data-rate communications. A reflector illuminated by the circularly polarized feed horn antenna provides a high-gain solution for satellite communications [1, 2].

A circularly polarized wave is realized by combining two orthogonal linearly polarized (LP) signals with a 90° time-phase difference. In [3], a dual circularly polarized feed polarizer was designed using an array of metallic pins as a delay structure to achieve the desired phase shift for the generation of circularly polarization. The losses of the pins, along with the fabrication challenges, limited the use of this method at millimeter-wave frequencies. In [4], a linearly polarized-circularly polarized conversion was achieved at sub-mm-wave frequencies by exploiting differential dispersion in hexagonal waveguides. In an orthomode transducer (OMT), a wideband circularly polarized wave can be generated by combining the two orthogonal linearly polarized signals into the waveguide structure [5-15]. This approach requires a dual input source and increased complexity, especially at millimeter-wave frequencies due to smaller feature sizes.

A *W*-band left-hand circularly polarized (LHCP) feed horn antenna with a built-in polarizer structure with a single side-fed input was analyzed and designed in this work. The described feed horn antenna illuminated an offset parabolic reflector of $f/D = 0.25$ to provide high-gain right-hand circular polarization (RHCP). The measured results of the fabricated prototype of the feed horn and offset-reflector antenna were in excellent agreement with the simulation. The effect of the CubeSat chassis on the radiation performance of the feed-reflector antenna was also investigated using the Multilevel Fast Multipole

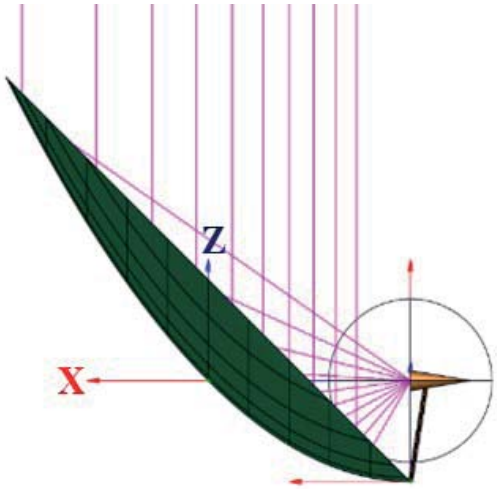

Figure 1. A ray-tracing diagram using TICRA *GRASP* with $\psi_e = 63.44°$ and $\psi_f = 90°$ for an offset parabolic reflector with $f/D = 0.25$.

Method (MLFMM) along with the Method of Moments (MoM) in TICRA *GRASP*. Additional discussions related to this paper were presented in [16-18]. In [19], the initial results related to the effect of the finite metal wall thickness on the radiation of the proposed feed horn antenna were investigated.

2. Proposed Feed Requirements

The proposed horn antenna was developed as a feed for an offset parabolic reflector antenna that can be placed inside the compact 1U (10 cm × 10 cm × 10 cm) volume of the CubeSat chassis. The stringent space constraint led to the selection of a small f/D of 0.25 to accommodate the reflector of diameter $D = 10$ cm inside the 1U block of the CubeSat.

Based on the above dimensions, the half cone angle subtended at the rim of the reflector (ψ_e) was calculated in [17] to be 63.44°, and the feed source needed to be directed towards the center of the offset reflector from the focal axis (ψ_f) by 90° [20]. Accordingly, the proposed feed horn antenna was designed to have a 12 dB half-edge illumination angle of around 64° within the desired bandwidth of 79.5 GHz to 88 GHz. The ray-tracing diagram of an offset parabolic reflector with the calculated values is plotted in Figure 1 using TICRA *GRASP*.

To study the effect of strict physical constraints on the co- and cross-polarization performance of the antenna, a simulation with the ideal Gaussian left-hand circularly polarized feed source was carried out in *GRASP*. The ideal Gaussian feed ignored the cross-polarization radiation. The peak right-hand circular polarization directivity of the offset parabolic reflector illuminated by the ideal Gaussian left-hand circularly polarized feed was 37.5 dBic, and the cross-polarization isolation was 41.5 dB within the main lobe at 86 GHz, as presented in Figure 2. The 3 dB beamwidth was 2.3°, and the spillover loss of the offset reflector was 0.63 dB at 86 GHz. Significant cross-polarization was thus observed even with the ideal feed illumination of the reflector. This high cross-polarization effect was the limitation of the low f/D ratio, and was present even when excited by the proposed feed horn antenna, as discussed in the next section.

3. Built-In Feed Horn Polarizer

3.1 Proposed Feed Horn Antenna Geometry

Figure 3 shows the front and isometric views of the feed horn antenna. The built-in polarizing structure included nine pairs of circular cavities in the cylindrical waveguide wall. These cavities were oriented at 45° to the rectangular

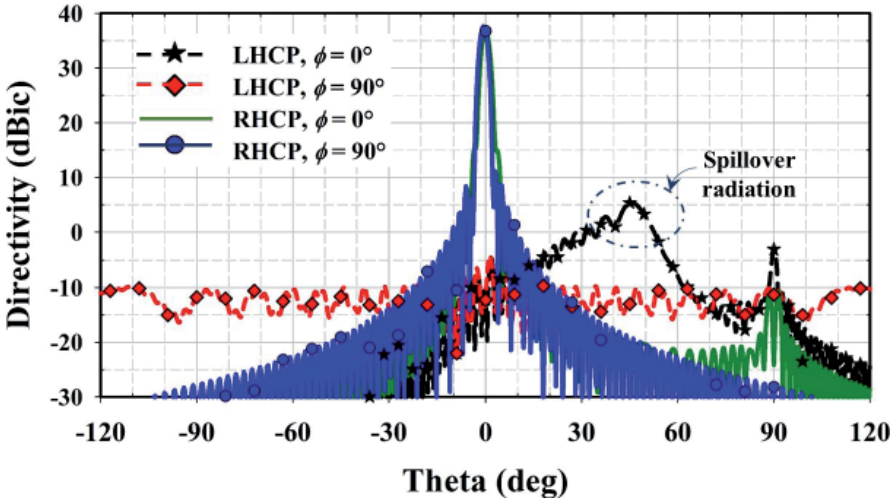

Figure 2. The simulated directivity pattern of an ideal Gaussian-fed offset parabolic reflector with $f/D = 0.25$ from TICRA *GRASP*.

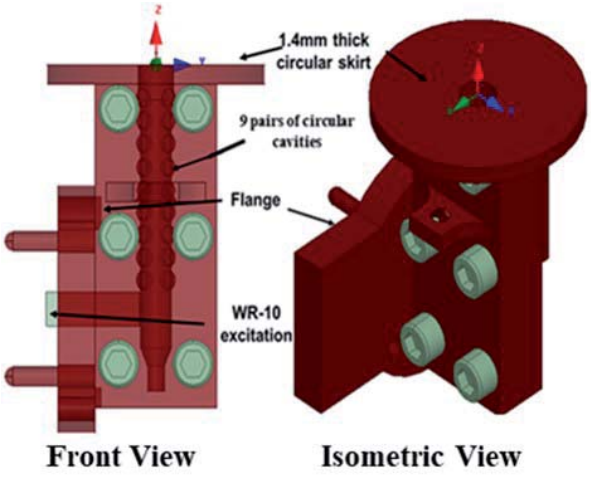

Figure 3. The proposed left-hand circularly polarized feed-horn antenna's geometry.

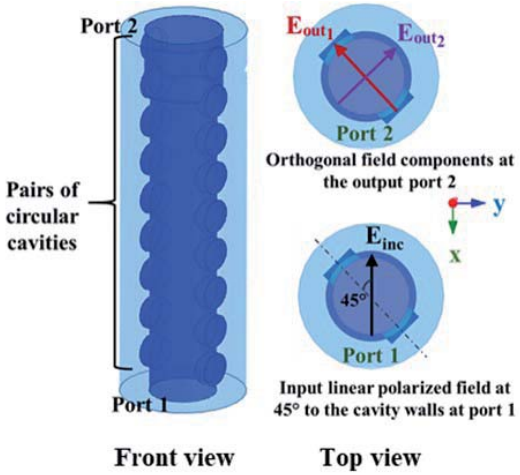

Figure 4. A two-port model of the polarizer structure of the proposed antenna with the top view showing input and output field components.

input port. The physical dimensions of the horn antenna were 26 mm × 14 mm × 5.25 mm. The cavity diameter was 1.39 mm, the spacing between the cavity pairs was 1.70 mm, and the depth of the cavity was 0.36 mm. A 1.40 mm thick circular skirt at the top of the rectangular wall was used to reduce diffraction from the edges of the waveguide.

Circular polarization in the proposed feed horn was achieved by incorporating a polarizing structure inside the cylindrical waveguide. The proposed built-in polarizer had the advantage of reducing the degradation in the antenna's radiation performance from fabrication inaccuracies as the cavities were placed on the wall of the circular waveguide where the electromagnetic field was sparse, as opposed to placing metallic pins [3] in the dense electromagnetic-field region of the circular waveguide. The proposed left-hand circularly polarized feed horn antenna was used as a feed source to excite an offset parabolic reflector with a small $f/D = 0.25$.

3.2 Principle of Operation

Figure 4 illustrates the two-port model of the polarizer section of the feed horn [17]. Since the input was offset 45° to the cavity pairs, the input RF signal, E_{inc} , was split into two orthogonal degenerate TE_{11} modes. The propagation constants of these propagating modes were different due to the cavity pairs along E_{out1}, as shown in Figure 5. As a result, the E_{out1} field in the direction of the cavity pairs had an additional phase delay of $\lambda/4$ relative to the orthogonal field E_{out2} at the aperture of the polarizer to generate the desired left-hand circularly polarization. The polarizer device could be viewed as a three-port structure, even with its two physical ports. The two degenerate modes at the output circular wave-port made the polarizer act as a three-port structure. The general expression for the 3 × 3 scattering matrix is written as

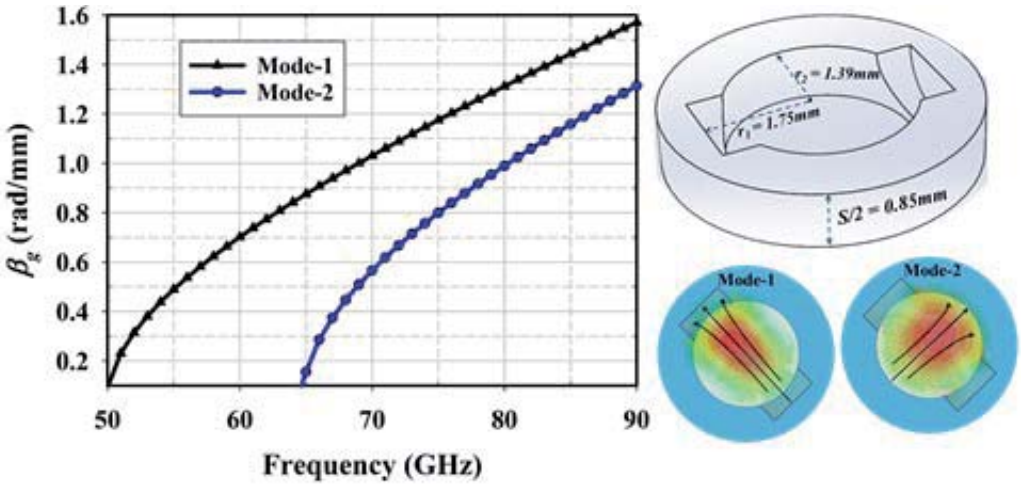

Figure 5. The dispersion-relation graph for a section of the polarizer, simulated in Ansys *HFSS*.

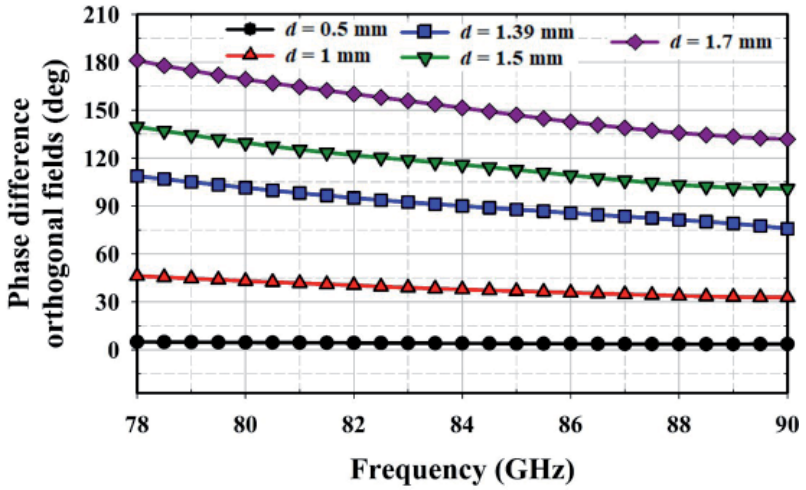

Figure 6. The effects of different cavity diameters, *d*, on the phase difference between the two orthogonal fields at the output port of the polarizer.

$$S = \frac{1}{2}\begin{bmatrix} 0 & -\sqrt{2}e^{-j\beta_1 L} & \sqrt{2}e^{-j\beta_2 L} \\ -\sqrt{2}e^{-j\beta_1 L} & 0 & 0 \\ \sqrt{2}e^{-j\beta_2 L} & 0 & 0 \end{bmatrix}, \quad (1)$$

where L is the length of the circular waveguide polarizer, and β_1 and β_2 are the propagation constants in the polarizer. The summation of the difference in propagation constants of the two modes $\beta_1(z_i, f)$ and $\beta_2(z_i, f)$ along the length of the polarizer gives the phase difference of 90° [4], as in Equation (2):

$$\sum_{i=1}^{L/\delta z} \left[\beta_2(z_i, f) - \beta_1(z_i, f)\right]\delta z = \frac{\pi}{2}, \quad (2)$$

where z_i (along the z direction) is the distance from the feed point for the ith discretized section in the waveguide at frequency f.

3.3 Parametric Studies

A parametric analysis was carried out in Ansys *HFSS* over the number of circular cavity pairs, the diameter, the depth, and the spacing between the circular cavities, keeping the length of the feed horn constant. Later, based on the optimum parametric values, a sequential nonlinear programming (gradient) optimization method was employed on the feed horn with the goal of an axial ratio (AR) less than 1.5 dB within the frequency range of 79 GHz to 88 GHz. In the optimum polarizer with nine pairs of circular cavities, the phase difference between the output field components was 90° (±15°), and the maximum amplitude imbalance was 0.10 dB across 79 GHz to 88 GHz.

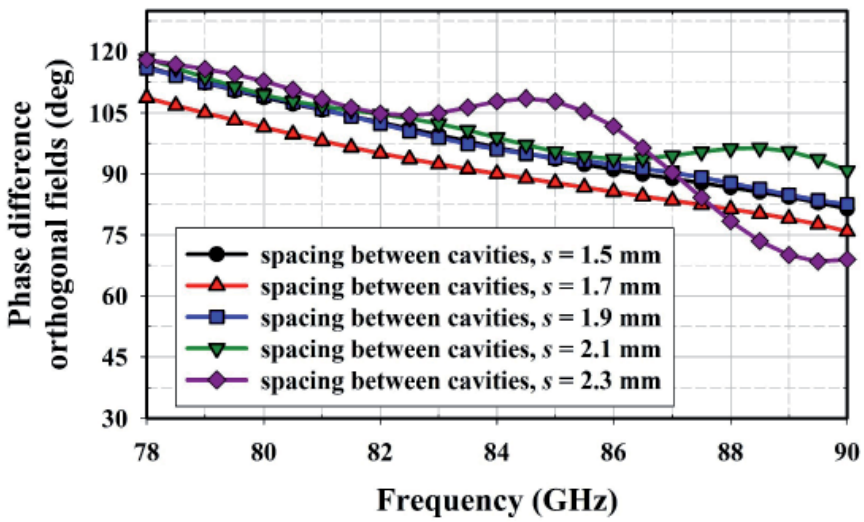

Figure 7. The effects of different spacings, *s*, between the cavities on the phase difference between the two orthogonal fields at the output port of the polarizer.

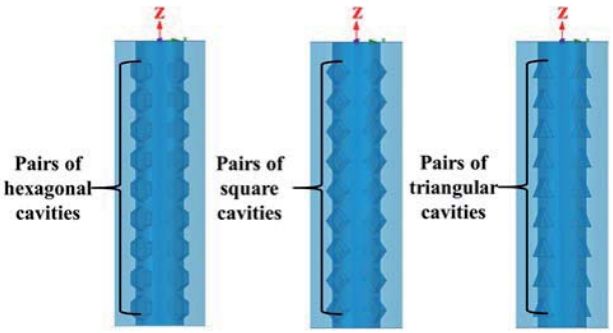

Figure 8. Different cavity shapes in the polarizer: (a) hexagonal, (b) square, and (c) triangular cavity shapes.

Figure 6 presents the effects of varying the cavity diameter on the output phase difference between the field components as a function of frequency for nine pairs of circular cavities. It was clear that for a cavity diameter of $d = 1.39$, the phase difference between the output field components was around 90°. The effect of varying the spacing, *s*, between the cavities on the phase difference is shown in Figure 7. A spacing $s = 1.70$ mm provided a phase delay of 90° (±10°) between the output field components.

Hexagonal, square, and triangular were the three different shapes of the cavity that were studied in addition to the circular cavity shapes, as illustrated in Figure 8. The effects of different cavity shapes on the phase difference are shown in Figure 9. The triangular cavity polarizer provided the least phase delay for a fixed length of the polarizer, whereas the proposed circular cavity polarizer offered the optimum phase difference to generate circularly polarization.

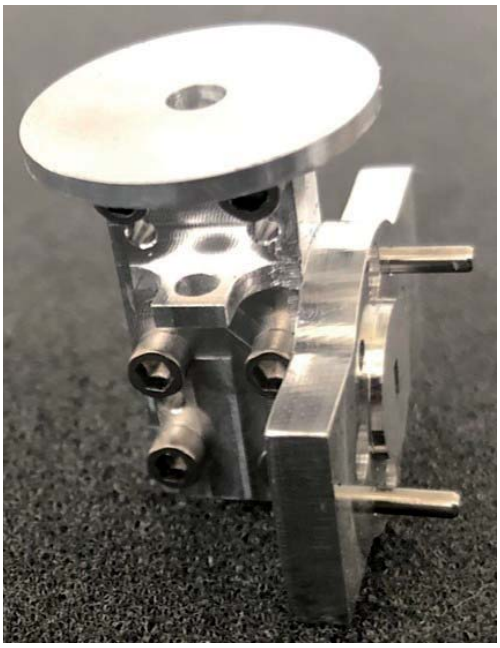

Figure 10a. A photograph of the fabricated feed-horn antenna.

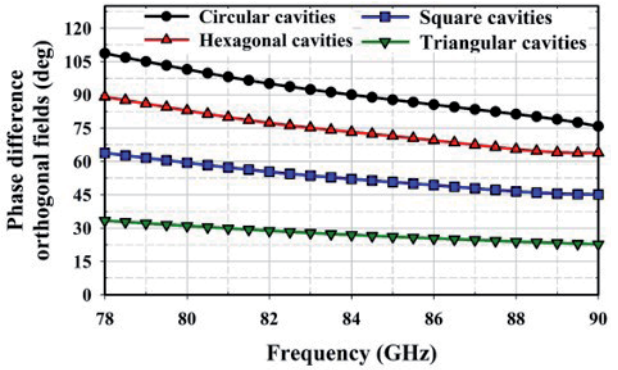

Figure 9. The effects of different shapes of the cavity on the phase difference between the two orthogonal fields.

4. Simulation and Measurement Results

The prototypes of the feed horn and the offset parabolic reflector antenna are shown in Figures 10a and 10b. The fabricated designs were measured in the Microwave Vision Group (MVG) spherical near-field chamber. The reflection-coefficient magnitude and axial ration of the feed-horn antenna were presented in [17] and are again shown in Figures 11 and 12 for clear discussion. The simulated and measured impedance matching of the feed-horn antenna were in excellent agreement from 79.5 GHz to 88 GHz, as shown in Figure 11. The simulated and measured axial ratio for the feed-horn antenna was below 1.2 dB over the entire matching bandwidth, as shown in Figure 12. The axial ratio as a function of elevation angle for different frequencies is presented in Figure 13. The average 3 dB axial-ratio beamwidth was around 100° within the desired frequency range. The slight variation in the measured and simulated results might be due to the fabrication tolerance of the cavities in the feed horn.

The three-dimensional realized gain radiation patterns are shown for the simulation and measurement in Figures 14a, 14b, and 14c at 79 GHz, 83 GHz, and 86 GHz, respectively. It could be observed that a stable and symmetric radiation pattern was obtained over the entire desired bandwidth. The simulated peak left-hand circularly polarized gains of the feed horn were 9.2 dBic, 9.5 dBic, and

Figure 10b. A photograph of the offset parabolic reflector with the feed horn.

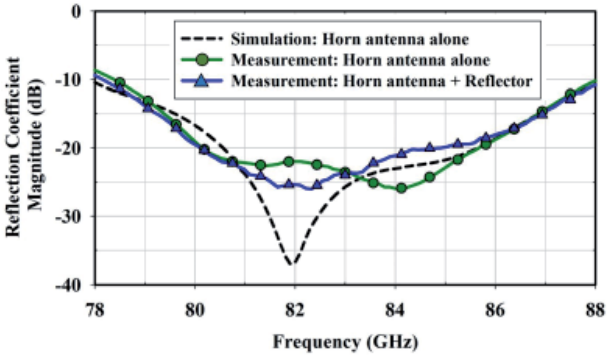

Figure 11. The simulated and measured S_{11} values of the proposed horn antenna and the measured S_{11} values of the integrated feed horn and reflector antenna.

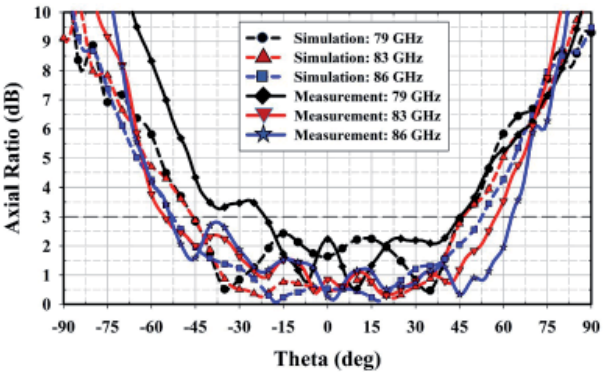

Figure 13. The simulated and measured axial ratio as a function of elevation angle, theta, of the feed-horn antenna.

9.45 dBic, and the peak cross-polarization isolations were 20 dB, 24 dB, and 25 dB at 79 GHz, 83 GHz, and 86 GHz, respectively. The measured peak left-hand circularly polarized gains of the horn were 7.9 dBic, 8.9 dBic, and 9.1 dBic, and the peak cross-polarization isolations were 16 dB, 20 dB, and 19 dB, at 79 GHz, 83 GHz, and 86 GHz, respectively.

The discrepancies between the measured and simulated results might be due to the fabrication and measurement tolerances. The proposed feed-horn antenna provided measured 12 dB half-edge illumination of 65° over the matching bandwidth, and thus met the requirement to illuminate an offset parabolic reflector of $f/D = 0.25$.

The proposed horn antenna was used as a feed source to illuminate an offset parabolic reflector with a small $f/D = 0.25$ and a reflector diameter of 10 cm. The geometry of the integrated feed-reflector was presented in [17], and it is included here in Figure 15 for clarity. Extra metal thickness was added around the rim of the reflector for ease of fabrication and structural support.

The offset reflector was analyzed using TICRA *GRASP*, which utilizes Physical-Optics (PO) currents on the reflector and Physical Theory of Diffraction (PTD) rim

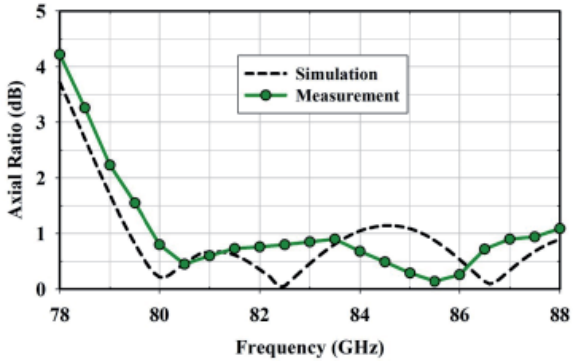

Figure 12. The simulated and measured axial ratio of the proposed feed-horn antenna as a function of frequency.

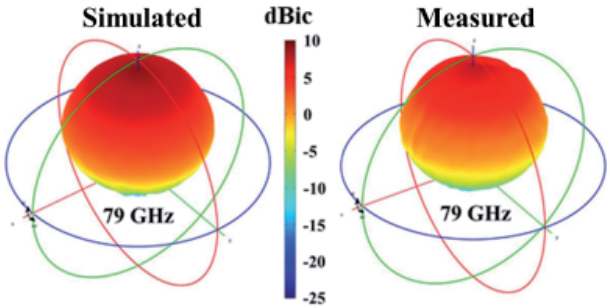

Figure 14a. The simulated (left) and measured (right) three-dimensional realized gain radiation patterns of the proposed feed-horn antenna at 79 GHz.

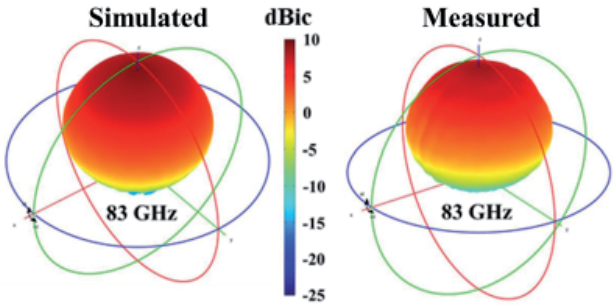

Figure 14b. The simulated (left) and measured (right) three-dimensional realized gain radiation patterns of the proposed feed-horn antenna at 83 GHz

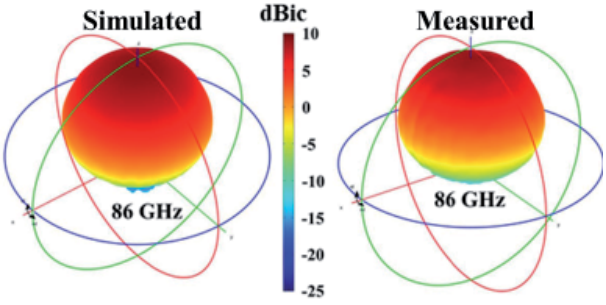

Figure 14c. The simulated (left) and measured (right) three-dimensional realized gain radiation patterns of the proposed feed-horn antenna at 86 GHz.

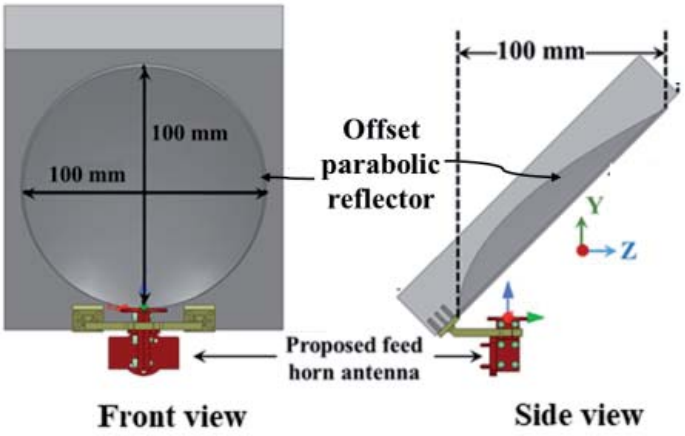

Figure 15. The offset parabolic reflector of $f/D = 0.25$, illuminated by the proposed feed-horn antenna.

currents to obtain the total induced current on the reflector. The radiation from the feed and the induced currents on the offset parabolic reflector were summed to get the total field.

The offset reflector was also analyzed using Ansys *HFSS*. Figures 16a, 16b, and 16c show the stable surface-current distributions on the reflector with an edge taper of -12 dB at 79 GHz, 83 GHz, and 86 GHz, respectively.

The simulated directivity patterns of the offset reflector at 79 GHz and 86 GHz are presented in Figures 17a and 17b, respectively, using TICRA *GRASP*. The peak simulated right-hand circular polarization directivities were 35.7 dBic and 36.6 dBic, with peak cross-polarization separations of 20 dB and 23.3 dB, at 79 GHz and 86 GHz, respectively. The simulated spillover loss of the reflector, analyzed from TICRA *GRASP*, was 0.83 dB. The average 3 dB beamwidths were 2.5° in both the $\varphi = 0°$ and $\varphi = 90°$ planes. The high cross-polarization level was an inherent property of the small f/D of the offset parabolic reflector.

The measured two-dimensional realized gain reflector patterns at 79 GHz and 86 GHz, respectively, are shown in Figures 18a and 18b. The small f/D of 0.25, along with the offset configuration of the reflector, resulted in a high cross-polarization. The measured peak right-hand circular polarization gains of the proposed feed reflector antenna were 32.92 dBic and 34.36 dBic at 79 GHz and 86 GHz, respectively.

The measured three-dimensional realized gain right-hand circular polarization radiation patterns are shown in Figures 19a, 19b, and 19c at 79 GHz, 83 GHz, and 86 GHz, respectively. The average measured 3 dB beamwidth was 3° and 2.8° in the $\varphi = 0°$ and $\varphi = 90°$ planes, respectively.

The average measured total antenna efficiency of the offset parabolic reflector was above 60% within the desired matching bandwidth from 79.5 GHz to 88 GHz. The total antenna efficiency includes the effects of feed-horn mismatch loss, feed-horn radiation efficiency, spillover, and the aperture efficiency of the offset reflector.

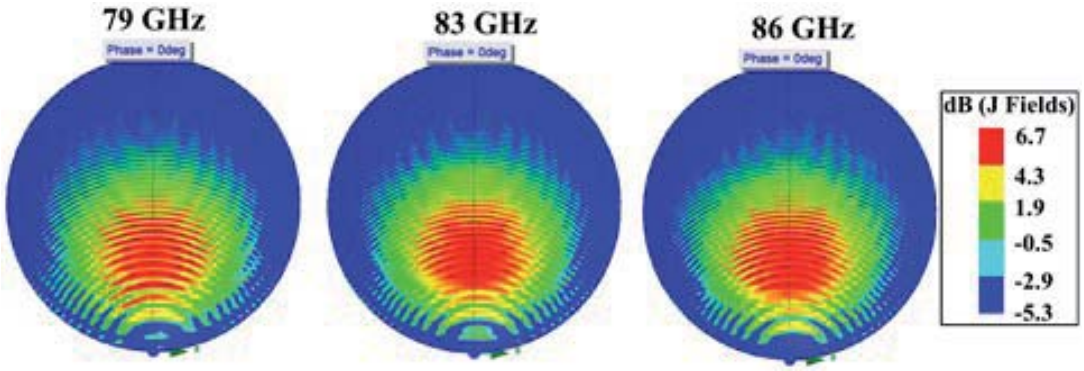

Figure 16. The current distribution on the offset parabolic reflector simulated in Ansys *HFSS* at (a) 79 GHz, (b) 83 GHz, and (c) 86 GHz.

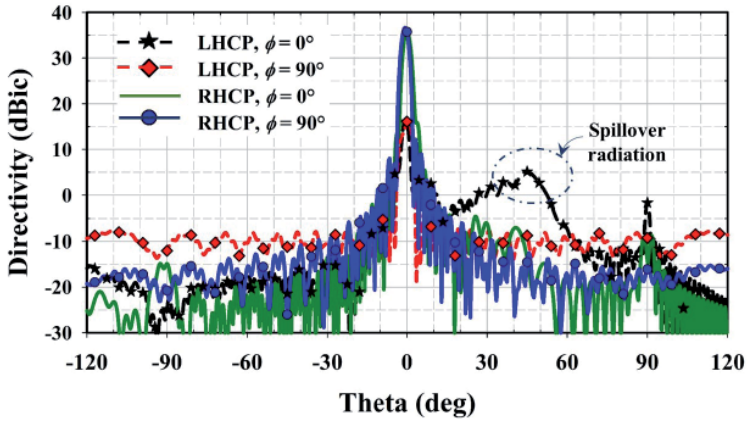

Figure 17a. The simulated directivity pattern of the offset parabolic reflector illuminated by the proposed feed horn at 79 GHz.

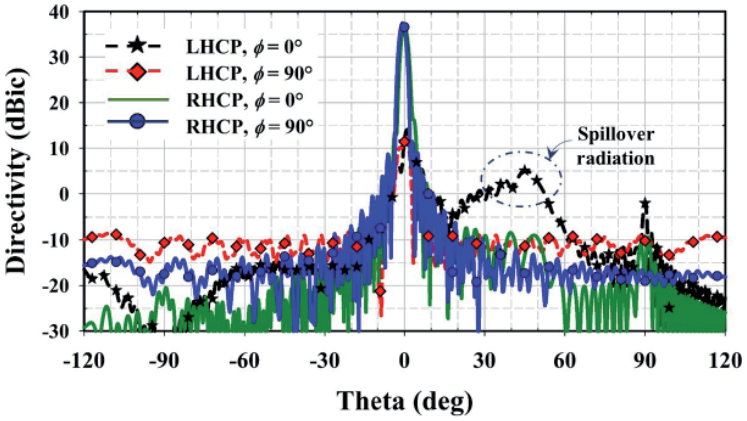

Figure 17b. The simulated directivity pattern of the offset parabolic reflector illuminated by the proposed feed horn at 86 GHz.

5. Effect of 6U-Cubesat Chassis

The proposed feed-reflector assembly was designed to be used in a CubeSat application at *W* band. The impact of the CubeSat chassis on the antenna's radiation performance was analyzed using the Multilevel Fast Multipole Method (MLFMM) along with the Method of Moments (MoM) in TICRA *GRASP*. The solver discretized the geometry using higher-order quadrilateral patches and surface currents using higher-order basis functions.

The position of the feed-reflector assembly inside the CubeSat chassis was chosen to study the worst-case antenna performance. The CAD rendering of the integrated feed reflector inside a 1U block of the 6U-CubeSat chassis and the simulated MoM current distribution on the entire structure at 86 GHz are presented in Figure 20. The comparison of

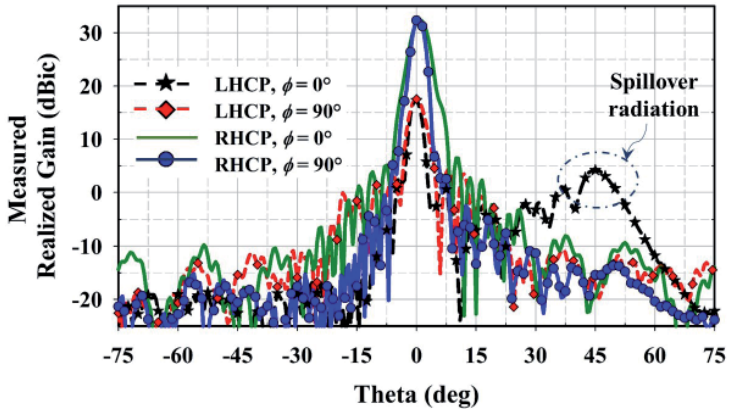

Figure 18a. The measured realized gain radiation pattern of the offset parabolic reflector at 79 GHz.

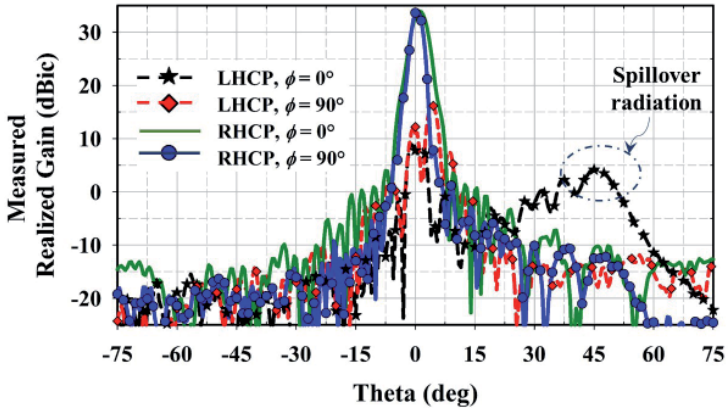

Figure 18b. The measured realized gain radiation pattern of the offset parabolic reflector at 86 GHz.

the two-dimensional directivity patterns of the feed-reflector assembly with and without the CubeSat chassis are shown in Figures 21a and 21b at $\varphi = 0°$ and $\varphi = 90°$, respectively. The peak simulated right-hand circular polarization directivities of the integrated feed-reflector inside the CubeSat chassis were 35.69 dBic and 36.53 dBic, and the peak simulated right-hand circular polarization directivities of the feed-reflector antenna without the CubeSat chassis were 36.53 dBic and 37.44 dBic, at $\varphi = 0°$ and $\varphi = 90°$, respectively. The left-hand circularly polarized cross-polarization increased significantly, by 6 dB and 8 dB at $\varphi = 0°$ and $\varphi = 90°$, respectively, in the presence of the CubeSat chassis. The CubeSat chassis thus had a strong impact on the cross-polarization level, and reduced the peak right-hand circular polarization directivity by 0.9 dB.

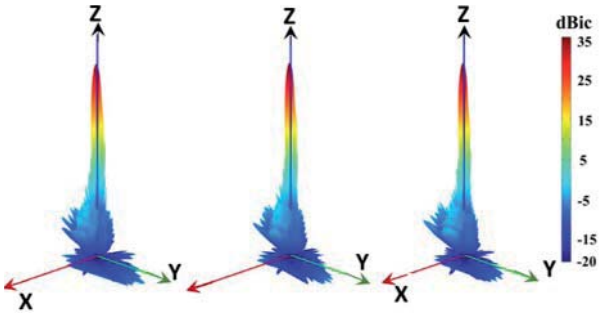

Figure 19. The measured three-dimensional right-hand circular polarization realized gain radiation patterns of the offset parabolic reflector at (a) 79 GHz, (b) 83 GHz, and (c) 86 GHz.

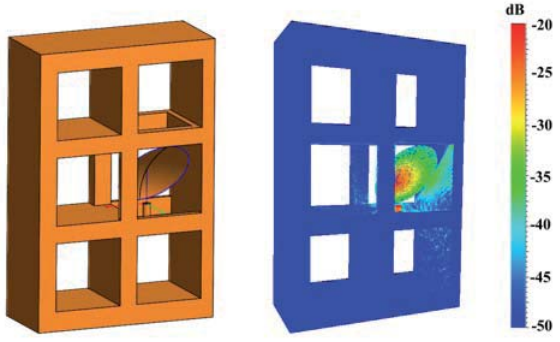

Figure 20. A CAD rendering (left) and the simulated current distribution (right) at 86 GHz of the feed-reflector assembly inside the 6U CubeSat chassis.

6. Conclusion

A novel circularly polarized feed horn was analyzed and developed at *W*-band frequencies from 79.5 GHz to 88 GHz, which eliminated the need for an external orthomode transducer or a complex septum. The results of the analysis and the simulation were validated in the fabrication and measurement of the proposed feed-horn antenna. The proposed feed horn was shown to have an impedance matching ($|S_{11}|$ below −15 dB) and an axial ratio (below 1.2 dB) from 79.5 GHz to 88 GHz. The proposed feed-horn antenna exhibited stable and symmetric radiation patterns across the desired frequency range. The strong impact of the CubeSat chassis on the radiation performance of the proposed feed horn integrated with the offset parabolic reflector assembly was also simulated using the MoM/MLFMM solver in TICRA *GRASP*.

7. Acknowledgment

The authors would like to thank MVG for the measurement of the feed horn and reflector antenna at their spherical near-field measurement facility. This work was supported by the Office of Naval Research (ONR) grant # N00014-16-1-2166.

8. References

1. L. Shafai, S. K. Sharma and S. Rao, *Handbook of Reflector Antennas and Feed Systems: Feed Systems*, *Vol. II*, Norwood, MA, USA, Artech House, 2013.

2. S. K. Sharma, L. Shafai and S. Rao, *Handbook of Reflector Antennas and Feed Systems: Theory and Design of*

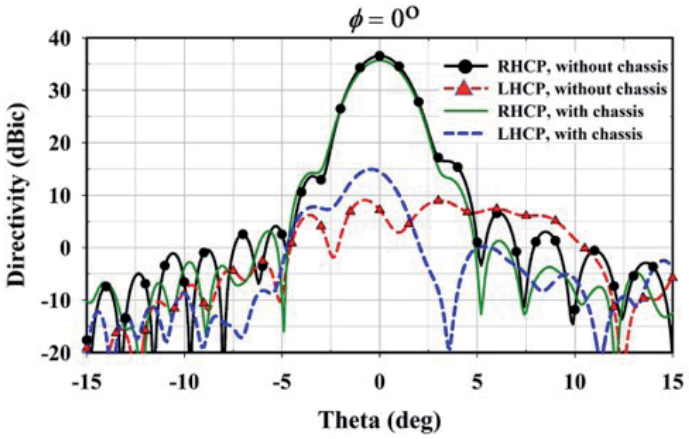

Figure 21a. The simulated two-dimensional directivity pattern of the feed-reflector with and without the 6U CubeSat chassis in the $\varphi = 0°$ plane, analyzed using the MoM/MLFMM solver in TICRA *GRASP*.

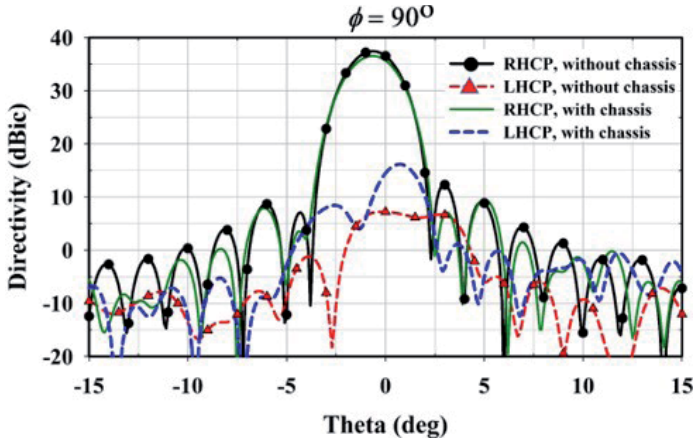

Figure 21b. The simulated two-dimensional directivity pattern of the feed-reflector with and without the 6U CubeSat chassis in the $\varphi = 90°$ plane, analyzed using the MoM/MLFMM solver in TICRA GRASP.

Reflectors, *Vol. I*, Norwood, MA, USA, Artech House, 2013.

3. S. K. Sharma, L. Shafai and M. Barakat, "Ka-band dual circularly polarized feed horn polarizer for reflector antennas for satellite communications," *11th International Symposium on Antenna Technology and Applied Electromagnetics [ANTEM 2005]*, St. Malo, 2005, pp. 1-4.

4. S. Bhardwaj and J. L. Volakis, "Hexagonal Waveguide Based Circularly Polarized Horn Antennas for Sub-mm-Wave/Terahertz Band," *IEEE Transactions on Antennas and Propagation*, **66**, 7, July 2018, pp. 3366-3374.

5. A. M. Boifot, E. Lier and T. Schaug-Pettersen, "Simple and broadband orthomode transducer (antenna feed)," *IEE Proceedings H - Microwaves, Antennas and Propagation*, **137**, 6, December 1990, pp. 396-400.

6. J. A. Ruiz-Cruz, J. R. Montejo-Garai, C. A. Leal-Sevillano, and J. M. Rebollar, "Orthomode Transducers With Folded Double-Symmetry Junctions for Broadband and Compact Antenna Feeds," *IEEE Transactions on Antennas and Propagation*, **66**, 3, March 2018, pp. 1160-1168.

7. J. A. Ruiz-Cruz, J. R. Montejo-Garai, J. M. Rebollar and J. M. Montero, "C-band orthomode transducer for compact and broadband antenna feeders," *Electronics Letters*, **45**, 16, July 30 2009, pp. 813-814.

8. M. Esquius-Morote, M. Mattes and J. R. Mosig, "Orthomode Transducer and Dual-Polarized Horn Antenna in Substrate Integrated Technology," IEEE Transactions on Antennas and Propagation, 62, 10, October 2014, pp. 4935-4944.

9. M. A. Moharram, A. Mahmoud, and A. A. Kishk, "A Simple Coaxial to Circular Waveguide OMT for Low-Power Dual-Polarized Antenna Applications," *IEEE Transactions on Microwave Theory and Techniques*, **66**, 1, January 2018, pp. 109-115.

10. R. Garcia, F. Mayol, J. M. Montero, and A. Culebras, "Circular polarization feed with dual-frequency OMT-based turnstile junction," *IEEE Antennas and Propagation Magazine*, **53**, 1, February 2011, pp. 226-236.

11. A. A. Sakr, W. Dyab, and K. Wu, "Design Methodologies of Compact Orthomode Transducers Based on Mechanism of Polarization Selectivity," *IEEE Transactions on Microwave Theory and Techniques*, **66**, 3, March 2018, pp. 1279-1290.

12. G. M. Coutts, "Wideband Diagonal Quadruple-Ridge Orthomode Transducer for Circular Polarization Detection," *IEEE Transactions on Antennas and Propagation*, **59**, 6, June 2011, pp. 1902-1909.

13. G. Virone, O. A. Peverini, M. Lumia, M. Z. Farooqui, G. Addamo, and R. Tascone, "W-Band Orthomode Transducer for Dense Focal-Plane Clusters," *IEEE Microwave and Wireless Components Letters*, **25**, 2, February 2015, pp. 85-87.

14. G. M. Coutts, "Octave Bandwidth Orthomode Transducers for the Expanded Very Large Array," *IEEE Transactions on Antennas and Propagation*, **59**, 6, June 2011, pp. 1910-1917.

15. W. Hongjian, Y. Min, L. Guang, and C. Xue, "Potter Horn and Compact Orthomode Transducer at 150 GHz," *IEEE Transactions on Antennas and Propagation*, **62**, 10, October 2014, pp. 5403-5405.

16. G. Mishra, A. T. Castro, S. K. Sharma and J.-C. S. Chieh, "W-band feed horn with polarizer structure for an offset reflector antenna for CubeSat applications," IEEE International Symposium on Antennas and Propagation & USNC/URSI National Radio Science Meeting, San Diego, CA, 2017, pp. 557-558.

17. G. Mishra, S. K. Sharma, and J.-C. S. Chieh, "A Circular Polarized Feed Horn with Inbuilt Polarizer for Offset Reflector Antenna for *W* -Band CubeSat Applications," *IEEE Transactions on Antennas and Propagation*, **67**, 3, March 2019, pp. 1904-1909.

18. G. Mishra, S. K. Sharma, and J.-C. S. Chieh, "Analysis and Design of a W-Band Circular Polarized Feed Horn with Inbuilt Polarizer for Low F/D Offset Reflector Antenna," URSI Commission B International Symposium on Electromagnetic Theory (EMTS 2019), San Diego, CA [accepted].

19. G. Mishra, S. K. Sharma and J.-C. S. Chieh, "Finite Metal Wall Effects of W-Band Circular Polarized Horn Antenna with Inbuilt Polarizer," IEEE International Symposium on Antennas and Propagation and USNC-URSI Radio Science Meeting, Atlanta, GA, USA, 2019, pp. 971-972.

20. T. A. Milligan, "Reflector Antennas," in *Modern Antenna Design*, Hoboken, NJ, USA, Wiley, 2005, p. 580.

Optical Metasurfaces Based on Spheroidal Nanoparticles: Theory and Applications

Alessio Monti[1], AndreaAlù[2], Alessandro Toscano[3], and Filiberto Bilotti[3]

[1]Niccolò Cusano University
Via don Carlo Gnocchi 3, 00166 Rome, Italy
E-mail: alessio.monti@unicusano.it

[2]CUNY Advanced Science Research Center
85 St. Nicholas Terrace
New York, 10031, USA

[3]Roma Tre University
Engineering Department
Via Vito Volterra 62
00146, Rome, Italy

Abstract

In this paper, we review our recent results about the theoretical modeling and the possible applications of optical metasurfaces made of arrays of spheroidal nanoparticles. We consider both the case of plasmonic and dielectric nanoparticles, and we show how their peculiar responses in the visible range make them plausible candidates for several innovative nanophotonic applications. We also show that the coupled dipole model allows properly homogenizing both these classes of metasurfaces, and understanding the effects of the geometrical parameters and material properties of their macroscopic optical response. The results of full-wave simulations are also reported to confirm the effectiveness of the theoretical findings.

1. Introduction

Metasurfaces are composite bi-dimensional surfaces engineered in such a way as to mold the flow of the impinging field in an unconventional manner [1-4]. Over the last years, metasurfaces have proven to enable many innovative and unprecedented functionalities, such as full control of the reflected and transmitted fields [5-7], perfect absorption [8], polarization transformation [9], holography [10], near-diffraction-limit focusing [11], electromagnetic invisibility and illusion [12, 13], etc.

From a theoretical point of view, a metasurface is an extremely thin layer supporting electric and magnetic current densities that introduce an abrupt change in the amplitude and phase of the transmitted and reflected electromagnetic field. Given the sub-wavelength size of their elements and the electrically small separation distance among them, metasurfaces are homogenizable in the surface plane [1]. A convenient way to describe their macroscopic behavior relies on the concept of the surface impedance. In particular, for a linear metasurface without magneto-electric coupling, the relationship between the tangential components of the electric and magnetic fields across the metasurface plane can be expressed as follows:

$$\begin{bmatrix} \mathbf{E}_t^+ \\ \mathbf{E}_t^- \end{bmatrix} = \begin{bmatrix} \underline{\mathbf{Z}}_s^e & 0 \\ 0 & \underline{\mathbf{Z}}_s^m \end{bmatrix} \bullet \begin{bmatrix} \hat{\mathbf{n}} \times \mathbf{H}_t^+ \\ \hat{\mathbf{n}} \times \mathbf{H}_t^- \end{bmatrix}, \qquad (1)$$

where $\underline{\mathbf{Z}}_s^e$ and $\underline{\mathbf{Z}}_s^m$ are respectively the 2×2 electric and magnetic surface-impedance dyadics of the metasurface, which reduce to scalar quantities if the metasurface is isotropic. The elements of the surface-impedance dyadic are in general complex quantities, the real and imaginary parts of which are related with the losses and the reactive behavior of the metasurface, respectively. The possibility of designing a real structure exhibiting a desired value of the complex surface impedances at a given frequency is one of the current research directions of this field.

In this context, the design and characterization of metasurfaces operating at radio frequencies and microwaves is well established. In fact, the first analytical models of some simple artificial surfaces realized through sub-wavelength metallic strips can be dated back to the fifties [14]. Models

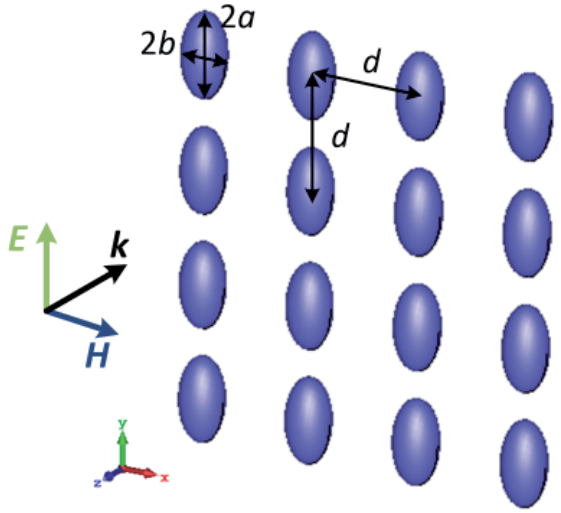

Figure 1a. A square array of spheroidal nanoparticles illuminated by a normally impinging plane wave.

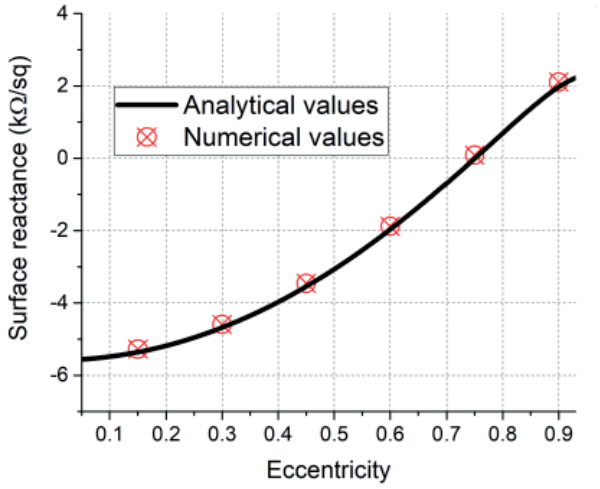

Figure 1b. The surface reactance of a plasmonic metasurface as a function of the eccentricity of its nanoparticles. The ticks are the results of numerical simulations.

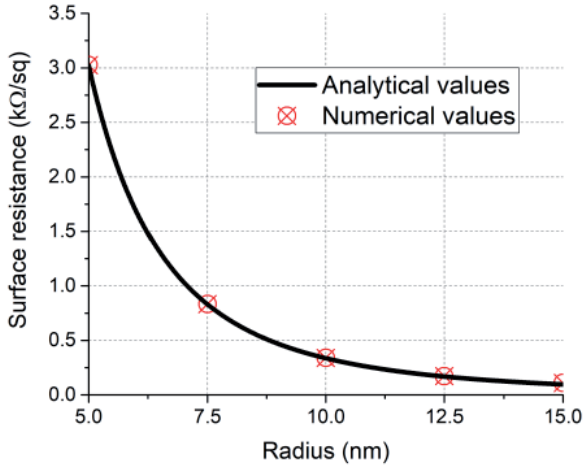

Figure 1c. The surface resistance of a plasmonic metasurface as a function of the radius of its nanoparticles. The ticks are the results of numerical simulations.

and design procedures were later generalized and extended to different geometries [15-18], while more recently, the use of resistive metasurfaces was investigated for the design of electromagnetic absorbers and radar-cross-section reduction devices [19, 20]. The current trend of this field is focused on the design of tunable devices the complex surface impedance of which can be controlled in real time [21]. Conversely, the design and characterization of optical metasurfaces is an emerging topic fostered by the terrific improvements of nanofabrication techniques. Different approaches have been proposed to design a metasurface exhibiting a desired value of the complex surface impedance at optical frequencies. Among them, the approach based on the use of nanoparticle arrays is particular promising, because of its flexibility and variety of applications [22].

In this paper, we review our recent efforts in the definition of effective analytical models and procedures for designing optical metasurfaces made of nanoparticles. We first show that the coupled dipole model is a simple and viable solution for describing the macroscopic behavior of metasurfaces made either of plasmonic or dielectric nanoparticles. We also show how the availability of an effective model allows an in-depth understanding of the complex scattering response of these structures, as well as estimating the effects of the geometry and material properties on their performance. Finally, we discuss and comment on several innovative applications of these optical metasurfaces, spanning from the design of scattering-control devices to the design of ultra-thin optical mirrors.

2. Analytical Models

A sketch of the reference geometry investigated in this paper is shown in Figure 1a. It consisted of a square array of spheroidal nanoparticles illuminated by an external plane wave the electric field of which was parallel to the particles' major axis. We assumed that the nanoparticles were embedded into a non-magnetic material with relative permittivity ε_h , and that their size and separation distance, d, were sub-wavelength, i.e., they were both small compared to the free-space wavelength. The size of the nanoparticles and their constituent material determined the electromagnetic modes excited within each particle. In the following, we considered two different scenarios that are both very popular in modern nanophotonics research. In the first case, the nanoparticles were made of a plasmonic material with negative relative permittivity at optical frequencies. In the second scenario, the nanoparticles were instead made of a high-index dielectric material. As will be clear later, the effects to be accounted for and the relative analytical models were different in the two cases.

2.1 Plasmonic Metasurfaces

We started by considering the case of *plasmonic nanoparticles*, which can be described as a lattice of ionic

cores in which the conduction electrons move almost freely. An external electromagnetic field applied to these structures originates a force on the electrons, which pushes them toward the surface of the nanoparticles and creates an electric dipole. Since the assumptions of the coupled dipole moment [17] are satisfied, we can express the *y* component of the complex surface impedance, Z_e^y, of a regular array of parallel electric dipoles as follows:

$$\frac{Z_e^y}{\eta_h} = -\frac{d^2}{k}\left\{\left[\mathrm{Im}\left(\alpha_e^{-1}\right) - \frac{k^3}{6\pi}\right] + \left[\mathrm{Re}\left(\alpha_e^{-1} - \beta_e\right)\right]\right\} \quad (2)$$

$$= -i\frac{d^2}{k}\mathrm{Re}\left(\alpha_e^{-1} - \beta_e\right),$$

with η_h being the intrinsic impedance of the host material, *k* being the wavenumber within the host material, α_e being the electric polarizability of the nanoparticle, and β_e being the interaction constant among the particles.

Given the reduced electrical size of the nanoparticles, we can approximate α_e with the static polarizability of a spheroidal particle, which gives [23]

$$\alpha_e = \frac{V}{L + \dfrac{\varepsilon_h}{\varepsilon - \varepsilon_h}}, \quad (3)$$

with *V* being the volume of the nanoparticle, ε being its relative permittivity, and *L* being the so-called depolarization factor, which accounts for the elongated shape of the particles. The interaction among the nanoparticles is accounted for by the term β_e, approximate expressions for which can be found in [24]. It is worth underlining that the polarizability, Equation (3), does not include the radiation losses, which play a role even for lossless scatterers [25]. As a consequence, the real part of the surface impedance, Equation (2), is different from zero even if all the materials involved are lossless. This error, which does not significantly affect the subsequent discussions as its practical impact is very limited, can be eliminated by adding a radiation-damping correction to the static polarizability.

To compute the value of Z_e^y, all we need now is to specify the dielectric function describing the response of the plasmonic material composing the nanoparticles. As clarified above, the nanoparticles are much smaller than the free-space wavelength λ_0, i.e., their radius is lower than $\lambda_0/10$. Since we are considering applications in the optical spectrum, in which the wavelength varies between 400 nm to 700 nm, we have to assume that the corresponding nanoparticle size may be lower than the mean free path of electrons, λ_{rt}, in many of the most common plasmonic materials (i.e., $\lambda_{rt} \sim 50$ nm for silver). As a consequence, the optical losses of these particles are higher compared to those of the material because of the surface dispersion effect of the electrons with the nanoparticle boundaries. The conventional Drude-Lorentz model used to describe the optical response of plasmonic materials is thus not effective anymore, since it may underestimate the overall optical losses of the nanoparticles. A simple way to account for the surface dispersion relies on the definition of a size-corrected dielectric function that depends on the electrical size of the nanoparticles [23]. For the case at hand, in which the nanoparticles have different characteristic dimensions along the three axis, the dielectric function becomes anisotropic, and can be written as

$$\varepsilon_i(\omega, r_i) = 1 - \frac{\omega_p^2}{\omega\left[\omega - j\left(\gamma + A\dfrac{\nu_F}{r_i}\right)\right]} + \frac{f\omega_L^2}{\omega_L^2 - \omega^2 + j\Gamma_L\omega},$$

$$i = x, y, z. \quad (4)$$

For the case of silver, the values of the parameters appearing in Equation (4) are $\omega_p = 9.17$ eV, $\omega_L = 5.27$ eV, $f = 2.2$ $\Gamma_L = 1.14$ eV, $\gamma = 0.0023\omega_p$, $\nu_F = 1.39\times10^6$ m/s, and $A = 0.6$.

Equations (2)-(4) provide all the elements to compute the complex surface impedance exhibited by an array of elongated particles illuminated by an external plane wave the electric field of which is parallel to the particle's major axis. By properly combining these equations, we get to the following explicit expressions:

$$\mathrm{Re}\left[Z_e^y\right] = R_e^y \quad (5)$$

$$= \frac{a^2\varepsilon_h\left[A_1\omega^2\Gamma_L\omega_L^2 + \dfrac{r_y\omega_p^2 B}{A_1^2\nu_f^2 + 2A_1 r_y\nu_f\gamma + r_y^2\left(\gamma^2+\omega^2\right)}\right]}{kV\omega\left[\left(-1 + A_2 + C + \varepsilon_h\right)^2 + \left(\dfrac{BC}{r_y\omega} + A_1\omega\Gamma_L\omega_L^2\right)^2\right]}$$

$$\mathrm{Im}\left[Z_e^y\right] = X_e^y = \frac{1}{4k}\left\{-\frac{4a^2R_0L_i - V + Vk^2R_0^2}{VR_0}\right.$$

$$\left. + \frac{4a^2\varepsilon_h\left(-1 + C + \epsilon_h + A\omega^2\omega_L^2 - A\omega_L^4\right)}{V\left[\left(-1 + A_2 + C + \varepsilon_h\right)^2 + \left(\dfrac{BC}{r_y\omega} + A\omega\Gamma_L\omega_L^2\right)^2\right]}\right\}$$

with

$$A_1 = \frac{f}{\omega^2\Gamma_L^2 + \left(\omega^2 - \omega_L^2\right)^2},$$

$$A_2 = A_1\omega_L^2\left(\omega^2 - \omega_L^2\right), \qquad (6)$$

$$B = \left(A_1 v_f + r_y\gamma\right),$$

$$C = \omega_p^2 \Big/ \left(\frac{B^2}{r_y^2} + \omega^2\right).$$

What we look for is a design strategy that allows us to independently tailor the real and the imaginary parts of the optical surface impedance.

For this purpose, we investigated the effects of two different geometrical parameters of the nanoparticles – the eccentricity and the absolute size – on the complex average surface impedance exhibited by the array. In Figure 1b, we show the variation of the surface reactance of an array of spheroidal silver nanoparticles as the eccentricity, *e*, changed from 0 (i.e., spheres) to values close to 1 (i.e., strongly elongated ellipsoids). These results were obtained by considering a metasurface with a period $a = 35$ nm and an operating frequency of $f_0 = 800$ THz ($\lambda_0 = 400$ nm). The theoretical results (solid line) were compared with the results obtained by implementing a retrieval procedure in full-wave simulation software (red ticks). As could be appreciated, the nanoparticle eccentricity represented a possible degree of freedom to tune the surface reactance within a wide range of possible values, from strongly capacitive up to strongly inductive.

In Figure 1c, we instead show the variation of the surface resistance of the metasurface as the radius of the nanoparticles changed. In this case, we considered a metasurface made of spherical nanoparticles and we assumed the same period and operating frequency as the previous example. As it could be appreciated, there was a significant increase in the surface resistance of the metasurface as the nanoparticle's radius reduced. This effect was due to the surface dispersion of the nanoparticles, and confirmed that the size-correction of their dielectric function was crucial to properly describing the optical response of this family of metasurfaces.

From the above discussion, we can conclude that by properly changing the eccentricity and the absolute size of the nanoparticles it is possible to achieve all the possible combinations of surface resistance and reactance that are needed in several applications. Some examples will be provided in the next section.

2.2 All-Dielectric Metasurfaces

A second class of optical metasurfaces that have been very popular in the last years are the so-called all-dielectric metasurfaces [26-33]. These consist of an array of nanoparticles made of a high-index dielectric material with a size comparable with the wavelength inside the dielectric (but still small compared to the free-space wavelength). When excited by an external field, these particles – also known as Mie resonators – support both an electric and a magnetic resonance. Moreover, since the resonances of the high-index nanoparticles originate from the displacement currents, their non-radiative optical losses are very low, with important advantages over their plasmonic counterparts.

From a modeling point of view, two important differences compared to the case of plasmonic metasurfaces need to be considered. The first difference is due to the fact that Mie resonators support a magnetically induced dipole moment in addition to the conventional dipolar electric mode. An array of such resonators thus supports both electric and magnetic current densities. If we focus our analysis on the case of spherical nanoparticles, which have an isotropic response on the plane of the metasurface, the electric surface impedance and magnetic surface admittance can be expressed as follows:

$$\begin{cases} \dfrac{Z_e}{\eta_h} = -i\dfrac{d^2}{k}\mathrm{Re}\left[\alpha_e^{-1} - \beta_e\right], \\ \eta_h Y_m = -i\dfrac{d^2}{k}\mathrm{Re}\left[\alpha_m^{-1} - \beta_m\right], \end{cases} \qquad (7)$$

where α_e (α_m) is the electric (magnetic) polarizability of the individual particle, and β_e (β_m) is the interaction constant among electric (magnetic) dipoles induced in the array. In Equation (7), the expression of the magnetic surface admittance was derived by duality. The reflection and transmission coefficient by a homogenous sheet characterized by the parameters in Equations (7) can be calculated as

$$\Gamma = \frac{-\eta_0}{2Z_e + \eta_0} + \frac{Z_m}{Z_m + 2\eta_0}, \qquad (8)$$

$$T = 1 - \frac{\eta_0}{2Z_e + \eta_0} - \frac{Z_m}{Z_m + 2\eta_0},$$

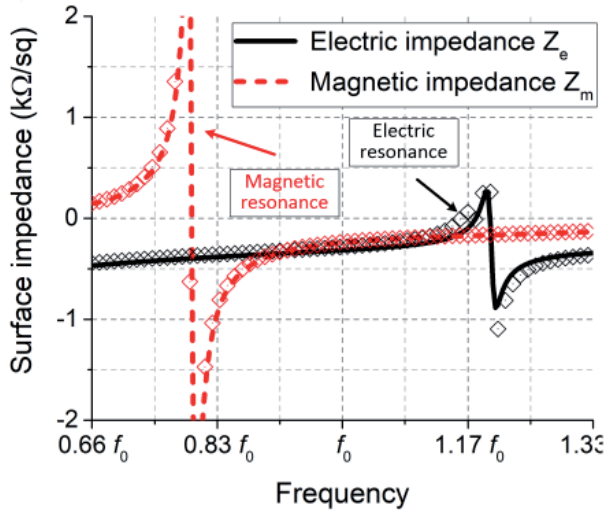

Figure 2a. The electric and magnetic surface impedances of the all-dielectric metasurface described in the main text for $d = 0.14\lambda_0$. The ticks represent the results of full-wave numerical simulations.

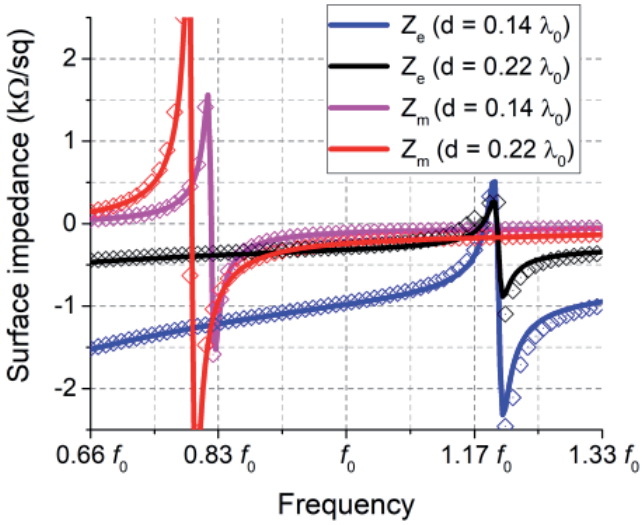

Figure 2b. The effect of the separation distance on the electric and magnetic resonances exhibited by the all-dielectric metasurfaces. The ticks represent the results of full-wave numerical simulations.

with η_0 being the free-space impedance.

The second fundamental difference between dielectric metasurfaces compared to plasmonic metasurfaces is related to the expression of the nanoparticle polarizabilities. In fact, in this case the size of the individual element is comparable with the wavelength inside the material. The static polarizability, Equation (3), used for the case of plasmonic metasurfaces is thus not effective anymore and would return inaccurate results. To this end, we need a more-precise description of the dynamic response of the nanoparticles, such as the description based on the Mie scattering coefficients [34, 35]. In particular, for the case of spherical nanoparticles, we can write

$$\alpha_e = -i\left(\frac{6\pi}{k^3}\right)a_1$$

$$= -i\left(\frac{6\pi}{k^3}\right)$$

$$\left[\frac{\sqrt{\varepsilon}\psi_1\left(\sqrt{\varepsilon}x\right)\psi_1'\left(\sqrt{\varepsilon_h}x\right)-\sqrt{\varepsilon_h}\psi_1\left(\sqrt{\varepsilon_h}x\right)\psi_1'\left(\sqrt{\varepsilon}x\right)}{\sqrt{\varepsilon}\psi_1\left(\sqrt{\varepsilon}x\right)\xi_1'\left(\sqrt{\varepsilon_h}x\right)-\sqrt{\varepsilon_h}\xi_1\left(\sqrt{\varepsilon_h}x\right)\psi_1'\left(\sqrt{\varepsilon}x\right)}\right], \quad (9)$$

$$\alpha_m = -i\left(\frac{6\pi}{k^3}\right)b_1$$

$$= -i\left(\frac{6\pi}{k^3}\right)$$

$$\left[\frac{\sqrt{\varepsilon_h}\psi_1\left(\sqrt{\varepsilon}x\right)\psi_1'\left(\sqrt{\varepsilon_h}x\right)-\sqrt{\varepsilon}\psi_1\left(\sqrt{\varepsilon_h}x\right)\psi_1'\left(\sqrt{\varepsilon}x\right)}{\sqrt{\varepsilon_h}\psi_1\left(\sqrt{\varepsilon}x\right)\xi_1'\left(\sqrt{\varepsilon_h}x\right)-\sqrt{\varepsilon}\xi_1\left(\sqrt{\varepsilon_h}x\right)\psi_1'\left(\sqrt{\varepsilon}x\right)}\right],$$

where $x = ka$, $\xi_n(...)$ and $\psi_n(...)$ are the Riccati-Bessel functions, and the prime symbols denote derivatives with respect to the entire argument of the function.

In Figure 2a, we show the frequency behavior of the electric and magnetic surface impedance of an all-dielectric metasurface characterized by the following electromagnetic and geometric parameters: $\varepsilon = 100 - j(1)$, $a = b = c = 0.06\lambda_0$, and $d = 0.14\lambda_0$. The theoretical results (solid line) were compared with the numerical results (ticks), which were obtained using a retrieval procedure based on the inversion of the reflection and transmission coefficients, Equation (8). As it could be appreciated, the agreement between theoretical and numerical results was very good for both the electric and magnetic modes excited by external fields in the metasurface plane.

Instead, Figure 2b reports the behavior of the surface impedances as functions of the separation distance between nanoparticles. Two different effects could be clearly observed from these results. The first effect was a shift of the magnetic resonance that progressively approached the electric resonance as the separation distance increased. In addition, the quality factors of both the resonances, i.e., the values assumed by the surface impedances in moving away from the resonance, were significantly affected by the metasurface period. Specifically, as the separation distance

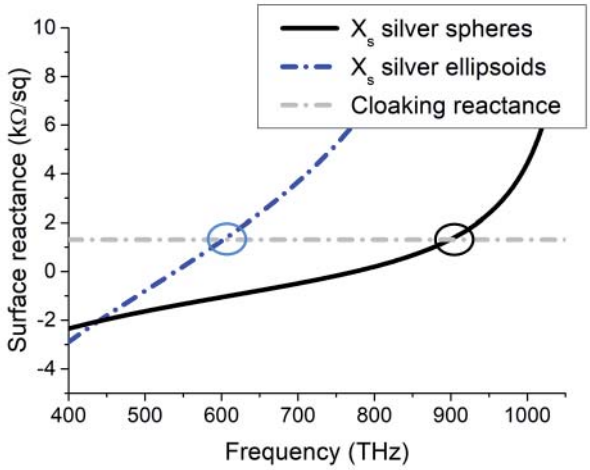

Figure 3a. The theoretical cloaking condition (grey line) and typical behavior of the surface reactance exhibited by optical metasurfaces composed of spherical and ellipsoidal nanoparticles (black and blue lines, respectively).

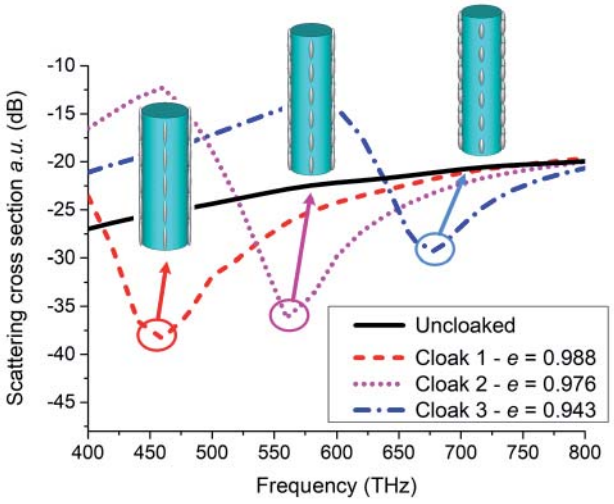

Figure 3b. The full-wave scattering cross section of a bare dielectric cylinder (black line) and of the same cylinder covered by three different metasurfaces.

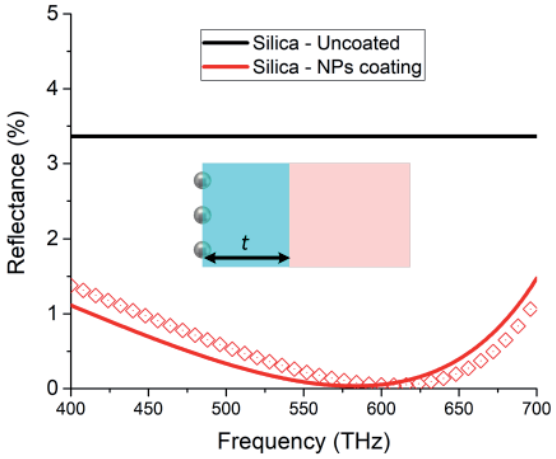

Figure 3c. The reflectance of a bare silica slab (black line) and of a silica slab covered with a capacitive metasurface (red line). The ticks are the results of numerical simulations.

increased, the quality factors of both the resonances reduced. The possibility of controlling the resonance frequency of the magnetic mode and the quality factor of both the electric and magnetic resonances provides two important degrees of freedom in the design of nanophotonic devices, as we will discuss later.

3. Applications of Plasmonic Metasurfaces: Scattering Cancellation and Perfect Absorption

In this section, we describe some of the possible applications of the plasmonic metasurfaces that we have investigated in the last years. In all the considered cases, the availability of an analytical model allowed a better understanding of the underlying physics, as well as achieving a final working design without the need for extensive numerical optimizations.

We started by considering the possibility of using a plasmonic metasurface to cloak objects. With the term *electromagnetic cloaking* we refer to the possibility, enabled by metamaterials, to significantly reduce the overall scattering cross section of an object illuminated by an external field without increasing its absorption. One of the most popular approaches to achieve cloaking of sub-wavelength objects is the so-called scattering cancellation [36, 37]. This approach requires covering the object to be hidden with a conformal coat, which can be either a bulk volumetric metamaterial [36] or an extremely thin metasurface [37], designed in such a way to scatter a field out of phase with the field scattered by the object itself. While the design of cloaking devices working at microwave frequencies is well consolidated [38-41], there are still some challenges in the design of optical scattering cancellation cloaks. The first attempts in this direction were discussed in [42, 43]. Specifically, it was shown that an array of spherical silver nanoparticles does reduce the total scattering of a dielectric object, but only at frequencies higher than the visible range. The availability of a bi-dimensional homogenization model for plasmonic metasurfaces, such as the model we presented in the previous section, allows better understanding the macroscopic response of these structures and engineering their behavior within the optical range.

As an example, in Figure 3a we report the theoretical surface reactance (grey line) needed to cloak a dielectric cylinder made of silica as the frequency changes. The cloaking surface reactance, which is clearly inductive, is equal to [37]

$$X_s^{cloak} = \frac{2}{\omega r \gamma \varepsilon_0 \left(\varepsilon_{obj} - 1\right)}, \qquad (10)$$

with r being the radius of the cylinder, γ being the ratio between the radius of the cover and the radius of the cylinder, and ε_{obj} being the relative permittivity of the dielectric cylinder ($\varepsilon_{obj} = 2.1$ for silica). The black line in Figure 3a instead shows the frequency variation of the surface impedance of an array of silver spherical nanoparticles with radius $a = 5$ nm. As could be appreciated, the surface impedance of this metasurface matches the required surface impedance only quite above the optical spectrum and, indeed, spherical silver nanoparticles have been used for cloaking dielectric objects at ultraviolet frequencies [43]. However, as it should be clear from the discussion in the previous section, we can tune the imaginary part of the surface impedance of plasmonic metasurfaces by acting on the eccentricity of their elements [44, 45]. The blue line in Figure 3a shows the surface reactance of an array of silver ellipsoids with axis $a = 20$ nm and $b = 5$ nm. As expected, this metasurface hit the cloaking condition in the visible range at a frequency that depended on the eccentricity of the nanoparticles. As a confirmation of these theoretical considerations, in Figure 3b we show the total scattering cross section of a dielectric cylinder covered by three different optical metasurfaces, evaluated using full-wave simulation software. The three metasurfaces, which only differed for the eccentricity of their elements, were able to return a significant reduction of the total object scattering at a desired frequency of the visible range.

As an additional example, we considered the cloaking of a semi-infinite dielectric slab. For this purpose, we investigated the effect of a plasmonic metasurface placed at a certain distance from the slab, as shown in the inset of Figure 3c. The theoretical analysis of such a structure (see [46]) revealed that a capacitive metasurface was needed to minimize the overall reflected field. In accord with the results discussed in the previous section, an array of spherical plasmonic nanoparticles is capacitive within the whole optical spectrum, and thus it can be engineered to satisfy the cloaking condition. The full-wave results for both an uncovered and a covered silica slab are shown in Figure 3c. The geometrical parameters used for this example were $r = 19$ nm, $a = 67$ nm, $t = 61$ nm (corresponding to a surface reactance of $X_s = -1231$ Ω/sq at 544 THz). As could be appreciated, the overall reflectance of the slab was minimized within the whole optical spectrum due to the superimposed capacitive cloak, which behaved as a shunt-matching capacitance between the slab and free space.

A second possible application of plasmonic metasurfaces is the design of perfect optical absorbers [47, 48]. This application is enabled by the surface dispersion effect that allows tuning the average surface resistance of a plasmonic metasurface by acting on the absolute size of its elements. To better explain this point, we considered

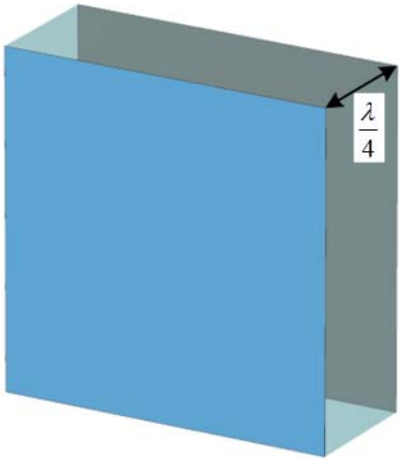

Figure 4a. A sketch of a Salisbury screen.

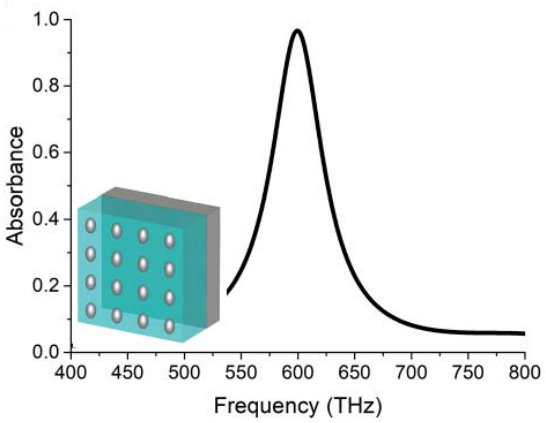

Figure 4b. The performance of an optical Salisbury screen in which the resistive sheet is implemented through an array of ellipsoidal nanoparticles.

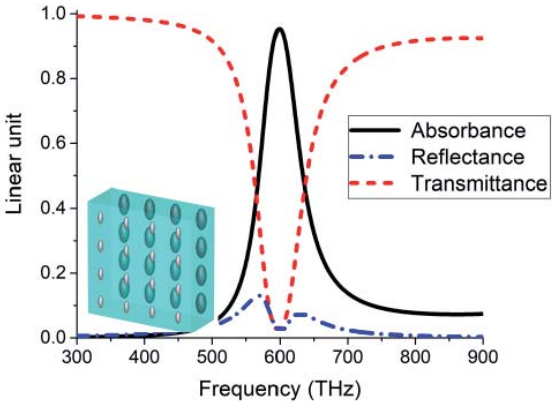

Figure 4c. The performance of a variant of the optical Salisbury screen that is transparent outside its absorption bandwidth. This effect was achieved by replacing the ground plane with an optical metasurface working as a perfect electric conductor only within a narrow frequency range.

the basic geometry of a Salisbury absorber, shown in Figure 4a, which is composed of a ground plane, a $\lambda/4$ dielectric spacer, and a resistive sheet. The resistive sheet can be considered as a resonant metasurface (i.e., $X_s = 0$ Ω/sq) the surface resistance of which is matched to the free-space intrinsic impedance (i.e., $R_s = \eta_0 = 377$ Ω/sq). In accordance with the theoretical findings discussed in the previous section, an optical resistive sheet can be designed by engineering the absolute size and the eccentricity of the nanoparticles composing a plasmonic metasurface [47].

In Figure 4b, we show the performance evaluated using full-wave numerical software of an optical absorber made of a plasmonic metasurface placed $\lambda/4$ apart from a thick layer of silver, which behaved as a ground plane. The metasurface was designed using Equation (5) to satisfy the above-mentioned requirements at the center of the optical spectrum ($f_0 = 600$ THz), and was characterized by the following parameters: $a = 13$ nm, $b = c = 5$ nm, and $d = 55$ nm. As could be appreciated, when illuminated by a plane wave with the electric field parallel to the major axis of the ellipsoids, the structure fully absorbed the impinging light at the design frequency.

A possible variant of this structure is shown in the inset of Figure 4c. In this case, the backing layer was replaced by a second plasmonic metasurface, which was designed to behave as a perfect electric conductor (i.e., $Z_s = 0$ Ω/sq) only within the absorber bandwidth. Consequently, this device worked as a Salisbury screen only in a narrow frequency range around the design frequency, while being almost completely transparent outside it (Figure 4c). Compared to other approaches that have been proposed for designing devices that do not affect the light propagation outside their operating bandwidth [49], the proposed approach ensures a broadband transparency, since the small size of the nanoparticles moves away the undesired effects of the higher-order modes.

4. Applications of Dielectric Metasurfaces: Optical Mirrors

As clarified above, dielectric metasurfaces offer improved flexibility over their plasmonic counterparts because of their reduced losses, and the fact that they exhibit a magnetic surface impedance. We have also discussed how the separation distance among the nanoparticles allows tuning the magnetic resonance and the quality factors of the both the electric and magnetic resonance. These degrees of freedom have recently been exploited for designing single-layer dielectric mirrors [29] the thickness of which was much lower than conventional Bragg reflectors. Here, we show that the coupled-dipole model discussed above allows an in-depth understanding of the complex scattering responses of these structures, and provides effective design tools.

The structure we considered is shown in Figure 5a. It consists of an array of spherical dielectric nanoparticles made of c-Si, which is one of the most popular materials used in nanophotonics, given its reduced losses and high refractive index (i.e., real part of the relative permittivity higher than 12 within the entire optical spectrum) [50]. For our analysis, the dielectric was modeled by interpolating its measured complex permittivity. As a design tool, we defined the quantity $\overline{R}(a,d)$ as the integral of the normalized amplitude of the reflection coefficient, Equation (8), within a chosen frequency range $[f_1, f_2]$, i.e.,

$$\overline{R}(a,d) = \int_{f_{min}}^{f_{max}} \left[\frac{|\Gamma(a,d,f)|}{f_{max} - f_{min}} \right] df \,. \qquad (11)$$

From the definition, it is clear that the maximum value of Equation (11) is $\overline{R}(a,d) = 1$ and, when this applies, the magnitude of the reflection coefficient, $\Gamma(a,d,f)$, is equal

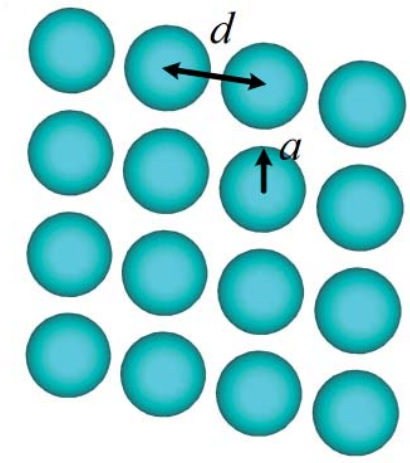

Figure 5a. A sketch of an all-dielectric metasurface made of spherical particles.

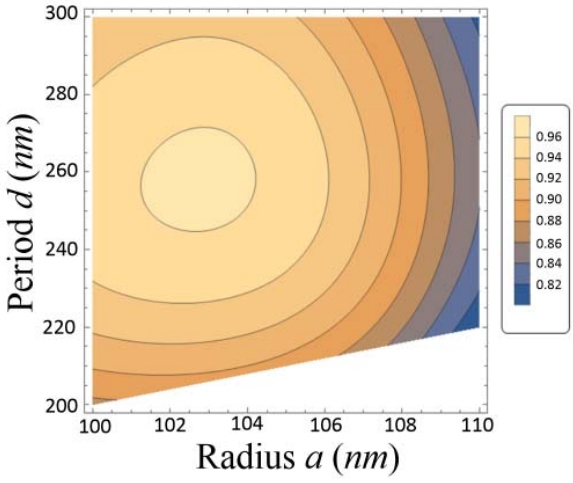

Figure 5b. The values of $\overline{R}(a,d)$ for different values of the nanoparticle radius and metasurface period.

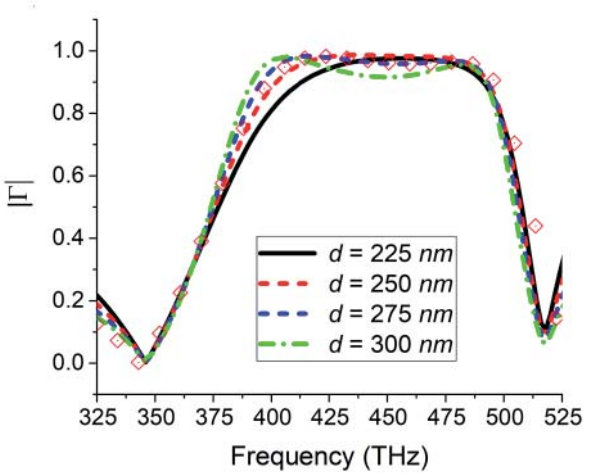

Figure 5c. The frequency behavior of the reflection coefficient of a c-Si dielectric metasurface for different separation distances. The ticks are the results of full-wave simulations.

to 1 within all the chosen frequency range. In Figure 5b, we show the value assumed by the quantity in Equation (11) for different nanoparticle radii, a, and separation distances, d (which, for geometrical constraints, were assumed to be higher than $2a$). In this example, we chose $f_{min} = 500$ THz and $f_{max} = 600$ THz. As expected, the maximum value of $\overline{R}(a,d)$ was achieved when the radius of the nanoparticles was close to $\lambda/2$, with λ being the wavelength inside the dielectric at the center frequency of the considered range. This is consistent with the so-called Kerker condition [51] of the individual nanoparticle. Nevertheless, the separation distance among the nanoparticles plays an important role given its effects on the resonance frequencies and on the quality factor of the resonances. This can be appreciated even better in Figure 5c, where the magnitudes of the reflection coefficient when $a = 104$ nm for different values of d are shown. As could be appreciated, there was a value d ($d = 250$ nm) that optimized the reflection of the structure and transformed the dual-band reflection behavior into a single broadband behavior. Also in this case, the theoretical results were compared with the full-wave results, showing excellent agreement within the reflection bandwidth. Before concluding, it is worth mentioning that in this example, the nanoparticles' size did not strictly satisfy the homogenization requirements. In fact, the non-extreme value of the relative permittivity of c-Si implies the use of particles with a radius that is larger than $\lambda_0/10$. Nevertheless, the coupled-dipole model is effective even in these non-ideal scenarios, and provides a powerful tool for describing the response of a wide class of all-dielectric optical metasurfaces.

5. Conclusions

In this paper, we reviewed our recent efforts in the theoretical modeling of optical metasurfaces consisting of an arrangement of spheroidal nanoparticles. We have investigated both the cases of plasmonic and dielectric nanoparticles, and shown that their electromagnetic responses can be effectively described by proper use of the coupled-dipole model. The theoretical formulation allowed the definition of several design strategies aimed at controlling the optical complex surface impedances exhibited by these structures. In particular, it was shown that the real and imaginary parts of the electric surface impedance of a plasmonic metasurface can be tailored by acting on the size and eccentricity of the nanoparticles, respectively. In addition, the effects of the separation distance on the electric and magnetic resonances of dielectric metasurfaces were discussed. Several possible applications, including the design of scattering-reduction devices, optical absorbers, and perfect mirrors, were discussed and validated through full-wave numerical simulations.

6. References

1. C. L. Holloway, E. F. Kuester, J. A. Gordon, J. O'Hara, J. Booth, and D. R. Smith, "An Overview of the Theory and Applications of Metasurfaces: The Two-Dimensional Equivalents of Metamaterials," *IEEE Transaction on Antennas Propagation*, **54**, 2012, pp. 10-35.

2. S. B. Glybovski, S. A. Tretyakov, P. A. Belov, Y. S. Kivshar, and C. R. Simovski, "Metasurfaces: From Microwaves to Visible," *Physics Reports*, **634**, 2016, pp. 1-72.

3. H.-T. Chen, A. J. Taylor, and N. Yu, "A Review of Metasurfaces: Physics and Applications," *Reports on Progress in Physics*, **79**, 2016, 076401.

4. A. Li, S. Singh, and D. Sievenpiper, "Metasurfaces and Their Applications," *Nanophotonics*, **7**, 2018, pp. 989-1011.

5. N. Yu, P. Genevet, M. A. Kats, F. Aieta, J.-P. Tetienne, F. Capasso, and Z. Gaburro, "Light Propagation with Phase Discontinuities: Generalized Laws of Reflection and Refraction," *Science*, **334**, 2011, 6054.

6. C. Pfeiffer and A. Grbic, "Metamaterial Huygens' Surfaces: Tailoring Wave Fronts with Reflectionless Sheets," *Physical Review Letters*, **110**, 2013, 197401.

7. S. A. Tretyakov, "Metasurfaces for General Transformations of Electromagnetic Fields," *Philosophical Transactions of the Royal Society A*, **373**, 2015, 20140362.

8. Y. Ra'di, R. Simovski, and S. A. Tretyakov, "Thin Perfect Absorbers for Electromagnetic Waves: Theory, Design, and Realizations," *Physical Review Applied*, **3**, 2015, 037001.

9. E. Doumanis, G. Goussetis, J. Gomez-Tornero, R. Cahill, and V. Fusco, "Anisotropic Impedance Surfaces for Linear to Circular Polarization Conversion," *IEEE Transaction on Antennas and Propagation*, **60**, 2012, pp. 212-219.

10. B. Fong, J. Colburn, J. Ottusch, J. Visher, and D. Sievenpiper, "Scalar and Tensor Holographic Artificial Impedance Surfaces," *IEEE Transactions on Antennas and Propagation*, **58**, 2010, pp. 3212-3221.

11. F. Monticone, N. M. Estakhri, and A. Alù, "Full Control of Nanoscale Optical Transmission with a Composite Metascreen," *Physical Review Letters*, **110**, 2013, 203903.

12. A. Alù, "Mantle Cloak: Invisibility Induced by a Surface," *Physical Review B*, **80**, 2009, 245115.

13. S. Vellucci, A. Monti, A. Toscano, and F. Bilotti, "Scattering Manipulation and Camouflage of Electrically Small Objects Through Metasurfaces," *Physical Review Applied*, **7**, 2017, 034032.

14. N. Marcuvitz, *Waveguide Handbook*, New York, NY, McGraw-Hill, 1951.

15. R. Ulrich, "Far Infrared Properties of Metallic Mesh and its Complementary Structure," *Infrared Phys*ics, **7**, 1967, pp. 37-55.

16. L. B. Whitbourn and R. C. Compton, "Equivalent-Circuit Formulas for Metal Grid Reflectors at a Dielectric Boundary," *Applied Optics*, **24**, 1985, pp. 217-220.

17. S. Tretyakov, *Analytical Modeling in Applied Electromagnetics*, Norwood, MA, Artech House, 2003.

18. O. Luukkonen, C. Simovski, G. Granet, G. Goussetis, D. Lioubtchenko, A. V. Raisanen, and S. A. Tretyakov, "Simple and Accurate Analytical Model of Planar Grids and High-Impedance Surfaces Comprising Metal Strips or Patches," *IEEE Transactions on Antennas and Propagation*, **56**, 2008, pp. 1624-1632.

19. F. Costa, A. Monorchio, and G. Manara, "Analysis and Design of Ultra Thin Electromagnetic Absorbers Comprising Resistively Loaded High Impedance Surfaces," *IEEE Transactions on Antennas and Propagation*, **58**, 2010, pp. 1551-1558.

20. Q. Chen, M. Guo, D. Sang, Z. Sun, Y. Fu, " RCS Reduction of Patch Array Antenna Using Anisotropic Resistive Metasurface," *IEEE Antennas and Wireless Propagation Letters*, **18**, 2019, pp. 1223-1227.

21. F. Liu, O. Tsilipakos, A. Pitilakis, A.C. Tasolamprou, M. Sajjad Mirmoosa, N. V. Kantartzis, D. H. Kwon, J. Georgiou, K. Kossifos, M. A. Antoniades, M. Kafesaki, C. M. Soukoulis, and S. A. Tretyakov, "Intelligent Metasurfaces with Continuously Tunable Local Surface Impedance for Multiple Reconfigurable Functions," *Physical Review Applied*, **11**, 2019, 044024.

22. M. I. Stockman, "Nanoplasmonics: Past, Present, and Glimpse into Future," *Optic Express*, **19**, 2011, pp. 22029-22106.

23. C. Noguez, "Optical Properties of Isolated and Supported Metal Nanoparticles," *Optical Materials*, **27**, 2005, 1204.

24. M. Yazdi and M. Albooyeh, "Analysis of Metasurfaces at Oblique Incidence," *IEEE Transactions on Antennas and Propagation*, **65**, 2017, pp. 2397-2404.

25. P. Belov, S. I. Maslovski, K. R. Simovski, and S. A. Tretyakov, "A Condition Imposed on the Electromagnetic Polarizability of a Bianisotropic Lossless Scatterer," *Technical Physics Letters*, **29**, 2003, pp 718-720.

26. J. Cheng, D. Ansari-Oghol-Beig, and H. Mosallaei, "Wave Manipulation with Designer Dielectric Metasurfaces," *Optics Letters*, **39**, 2014, pp. 6285-6288.

27. J. Sautter et al., "Active Tuning of All-Dielectric Metasurfaces," *ACS Nano*, **9**, 2015, pp. 4308-4315.

28. B. S. Luk'yanchuk, N. V. Voshchinnikov, R. Paniagua-Domínguez, and A. I. Kuznetsov, "Optimum Forward Light Scattering by Spherical and Spheroidal Dielectric Nanoparticles with High Refractive Index," *ACS Photonics*, **2**, 2015, pp 993-999.

29. P. Moitra, B. A. Slovick, W. Li, I. I. Kravchencko, D. P. Briggs, S. Krishnamurthy, and Jason Valentine, "Large-Scale All-Dielectric Metamaterial Perfect Reflectors," *ACS Photonics*, **2**, 2015, pp. 692-698.

30. A. Arbabi, Y. Horie, M. Bagheri, and A. Faraon, "Dielectric Metasurfaces for Complete Control of Phase and Polarization with Subwavelength Spatial Resolution and High Transmission," *Nature Nanotechnology*, **10**, 2015, pp. 937-943.

31. A. I. Kuznetsov, A. E. Miroshnichenko, M. L. Brongersma, Y. S. Kivshar, and B. Luk'yanchuk, "Optically Resonant Dielectric Nanostructures," *Science*, **354**, 2016, 2472.

32. A. Cordaro, H. Kwon, D. Sounas, A. F. Koenderink, A. Alù, and A. Polman, "High-Index Dielectric Metasurfaces Performing Mathematical Operations," *arXiv*, 2019, 1903.08402.

33. R. Jacobsen, A. Lavrinenko and S. Arslanagic, "Water-Based Metasurfaces for Effective Switching of Microwaves," *IEEE Antennas Wireless Propagation Letters*, **17**, 2018, pp. 571-574.

34. A. Alù and N. Engheta, "Polarizabilities and Effective Parameters for Collections of Spherical Nanoparticles Formed by Pairs of Concentric Double-Negative, Single-Negative, and/or Double-Positive Metamaterial Layers," *Journal of Applied Physics*, **97**, 2005, 094310.

35. W. T. Doyle, "Optical Properties of a Suspension of Metal Spheres," *Physical Review B*, **39**, 1989, 9852.

36. A. Alù, N. Engheta, "Achieving Transparency with Plasmonic and Metamaterial Coatings," *Physical Review E*, **72**, 2005, 016623.

37. A. Alù, "Mantle Cloak: Invisibility Induced by a Surface," *Physical Review B*, **80**, 2009, 24115.

38. Y. R. Padooru, A. B. Yakovlev, P. Y. Chen, and A. Alù, "Analytical Modeling of Conformal Mantle Cloaks for Cylindrical Objects Using Sub-Wavelength Printed and Slotted Arrays," *Journal of Applied Physics*, **11**, 2012, 034907.

39. A. Monti, J.C. Soric, A. Alù, A. Toscano, F. Bilotti, "Anisotropic Mantle Cloaks for TM and TE Scattering Reduction," *IEEE Transaction on Antennas and Propagation*, **63**, 2015, pp. 1775-1788.

40. J. C. Soric, A. Monti, A. Toscano, F. Bilotti, and A. Alù, "Dual-Polarized Reduction of Dipole Antenna Blockage Using Mantle Cloaks," *IEEE Transactions on Antennas and Propagation*, **63**, 2015, pp. 4827-4834.

41. J. C Soric, A. Monti, A. Toscano, F. Bilotti, and A. Alù, "Multiband and Wideband Bilayer Mantle Cloaks," *IEEE Transactions on Antennas and Propagation*, **63**, 2015, pp. 3235-3240.

42. S. Mühlig, M. Farhat, C. Rockstuhl, and F. Lederer, "Cloaking Dielectric Spherical Objects by a Shell of Metallic Nanoparticles," *Physical Review B*, **83**, 2011, 195116.

43. S. Mühlig, A. Cunningham, J. Dintinger, M. Farhat, S. B. Hasan, T. Scharf, T. Bürgi, F. Lederer, and C. Rockstuhl, "A Self-Assembled Three-Dimensional Cloak in the Visible," *Scientific Reports*, **3**, 2013, 2328.

44. A. Monti, A. Alù, A. Toscano, and F. Bilotti, "Optical Invisibility Through Metasurfaces Made of Plasmonic Nanoparticles," *Journal of Applied Physics*, **117**, 2015,123103.

45. M. Fruhnert, A. Monti, I. Fernandez-Corbaton, A. Alù, A. Toscano, F. Bilotti, and C. Rockstuhl, "Tunable Scattering Cancellation Cloak with Plasmonic Ellipsoids in the Visible," *Physical Review B*, **93**, 2016, 245127.

46. A. Monti, A. Alù, A. Toscano, and F. Bilotti, "Metasurface-Based Anti-Reflection Coatings at Optical Frequencies," *Journal of Optics*, **20**, 2018, 055001.

47. A. Monti, A. Toscano, and F. Bilotti, "Exploiting the Surface Dispersion of Nanoparticles to Design Optical-Resistive Sheets and Salisbury Absorbers," *Optics Letters*, **41**, 2016, pp. 3383-3386.

48. A. Monti, A. Alù, A. Toscano, and F. Bilotti, "Narrowband Transparent Absorbers Based on Ellipsoidal Nanoparticles," *Applied Optics*, **56**, 2017, pp. 7533-7538.

49. Y. Ra'di, V. S. Asadchy, S. U. Kosulnikov, M. M. Omelyanovich, D. Morits, A. V. Osipov, C. R. Simovski, and S. A. Tretyakov, "Full Light Absorption in Single Arrays of Spherical Nanoparticles," *ACS Photonics*, **2**, 2015, pp. 653-660.

50. D. G. Baranov, D. A. Zuev, S. I. Lepeshov, O. V. Kotov, A. E. Krasnok, A. B. Evlyukhin, and B. N. Chichkov, "All-Dielectric Nanophotonics: The Quest for Better Materials and Fabrication Techniques," *Optica*, **4**, 2017, pp. 814-825.

51. M. Kerker, D. S. Wang, and L. Giles, "Electromagnetic Scattering by Magnetic Spheres," *The Journal of Optical Society of America*, **73**, 1983, pp. 765-767.

Time-Modulated Reactive Elements for Control of Electromagnetic Energy

Grigorii A. Ptitcyn[1], Mohammad S. Mirmoosa[2], Viktar S. Asadchy[3], and Sergei A. Tretyakov[1]

[1]Department of Electronics and Nanoengineering Aalto University
P.O. Box 15500
FI-00076 Aalto, Finland
E-mail: grigorii.ptitcyn@aalto.fi

[2]Laboratory of Wave Engineering
École Polytechnique Fédérale de Lausanne (EPFL)
CH-1015 Lausanne, Switzerland

[3]Department of Electrical Engineering
Stanford University
Stanford, California 94305, USA
E-mail: sergei.tretyakov@aalto.fi

Abstract

Accumulation of electromagnetic field energy in classical passive structures, such as resonators and reactive circuit elements, is limited by the amplitude of time-harmonic external sources. In the steady-state regime, all incident power that is not absorbed is fully re-radiated (reflected), and the time-averaged stored energy is constant, even though the external source continuously supplies energy. We have recently shown that lossless objects can continuously accumulate energy if their properties are properly modulated in time. Here, we discuss this possibility, and study means to release this accumulated energy in the desired moment or moments of time in the form of pulses of the desired shape. Furthermore, we discuss a possibility of keeping the energy inside the load, turning off the incident wave and changing the modulation function of the load. Finally, instead of a single time-reactive element, we consider a parallel time-varying LC circuit that gives the same functionality, in addition to allowing engineering currents flowing through the load's circuit elements. This paper is an extended version of [1].

1. Introduction

The property of accumulating and releasing of energy without dissipation makes an efficient battery. Electromagnetic field energy can be stored in the form of evanescent fields or standing waves inside or near various objects, for example, in cavity resonators, in low-loss metasurfaces, and in reactive circuit elements (capacitors and inductors). If we consider reactive elements connected to a time-harmonic source, then the energy stored inside them depends on the current ($i(t)$) and voltage ($v(t)$) provided by the source, and on the element parameters: capacitance (C) and inductance (L). The stored energy is given by the equations

$$W_{\mathrm{e}}(t) = C\frac{v(t)^2}{2}, \tag{1}$$

$$W_{\mathrm{m}}(t) = L\frac{i(t)^2}{2}.$$

After the transition period, when the steady-state regime is established, the time-averaged stored energy does not grow, and all incident power is fully reflected back to the source. This is a classical limitation that is valid for stationary reactive elements connected to time-harmonic sources. It is possible to overcome this limitation by modulating the signal sent by the source. This approach was realized in [2]: an exponentially growing wave was virtually absorbed inside a dielectric slab and released after stopping the energy pump. However, modifying the source is not always an option, and in this case there is no control over the shape of the released signal. Another way to store energy is to modulate the load reactance in time [3]. In this way, one can eliminate reflection, although there is no dissipation. Since the load is reactive and energy cannot be absorbed, all the incident energy is stored. Here, we show that using a time-varying load it is possible to control reflected waves, meaning that aside from unlimited accumulation of electromagnetic energy, it is also possible

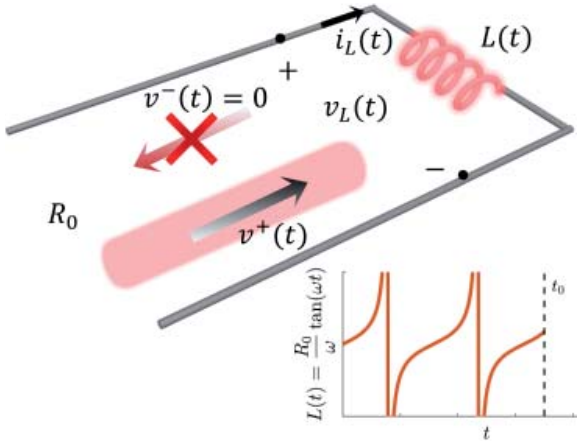

Figure 1a. A transmission line terminated by a time-dependent inductance that virtually absorbs the incoming energy.

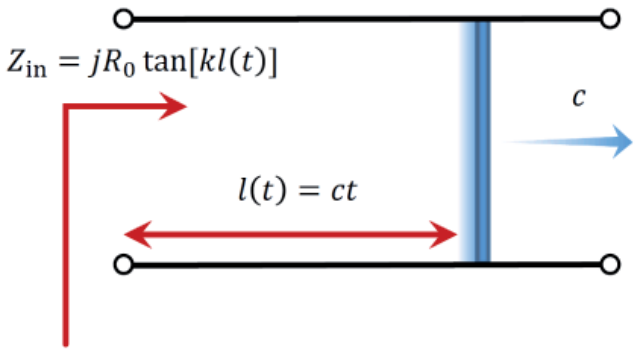

Figure 1b. A conceptual realization of the time-dependent inductance for Figure 1a by a short-circuited line the length of which extends with a constant velocity.

to release the stored energy in the form of an arbitrarily shaped pulse. In addition to that, in this paper we extend the theory towards arbitrary incident signals.

2. Accumulation of Energy by Time-Modulated Reactive Elements

2.1 Time-Harmonic Excitation

Let us consider a time-varying reactive element, for instance, an inductance. The voltage on such an inductance reads as

$$v_{\mathrm{L}}(t) = L(t)\frac{di(t)}{dt} + \frac{dL(t)}{dt} i_{\mathrm{L}}(t), \qquad (2)$$

where $v_{\mathrm{L}}(t)$ and $i_{\mathrm{L}}(t)$ denote the instantaneous voltage and current, respectively. For a conventional stationary inductor, the second term in Equation (2) is zero. However, for an inductance that changes in time, the voltage across it depends on the time derivative of $L(t)$. Moreover, the second term in Equation (2) resembles Ohm's law, which relates voltage with current through a coefficient $\frac{dL(t)}{dt}$, meaning that this derivative can be considered as a positive or negative resistance. In other words, a time-varying inductance either produces or absorbs energy. As soon as the inductor is lossless, this energy cannot be absorbed by the element itself: it can be either accumulated in the reactive element or in the modulating device (assuming that it is also lossless).

Let us study time-varying reactive elements for the example of a transmission line terminated by a time-modulated inductance, as illustrated in Figure 1a. In order to exploit virtual absorption in time-varying reactive elements, let us find the required modulation function that cancels reflection from the load. For convenience, the voltage on the inductance can be split into the incident voltage, $v^+(t)$, and the reflected voltage, $v^-(t)$. This allows us to express the voltage on the inductance and the current through it as

$$v_{\mathrm{L}}(t) = v^+(t) + v^-(t), \qquad (3)$$

$$i_{\mathrm{L}}(t) = \frac{v^+(t) - v^-(t)}{R_0},$$

where R_0 represents the characteristic impedance of the transmission line. Substituting Equation (2) into Equation (3), we get a general formula for the incident and reflected waves:

$$= L(t)\frac{dv^-(t)}{dt} + \left[\frac{dL(t)}{dt} + R_0\right] v^-(t) \qquad (4)$$

$$= L(t)\frac{dv^+(t)}{dt} + \left[\frac{dL(t)}{dt} - R_0\right] v^+(t).$$

Assuming a time-harmonic incident wave $v^+(t) = A\cos(\omega t)$ and demanding zero reflection, $v^-(t) = 0$, it is possible to solve Equation (4) and find the required function for $L(t)$ The solution is

$$L(t) = \frac{R_0}{\omega}\tan(\omega t). \qquad (5)$$

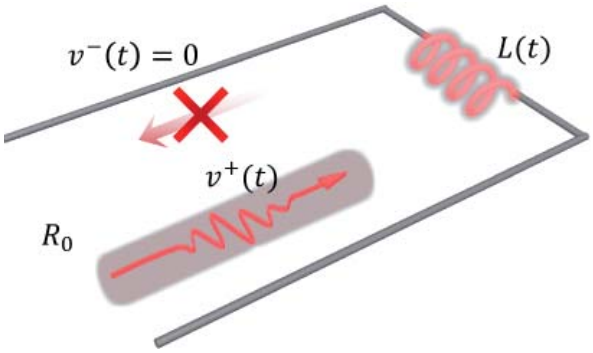

Figure 2a. A conceptual illustration of a time-varying inductance that absorbs the energy of any incident signal.

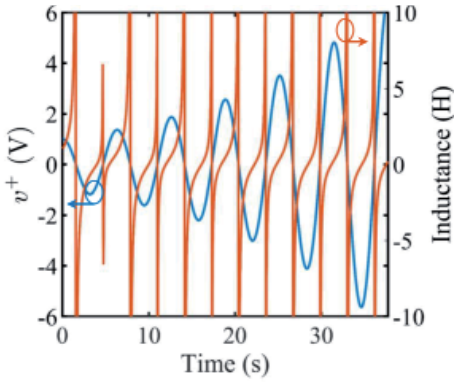

Figure 2b. An exponentially growing incident voltage and the modulation function that realizes zero reflection for the case of Figure 2a. The voltage of the incident signal is shown in blue, and the modulation function for inductance is shown in red.

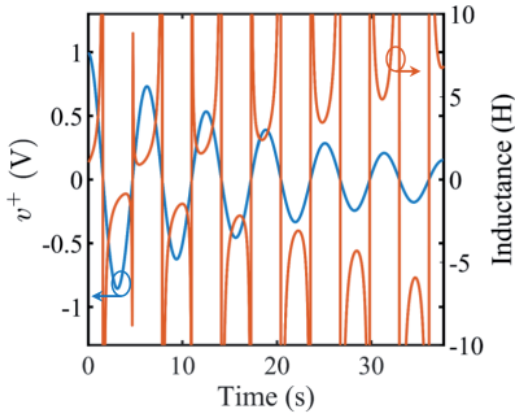

Figure 2c. An exponentially decaying incident voltage and the modulation function that realizes zero reflection for the case of Figure 2a. The voltage of the incident signal is shown in blue, and the modulation function for inductance is shown in red.

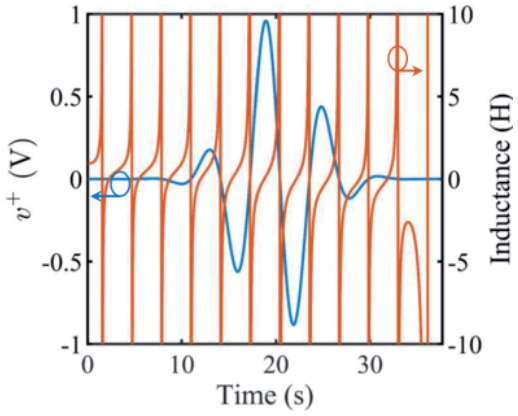

Figure 2d. A pulse signal and the corresponding modulation function. The voltage of the incident signal is shown in blue, and the modulation function for inductance is shown in red.

An inductance modulated according to Equation (5) eliminates the reflected wave, meaning that it virtually absorbs all the input energy. For better understanding, let us draw an analogy between a transmission line terminated with such a time-varying load and a short-circuited transmission line. The classical formula for the input reactance of a short-circuited transmission line is

$$Z_{\text{in}} = jR_0 \tan\left(\frac{\omega}{c} l\right), \qquad (6)$$

where c is the phase velocity and l represents the length of the line. Instead of a constant length l, let us now consider a short-circuited line the length of which is linearly increasing with constant velocity, c. The input impedance of such a line is $Z_{in} = jR_0 \tan(wt)$ (see Figure 1b), which is exactly equal to the impedance of the time-modulated inductance, $Z_{in} = j\omega L(t)$. It becomes clear that inductance modulated according to Equation (5) mimics a short-circuited transmission line of linearly increasing length. We see that in this conceptual scenario, the reason for having no reflection from a lossless load is that the incident wave never reaches the reflecting termination, since the short is moving away from the input port with the same velocity as the phase front of the incident wave. Varying the load inductance as prescribed by Equation (5) for a long enough time one can thus accumulate theoretically unlimited field energy in the reactive load.

2.2 Virtual Absorption of Arbitrary Incident Signal

The analysis presented above of transmission lines terminated with time-varying reactive elements is quite general, and it can be applied for accumulation of energy delivered not only by time-harmonic waves. Equation (4) can be reconsidered for an arbitrary incident wave $v^+(t)$

and solved again with respect to the modulation function $L(t)$, assuming zero reflection, $v^-(t) = 0$. The solution is

$$L(t) = R_0 \frac{v^+(0) + \int_0^t v^+(t')dt'}{v^+(t)}. \qquad (7)$$

In the case of a time-harmonic incident voltage, Equation (7) gives a tangent function that matches with Equation (5). Figure 2a shows that conceptually, an incident voltage of any shape can be virtually absorbed.

Figures 2b-2d illustrate examples of different modulation functions that realize zero-reflection regimes for various time dependences of the incident voltage. In all the figures, the incident voltage is shown in blue and the modulation function for inductance is shown in red. It is obvious that Equation (7) has a solution for any integrable function: therefore, for any incident voltage signal, a proper modulation function can be determined.

3. Controlling the Release of Energy

3.1 Engineering the Shape of the Output Pulse

Accumulation of energy with no loss is also possible by controlling the source [2]. However, such an approach does not provide any control of how the stored energy will be released. In our case, it is possible to stop modulation of the load and the energy will be slowly released, but it is possible to change the modulation regime and engineer the shape of the released pulse. One of the possibilities is to modulate the load as an exponentially decaying function of time. We assume that starting from $t = 0$, the time-varying inductance was illuminated by a time-harmonic wave, and the inductance was modulated according to Equation (5) until the moment $t_0 = 2.5$ s. During this period of time, incident energy was accumulated in the load. Starting from $t = t_0$, the incident wave was kept the same, but the load reactance was modulated as an exponentially decaying function:

$$L(t) = \begin{cases} \frac{R_0}{\omega}\tan(\omega t), & t < t_0 \\ \frac{R_0}{\omega}\tan(\omega t_0)\exp\left[-\alpha(t-t_0)\right], & t > t_0 \end{cases} \qquad (8)$$

where the parameter determines the inductance decay rate. Figure 3a graphically represents the varying inductance defined by Equation (8). The reflected voltage is presented in Figure 3b. It is clear that changing α allows us to shape the amplitude and width of the output pulse.

3.2 Forming a Delta-Function Pulse

We can envisage another way for releasing energy, getting back to the conceptual scenario with a moving short. The short that moves with the phase velocity c reflects nothing. Now let us consider a short that moves backwards after some moment of time, t_0. This means that the initially increasing length of the transmission line starts to reduce after moment t_0. In this case, at $t = 2t_0$, the length of the transmission line is zero and all the energy is released. However, most importantly, the energy is released in the form of a delta-function pulse, since all reflected waves propagate together with the short and arrive simultaneously at the output. In order to realize this, the modulation function should be mirrored with respect to moment t_0:

$$L(t) = \begin{cases} \frac{R_0}{\omega}\tan(\omega t), & t < t_0 \\ \frac{R_0}{\omega}\tan\left(2\omega t_0 - \omega t\right), & t > t_0 \end{cases} \qquad (9)$$

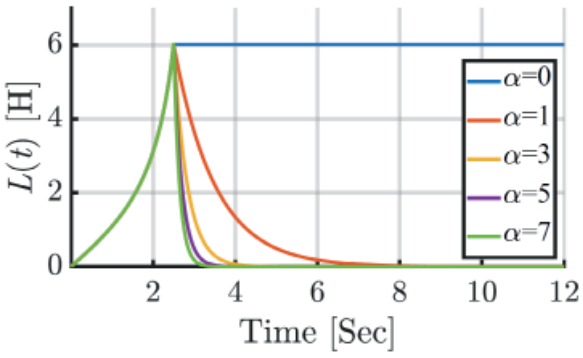

Figure 3a. Modulation functions of inductance for different sample values of α that control the shape of the output pulse.

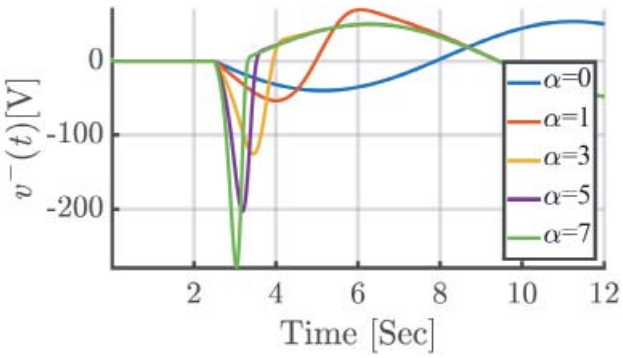

Figure 3b. The reflected voltage in the form of pulses.

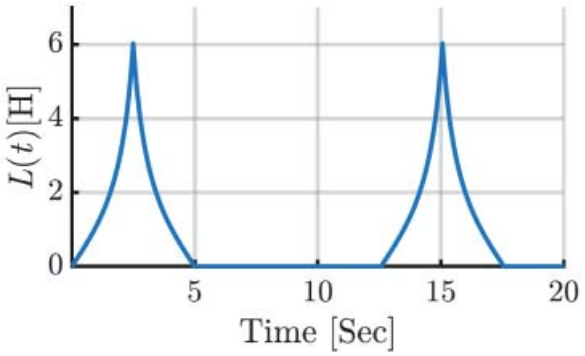

Figure 4a. The modulation function for an inductance that realizes pulse generation.

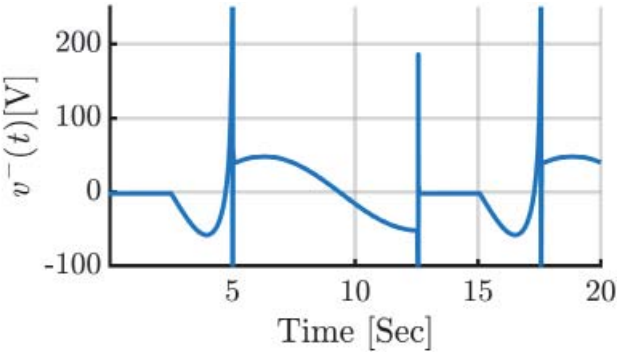

Figure 4b. The reflected voltage from a modulated load that exhibits formed short pulses at $2t_0$ (5 s) and $T_0 + 2t_0$ (17.6 s).

Figure 4a shows the time-dependent inductance that generates two output pulses. The function is periodic with a period equal to the period of the incident wave ($T_0 = 2\pi/\omega$) and consists of three regions: $0 < t < t_0$, when the energy is pumped into the system with zero reflection ($t_0 = 2.5$ s in this example); $t_0 < t < 2t_0$, when the time-modulation function is reversed in order to release all the energy by the moment $2t_0$; and $2t_0 < t < T_0$, when the system relaxes and $L(t)$ is constant and very small. The reflected voltage for such modulation is presented in Figure 4b, and we see that indeed at moment $2t_0$ there is a huge reflection. At moments $t = 0$ and $t = T_0$ there is a small reflection that occurs because of transitions; nevertheless, these reflections decay fast.

In analogy with a moving short, illustrated in Figure 1b, there is no need to physically move the short. Conceptually, it is possible to periodically load a transmission line with switches that can be closed at the appropriate moments in time [3]. In this scenario, the output pulse is formed by a set of periodic pulses that propagate along the line. Initially, all the switches are open, and the signal propagates without reflections. When the leading pulse arrives at the last switch, the switch closes, and the pulse is therefore reflected. This reflected pulse and the second incoming pulse approach the second-to-the-last switch from the opposite directions and at a moment in time when they meet, the second switch closes, thus forming a reflected pulse of doubled amplitude. It is clear that each next switch increases the amplitude of the reflected pulse, meaning that the energy at the output is proportional to the squared number of pulses entering the transmission. However, the total energy entering the transmission line is proportional to the number of pulses. This means that extra energy comes from the device that controls the switches.

From another perspective, in order to achieve zero reflection the requirement that has to be fulfilled is the impedance matching, meaning that a single time-varying element given by Equation (5) can be replaced by a combination of conventional elements that give the same impedance. In order to do this, one can expand the periodic function in Equation (5) into a Fourier series and then realize components of the series using harmonically pumped mixers and filters [3].

3.3 Energy-Keeping Regime

Modulating a reactive load makes it possible to cancel the reflection and virtually absorb the incident energy. It also allows us to engineer the shape of released pulses. Moreover, there is an additional functionality that is vital for energy-storing applications. By changing the modulation function, it is possible to realize the energy-keeping regime. In this case, Equation (4) can be solved assuming zero reflection at all moments of time, $v^-(t) = 0$ and, as an example, an exponentially decaying incident wave after some moment of time, t_0 :

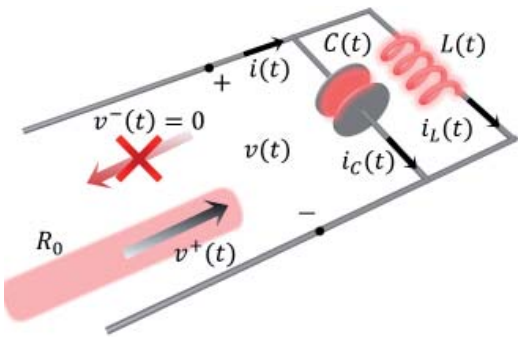

Figure 5a. A transmission line terminated by a parallel $L(t)C(t)$ circuit.

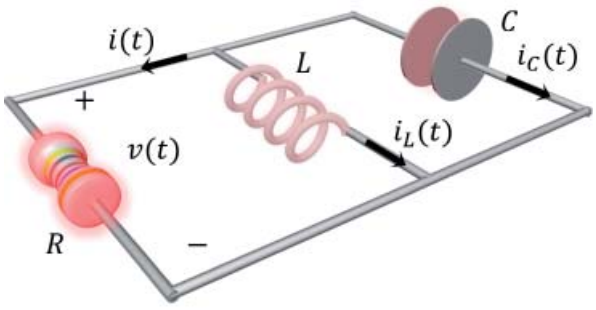

Figure 5b. The RLC circuit corresponding to Figure 5a after stopping modulation.

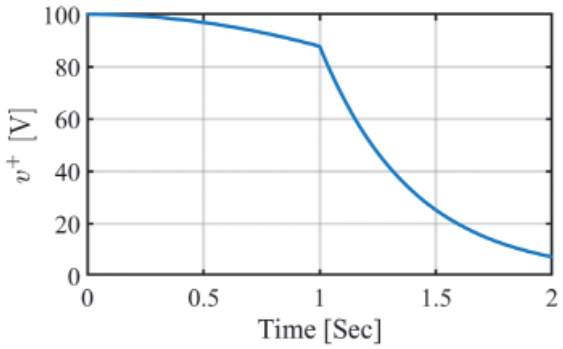

Figure 6a. The incident voltage that is a cosine function before $t_0 = 1$ s and an exponentially decaying function after t_0. The decaying rate was $\beta = 5$.

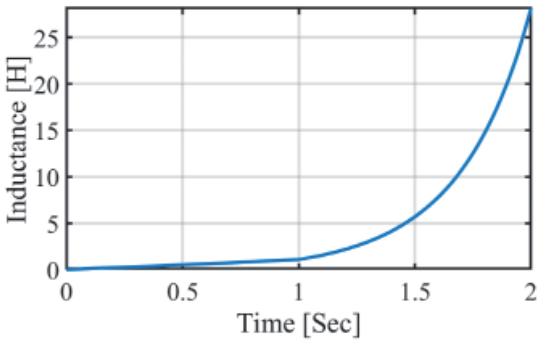

Figure 6b. The modulation function for an inductance that realizes zero reflection of the incident voltage wave in Figure 6a.

$$v^+(t) = \begin{cases} A\cos(\omega t), & t < t_0 \\ A\cos(\omega t_0)\exp\left[-\beta\omega(t-t_0)\right], & t > t_0 \end{cases} \quad (10)$$

The parameter β controls the rate with which the incident voltage attenuates to zero.

In order to realize zero reflection before moment t_0, the inductance has to be modulated as defined by Equation (5). In order to find the modulation function for the time period after t_0, Equation (4) has to be solved using the corresponding voltage $v^+(t)$ from Equation (10). The solution in this case is

$$L(t) = C\frac{\exp(\beta t\omega)}{\cos(t\omega)} + \frac{R_0\left[-\beta\cos(t\omega)+\sin(t\omega)\right]}{\cos(t\omega)\left(1+\beta^2\right)\omega}, \quad (11)$$

where C is a constant that is given by

$$C = \frac{\beta\exp(-\beta t_0\omega)R_0\left[\cos(t_0\omega)+\beta\sin(t_0\omega)\right]}{\left(1+\beta^2\right)\omega}. \quad (12)$$

The modulation function in Equation (11) grows exponentially; however, the growth rate depends mostly on β. The faster the incident voltage in turned off, the faster is the required growth of the modulation function. Figure 6a graphically shows the incident voltage that exponentially attenuates to 0 with the rate $\beta = 5$ after $t_0 = 1$ s. Figure 6b shows the corresponding modulation function for an inductance that keeps the reflected voltage always at a zero level.

In this case, the time-varying load keeps the energy as long as required and afterwards, the energy can be released. The pumping circuit spends energy on modulation during the energy-keeping period, but finally all the energy can be released as an output pulse [3].

4. Engineering Currents in the Branches of a Parallel LC Circuit

The solution for a single time-varying element that cancels the reflection leaves no freedom for electric current flowing through the element. It is defined by the characteristic impedance of the transmission line and the amplitude of the incident wave. However, replacing a single reactive element via a circuit composed of two elements (see Figure 5a) allows us to choose functions for currents flowing through the components. Modulating both of these elements allows us to engineer time dependences of the currents in the branches with one restriction on the sum of the currents, which should equal $i(t) = A\cos(\omega t)/R_0$ in order to ensure zero reflection. Currents in the branches uniquely define the corresponding functions for the reactive elements, which makes it possible to find simple and realizable modulation functions for reactive elements.

5. Conclusion

In conclusion, we have developed our results on time-variant reactive elements that can continuously accumulate energy from conventional external time-harmonic sources, without any reflections of the incident power, focusing on the regime of energy release. We have found the required time dependences of reactive elements, and discussed possible realizations as time-space modulated transmission lines and mixer circuits. We have shown that a modulated reactive load as an exponentially decaying inductance provides control over the shape of the released pulse. Moreover, we also discussed the possibility of realizing an energy-keeping regime in the absence of incident waves. Indeed, exploiting time-varying reactive loads offers a vast range of possibilities, which become possible if the modulation function is not limited to time-harmonic and even periodic functions. Although the study was made for probably the

simplest examples of time-varying inductance, the results can be directly applied to waves incident on lossless time-modulated boundaries, since they can be modeled as bulk loads in an equivalent transmission line.

6. References

1. G. A. Ptitcyn, M. S. Mirmoosa, V. S. Asadchy, and S. A. Tretyakov, "Time-Modulated Reactive Elements for Control of Electromagnetic Energy," 2019 URSI International Symposium on Electromagnetic Theory (EMTS), paper E08-1, San Diego, CA, USA, May 2019.

2. D. G. Baranov, A. Krasnok, and A. Alù, "Coherent Virtual Absorption Based on Complex Zero Excitation for Ideal Light Capturing," *Optica*, **4**, December 2017, p. 1457.

3. M. S. Mirmoosa, G. A. Ptitcyn, V. S. Asadchy, and S. A. Tretyakov, "Unlimited Accumulation of Electromagnetic Energy Using Time-Varying Reactive Elements," *Phys. Rev. Applied*, **11**, 2019, p. 014024.

Antenna Agnostic Feed Cancellation STAR System for Improved Cancellation

Satheesh Bojja Venkatakrishnan, Alexander Hovsepian, and John L. Volakis

Department of Electrical and
Computer Engineering
Florida International University
Miami, FL USA

Abstract

Due to increased consumer demand for higher data rates, additional but discontinuous frequency bands will be allocated for commercial use. As a result, only a small percentage of the RF spectrum will be assigned to US departments and agencies. This spectrum shrinkage has led to the development of creative techniques for efficient spectrum utilization. A well-known technique to better utilize existing bandwidth is that of "Same Frequency – Simultaneous Transmit and Receive" (SF-STAR). SF-STAR allows for concurrent transmission and reception of RF signals across the entire available bandwidth to double throughput. A major challenge in realizing STAR is the high power transmitted (Tx) signal coupling into the collocated receiver (Rx), resulting in direct interference. As a result, implementation of SF-STAR requires significant isolation of 90 dB to 120 dB between the transmitter and receiver. To achieve this, we must (1) cancel interference caused by the transmitter itself that is collocated with the receiving antenna; (2) remove multipath transmitted signals; (3) suppress spurious signals from nearby interferers; and (4) cancel noise from the transmitting chain via self-interference cancellation (SIC). In this paper, we present an interference-cancellation circuit that is antenna agnostic and achieves isolation up to 60 dB at the antenna stage across 400 MHz of instantaneous bandwidth. In addition, we present an SF-STAR cancellation that employs RF cancellation filters to provide ~70 dB cancellation across 1 GHz of instantaneous bandwidth.

1. Introduction

Increases in wireless connectivity and data traffic have been unprecedented. Moreover, available spectrum is across discontinuous frequency bands, with many applications being allocated in the same frequency band [1, 2]. In order to access multiple discontinuous frequency bands, wideband RF back ends capable of processing signals from different bands concurrently are required. Indeed, the need for effective use of bandwidth has led to creative approaches for spectrum allocation and reuse [3-10]. One such technique to enhance spectrum access is that of Same Frequency – Simultaneous Transmit and Receive (SF-STAR), also referred to as the in-band full duplexing (IBFD) technique. SF-STAR achieves full duplex communication by concurrent transmission and reception across the entire bandwidth of a channel at the same time to double data capacity.

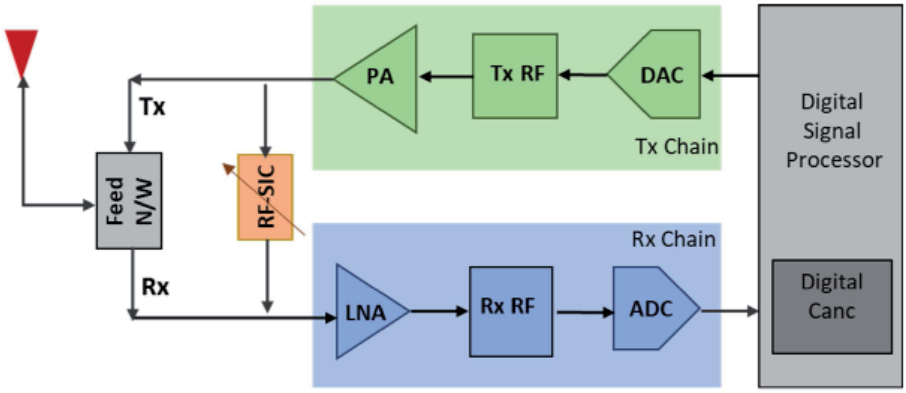

Figure 1a. The single-antenna radio architecture.

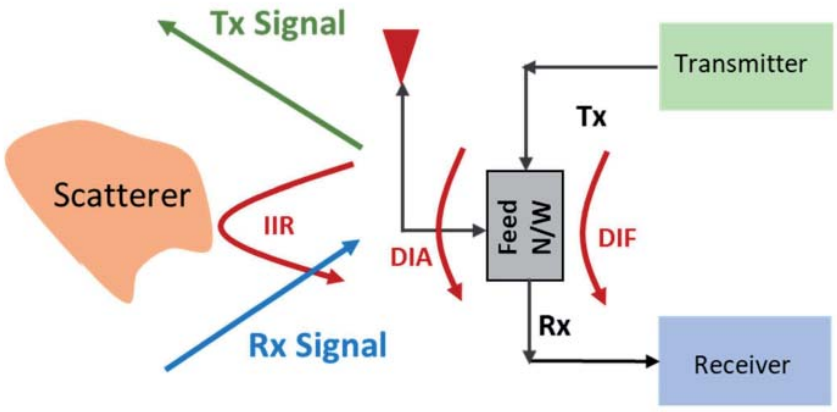

Figure 1b. The direct and indirect interference signal components.

A typical SF-STAR transceiver architecture is depicted in Figure 1a. A major challenge with STAR techniques is the coupling of a high-power transmitted (Tx) signal onto the collocated receiver (Rx). This signal interference may also lead to saturation and de-sensitization of the receiver chain. Specifically, it may lead to saturation of the low-noise amplifier (LNA) when high power signals are fed to it. Consequently, significant interference suppression of 100 dB to 120 dB is required for successful implementation of STAR. To do this, multiple stages of cancellation are required to (1) cancel direct interference (the original transmitted signal) from the transmitter; (2) suppress harmonics from power amplifiers (PA) generated in the transmitted chain; (3) remove multipath transmitted signals; (4) suppress spurious signals from nearby interferers; and (5) cancel noise from the transmitter chain via self-interference cancellation (SIC). Notably, self-interference cancellation must be carried out in the RF and baseband analog circuits as well as in the digital and propagation sections of the link.

Previous SF-STAR system architectures [3-14] demonstrated 80 dB to 110 dB interference suppression. However, this was done only for narrowband signals (< 80 MHz) using two or three cancellation stages. Recently, a novel wideband SF-STAR system was proposed [15] by our group, using phased arrays and collocated transmitting and receiving elements. The proposed SF-STAR system employs four stages of cancellation, with an unprecedented 120 dB of self-interference cancellation across a bandwidth of > 1 GHz. The cancellation includes all linear, nonlinear, and transmitted noise over the entire wide operational bandwidth. These cancellation stages were implemented at four stages: (1) the transmitting/receiving antenna, using polarization orthogonality; (2) the analog radio-frequency (RF) circuits of the receiver; (3) the analog baseband (BB) components; and (4) the digital cancellation sections [15-18].

Building on our previous SF-STAR realization, in this paper we present SF-STAR self-interference cancellation approaches that no longer depend on the antenna used. We focus on both single-antenna and multiple-antenna or array systems. For both cases, our SF-STAR cancellation implementation was able to achieve unprecedented cancellation levels of ~70 dB only in the RF domain across a wide bandwidth. The initial prototype showed > 70 dB of transmit-to-receive isolation with low-cost fabrication. Overall, the architecture is poised to achieve a total of > 100 dB receive-transmit isolation in a small form factor. The proposed solution realizes a more practical, frequency-tunable, full-duplex radio.

This paper is structured as follows. Section 2 describes the proposed SF-STAR implementation for a single-antenna radio. This section describes the novel feed network used to achieve improved isolation of > 60 dB. A two-antenna radio system is discussed in Section 3, showing interference cancellation of ~70 dB using two RF stages.

2. Case 1: Single-Antenna Radios

Typical radios employ single antennas to realize full-duplex communication. Full duplex is typically achieved either by employing time-division duplexing (TDD) or frequency-division duplexing (FDD). Figure 1a shows a typical single-antenna radio system. As can be seen, a single antenna is used for reception and transmission, and it is connected to a feed network that divides the receiver and transmitter circuits. Notably, both time-division duplexing and frequency-division duplexing require double the time and/or frequency resources in comparison with an SF-STAR system. Time-division duplexing radios employ circulators or isolators to suppress interference between the transmitter and receiver chains [19, 20]. On the other hand, frequency-division duplexing radios employ diplexers to achieve frequency filtering. Consequently, multi-band radios employing frequency-division duplexing require a larger number of tunable duplexers, resulting in complex RF architecture. Further, these single-antenna radios suffer from significant interference due to common modules (circulator/isolator/diplexer) connecting the transmitter and receiver chains. That is, to realize SF-STAR, high-power interference must be suppressed.

Figure 1b shows possible signal-interference paths in a radio that uses a single antenna. As seen, there are three paths for the transmitted signal to couple back to the receiver. These paths can be further divided into direct or indirect interference. Direct interference refers to signals that are coupled back to the receiver within the radio. There are two types of direct interference: (1) coupling within the circulators/isolators employed in the feed network due to their finite isolation, referred to as DIF; and (2) antenna mismatches causing the transmitted signal to be reflected back into the chain and to leak into the receiver, referred to as DIA. Of importance is the direct interference signals that are deterministic and can be analytically modeled for removal.

Indirect interference signals include those coming from outside the radio. For example, nearby scatterers can reflect a high-power signal back to the radio that subsequently leaks back into the receiver. These indirect interference signals from reflectors are referred to as IIR. IIR signals are unpredictable, and cannot therefore be accurately estimated a priori. In this paper, we primarily focus on removing direct interference signals.

To achieve SF-STAR cancellation at the antenna stage, for the first time we present a feed network that is agnostic to antenna type (see Figure 2). This novel approach has several benefits: (1) it can be inserted in existing radios, irrespective of antenna type; (2) it suppresses all signal components from the transmitter chain, including high-power direct transmitted signals, harmonics from power amplifiers, and noise coupling from the transmitter chain; and (3) it enables SWaP-C implementation due to its passive nature with no power consumption. Its small volume and passive circuitry makes its implementation suitable for future 5G communication, radars, and for remote-sensing applications.

The proposed antenna-agnostic feed network is depicted in Figure 2. As shown, the proposed feed network employs three circulators and a hybrid 180° coupler. It is assumed that all circulators are identical, and hence the signals through them undergo the same insertion loss and isolation. That is, their [*S*] parameters are assumed to be identical. For the circulators, a nominal 0.5 dB can be assumed, and for the hybrid-180° coupler, a typical insertion loss is 3 dB.

To describe the STAR cancellation process, a signal, T_1 is considered at the input of the feed network. This T_1 signal is fed into port 1 of the three-port circulator, C1. The outputs from port 2 ($T_1 S_{21}^{C1}$) and port 3 ($T_1 S_{31}^{C1}$) of C1 are then fed to C2 and C3, respectively. Circulator C2 is connected to the antenna. Hence the transmitted signal radiated by the antenna is $T_1 S_{21}^{C1} S_{21}^{C2}$. Due to finite isolation between the ports of C2, the transmitted signal at port 1 leaks into port 3, causing a signal $T_1 S_{21}^{C1} S_{31}^{C2}$ that must eventually be suppressed from the receiver chain. Unfortunately, this coupled signal is typically 20 dB below the original transmitted signal, implying large self-interference that must be suppressed to eventually decode the desired $R_1 S_{32}^{C2}$ signal.

To cancel this coupled $T_1 S_{21}^{C1} S_{31}^{C2}$ signal, we introduce an additional circulator, C3, that creates a replica of the same signal. As can be seen from Figure 2, the output of the transmitted signal from ports 3 of C2 and C3 are the same. Hence, by subtracting one from another, it is possible to completely remove the self-interference signal from the transmitter chain. To do so, a hybrid 180° coupler or a balun could be employed. Doing so creates a perfect cancellation as the two signals are of the same amplitude and but opposite phase. Because $S_{21}^{C1} = S_{21}^{C3}$ and $S_{31}^{C1} = S_{31}^{C2}$, the output of the hybrid 180° has no residual transmitted signal and contains only the desired received signal.

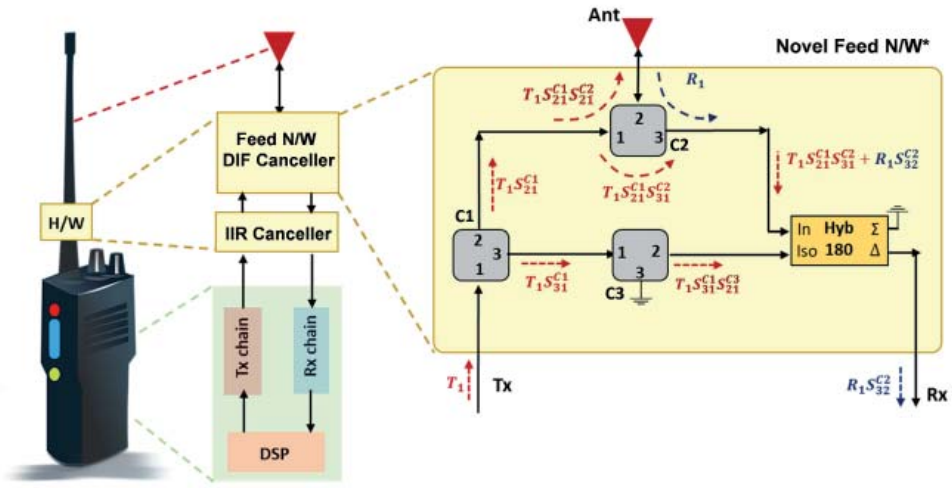

Figure 2. The proposed feed network providing up to 65 dB cancellation to achieve SF-STAR.

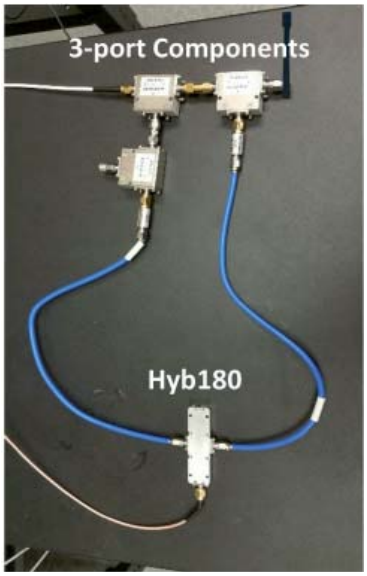

Figure 3a. A commercial off-the-shelf (COTS) implementation of the proposed high-isolation feed network.

The aforementioned new STAR transceiver was tested via simulations and measurements. Specifically, simulations were used to validate the proposed theory by achieving a cancellation of almost 100 dB. This is in contrast to past cancellations of 20 dB provided by a single circulator. For measurements, a simple feed network was realized using existing commercial-off-the-shelf (COTS) components,

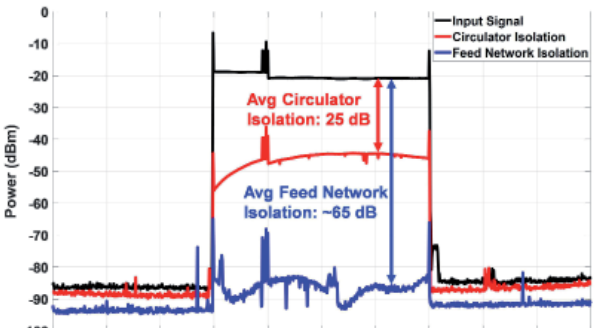

Figure 3b. The measured cancellation levels using the proposed feed network (blue) and a standard circulator (red).

as shown in Figure 3a. Figure 3b shows that the residual transmitted signal power was suppressed by almost 65 dB using the proposed feed network implementation. This corresponded to an average of 40 dB improvement over existing circulators, with the potential for 80 dB improvement using a specialized design.

3. Case 2: Dual-Antenna Radios

These radios employ two or more antennas for transmission and reception. As a result, they do not share a single feed network as in the former case (see Figure 4). This type of radio also suffers from both direct

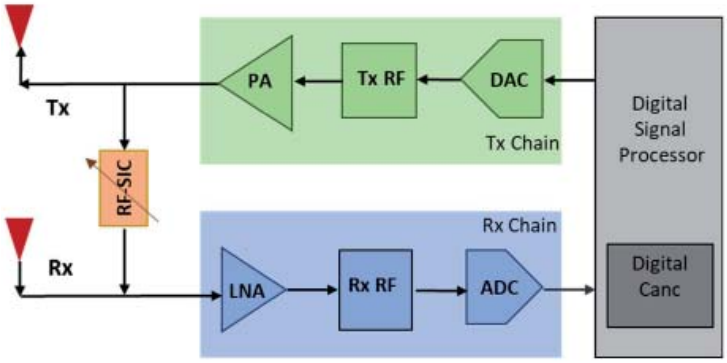

Figure 4a. A two-antenna radio system.

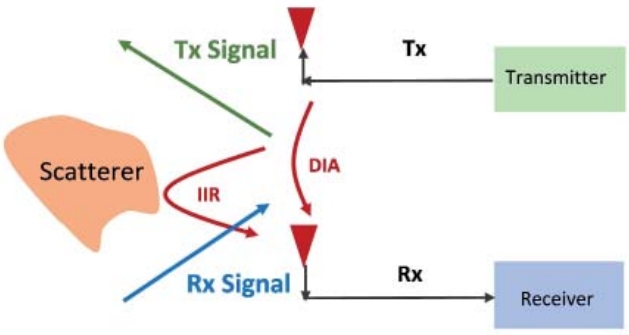

Figure 4b. Direct and indirect interference components in a two-antenna system.

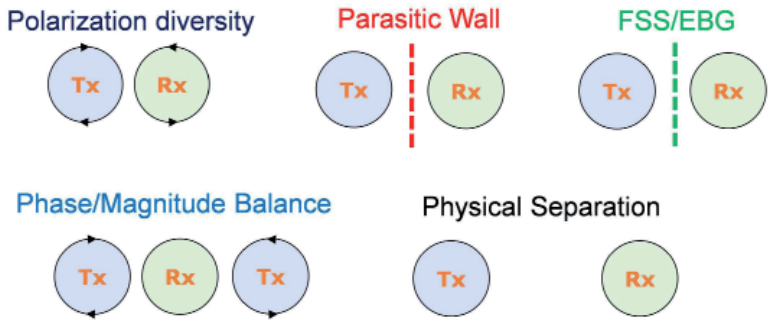

Figure 5. A few techniques for improving antenna isolation in a multi-antenna radio system.

and indirect interference, and there are multiple antenna-isolation approaches that can be employed to improve the cancellation. However, these approaches do not provide the required 60 dB cancellation. As a result, this type of radio is highly dependent on subsequent RF-SIC cancellation stages to augment the limited antenna isolation. Both stages combined should provide at least 60 dB of cancellation to successfully realize STAR.

3.1 Antenna Isolation

Figure 5 depicts several techniques for improving DIA isolation between two or more collocated antennas. These include: (1) polarization diversity, where both the transmitter and receiver are orthogonally polarized [18, 21]; (2) a parasitic wall or FSS or EBG between the transmitting and receiving antennas – this approach could provide improved isolation between two collocated antennas, but is narrowband [22]; (3) physically separating both antennas [5, 10], but the isolation depends on the antenna separation distance; (4) controlling phase and magnitude balance by creating 180° phase difference between the transmitter antennas [23] – however, this approach requires a total of three antennas as opposed to utilizing only two, as in previous cases. In this paper, we employed a hybrid technique employing phase/magnitude balance along with polarization diversity to achieve improved isolation.

The proposed SF-STAR radio contained a collocated pair of transmitting and receiving antennas. As shown in Figure 6a, the transmitting antenna is a flared monopole and the receiving aperture is a ring antenna. The ring is separated into two halves, each fed with a balun. This ring width is increased to widen the bandwidth to nearly 1.5 GHz backed by a 1λ diameter circular ground plane, placed a distance of $\lambda/5$ from the ring antenna at the lowest frequency of operation (see Figure 6a). The monopole is fed by a 50 Ω SMA connector, and a tapered microstrip balun feed is used for each of the ring halves (see Figure 6b). High transmitter/receiver isolation is achieved across a wide bandwidth due to the low cross-polarization of the transmitter and receiver antenna orientations. The VSWR for the transmitted polarization was < 2 across the entire bandwidth, and the $\text{VSWR} < 3$ at the receiving antenna, as depicted in Figure 7a. The entire design was fabricated using PCB technology to ensure low cost. However, despite the antenna's very good symmetry, the antenna was able to provide only 40 dB isolation across the desired bandwidth. To achieve 65 dB isolation, we could include an RF-SIC filter in the next stage of the receiver.

3.2 RF Cancellation

To achieve an additional 20 dB to 25 dB self-interference cancellation across a 1 GHz bandwidth, we

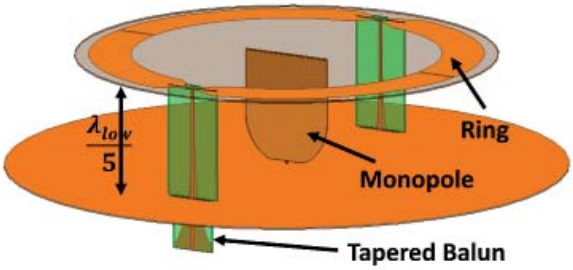

Figure 6a. The *HFSS* model of the high-isolation antenna.

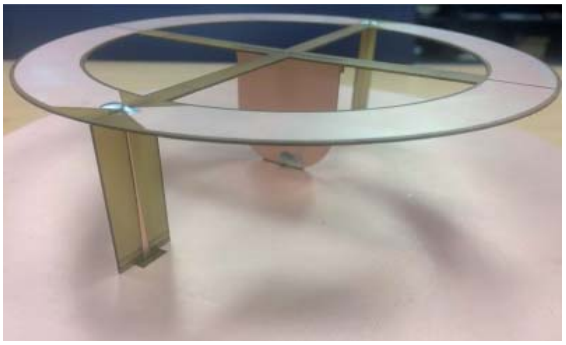

Figure 6b. The fabricated high-isolation antenna.

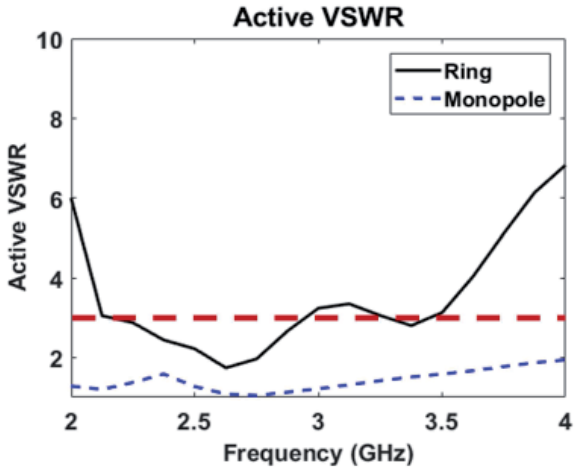

Figure 7a. The simulated VSWRs of the monopole and the ring antenna.

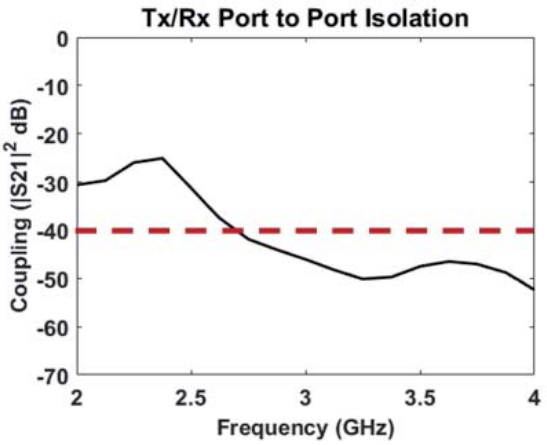

Figure 7b. The simulated isolations between the monopole and ring antenna.

employed a multi-tap FIR filter. Various filters have been used to suppress transmitter-receiver coupling. However, most of these implementations have been across narrow instantaneous bandwidths [3, 11]. In [15], we implemented a 12-tap filter bank RF-FIR filter that could achieve an average cancellation of ~25 dB across a 1 GHz instantaneous bandwidth. Increasing the number of taps in a filter provides more degrees of freedom (such as tunable tap delay and attenuation at each taps) to achieve cancellation over a much larger bandwidth. Concurrently, it is important to minimize these taps to ensure simplicity and reduce noise. In any case, the goal was to design a filter the response of which canceled the coupling from the transmitter to the receiver antenna represented by the transfer function $H_{chnl}(j\omega)$. The transfer function of the RF filter can be represented by the expression

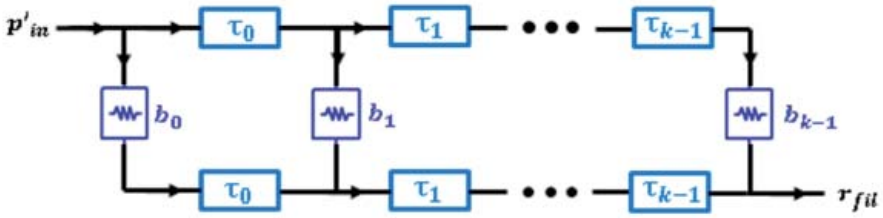

Figure 8. A block-diagram representation of the RF-SIC filter.

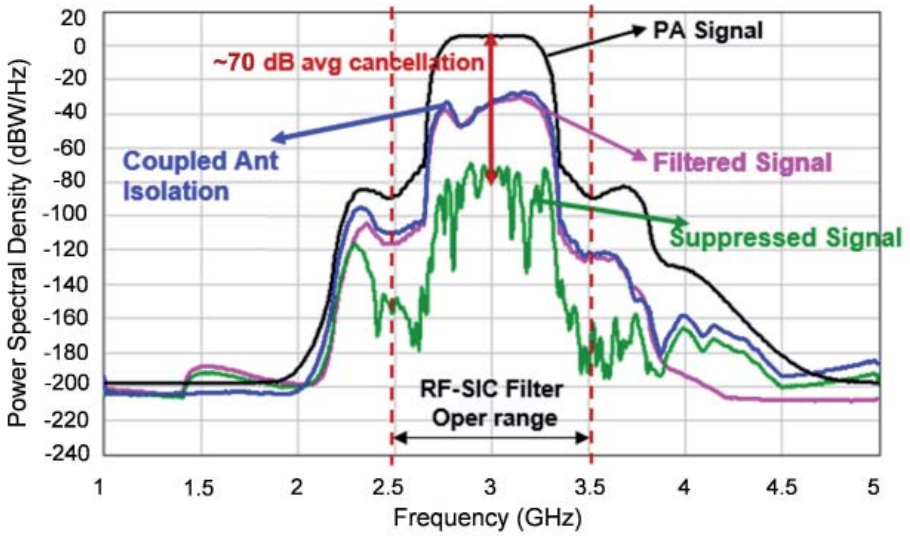

Figure 9. A simulation demonstrating a combined antenna + filter cancellation of ~70 dB across 1 GHz.

$$H_{fil}(j\omega) = \sum_{k=0}^{K-1} b_k e^{-j\omega\tau_k}, \quad (1)$$

where b_k refers to the tap coefficient values and the τ_k are the tap delays, represented in the block diagram in Figure 8. The goal is to minimize the number of taps and still represent the response of the antenna coupling given by $H_{chnl}(j\omega)$.

To design the RF-SIC filter, the coefficients of the transfer function in Equation (1) must be optimized to match the coupled signal from the transmitter onto the receiver. This optimization must be done across large bandwidths, a major challenge for the filter design. In the following, we refer to the RF-SIC filter response as $H_{fil}(j\omega)$ The goal is to have $H_{fil}(j\omega) = -H_{chnl}(j\omega)$ across the entire bandwidth. Any deviation will result in an imperfect cancellation. In dB, the level of self-interference cancellation is given by

$$SIC_{RF|dB} = 20\log_{10}\frac{H_{fil}(j\omega) + H_{chnl}(j\omega)}{H_{chnl}(j\omega)}. \quad (2)$$

Figure 9 gives the combined cancellation achieved using a two-antenna STAR system. As can be seen, the total cancellation now reached ~70 dB across 1 GHz of bandwidth. Only the antenna isolation and RF-SIC filter stages were used to achieve this. The blue plot corresponds to the self-interference suppression due to antenna isolation alone, and the green plot corresponds to the combined antenna and filter cancellation. Indeed, the results in Figure 9 validated the proposed approach of improved cancellation by employing SF-STAR in a two-antenna radio system.

4. Conclusion

A novel feed network to achieve SF-STAR cancellation was proposed. Key to this in-band full-duplex operation was the use of an antenna-agnostic cancellation approach. For the first time, the proposed system was capable of providing up to 60 dB cancellation just at the antenna stage. Additional cancellation filter stages can be added to easily achieve cancellations of ~100 dB or more across a 1 GHz bandwidth. The proposed feed network can be realized in a small form factor for ease of integration in existing radios. We also proposed a similar SF-STAR system for suppressing self-interference signals in a two-antenna radio. This approach employed high-isolation antennas and improved cancellation RF-SIC filters. Simulation confirmed a combined cancellation of up to 70 dB across 1 GHz. This same RF-SIC filter can be used in the single-antenna radio to achieve more than ~90 dB wideband cancellation by using only two stages of cancellation. In summary, we showed that an SF-STAR system can be realized using either single-antenna or two-antenna radios.

5. Acknowledgement

This work was supported by the US Office of Naval Research under grant N00014-16-1-2253 and under US Army contract #W911QX18P0203 with MaXentric.

6. References

1. S. Hong, J. Brand, J. I. Choi, M. Jain, J. Mehlman, S. Katti, and P. Levis, "Applications of self-interference cancellation in 5G and beyond," *IEEE Communications Magazine*, **52**, 2, February 2014, pp. 114-121.

2. L. Larson, "RF and microwave hardware challenges for future radio spectrum access," *Proceedings of the IEEE*, **102**, 3, March 2014, pp. 321-333.

3. K. E. Kolodziej, J. G. McMichael, and B. T. Perry, "Multitap RF canceller for in-band full-duplex wireless communications," *IEEE Transactions on Wireless Communications*, **15**, 6, June 2016, pp. 4321-4334.

4. J. Zhou, T. H. Chuang, T. Dinc, and H. Krishnaswamy, "Integrated wideband self-interference cancellation in the RF domain for FDD and full duplex wireless," *IEEE Journal of Solid-State Circuits*, **50**, 12, December 2015, pp. 3015-3031.

5. M. Duarte and A. Sabharwal, "Full-duplex wireless communications using off-the-shelf radios: Feasibility and first results," 2010 Conference Record of the Forty Fourth Asilomar Conference on Signals, Systems and Computers, November 2010, pp. 1558-1562.

6. D. Bharadia and S. Katti, "Full duplex MIMO radios," Proceedings of the 11th USENIX Conference on Networked Systems Design and Implementation, 2014, pp. 359-372.

7. D. J. van den Broek, E. A. M. Klumperink, and B. Nauta, "A self-interference-canceling receiver for in-band full-duplex wireless with low distortion under cancellation of strong Tx leakage," 2015 IEEE International Solid-State Circuits Conference - (ISSCC) Digest of Technical Papers, February 2015, pp. 1-3.

8. S. Chen, M. A. Beach, and J. P. McGeehan, "Division-free duplex for wireless applications," *Electronics Letters*, **34**, 2, January 1998, pp. 147-148.

9. D. Bharadia, E. McMilin, and S. Katti, "Full duplex radios," Proceedings of the 2013 Conference on SIGCOMM ACM, New York, NY, USA, pp. 375-386.

10. M. Duarte, C. Dick, and A. Sabharwal, "Experiment-driven characterization of full-duplex wireless systems," *IEEE Transactions on Wireless Communications*, **11**, 12, December 2012, pp. 4296-4307.

11. J. I. Choi, M. Jain, K. Srinivasan, P. Levis, and S. Katti, "Achieving single channel, full duplex wireless communication," Proceedings of the 16th Annual International Conference on Mobile Computing and Networking, 2010, pp. 1-12.

12. M. Jain, J. L. Choi, T. M. Kim, D. Bharadia, S. Seth, K. Srinivasan, P. Levis, S. Katti, and P. Sinha, "Practical, real-time, full duplex wireless," Proceedings of the 17th Annual International Conference on Mobile Computing and Networking, 2011, pp. 301-312.

13. E. Everett, A. Sahai, and A. Sabharwal, "Passive self-interference suppression for full-duplex infrastructure nodes," *IEEE Transactions on Wireless Communications*, **13**, 2, February 2014, pp. 680-694.

14. B. Debaillie, D. J. van den Broek, C. Lav´ın, B. van Liempd, E. A. M. Klumperink, C. Palacios, J. Craninckx, B. Nauta, and A. P¨arssinen, "Analog/RF solutions enabling compact full-duplex radios," *IEEE Journal on Selected Areas in Communications*, **32**, 9, September 2014, pp. 1662-1673.

15. S. Bojja Venkatakrishnan, E. A. Alwan and J. L. Volakis, "Wideband RF Self-Interference Cancellation Circuit for Phased Array Simultaneous Transmit and Receive Systems," *IEEE Access*, **6**, 2018, pp. 3425-3432.

16. K. L. Scherer, S. J. Watt, E. A. Alwan, A. A. Akhiyat, B. Dupaix, W. Khalil, and J. L. Volakis, "Simultaneous transmit and receive system architecture with four stages of cancellation," 2015 IEEE International Symposium on Antennas and Propagation USNC/URSI National Radio Science Meeting, July 2015, pp. 520-521.

17. S. Bojja-Venkatakrishnan, E. A. Alwan, and J. L. Volakis, "Wideband RF and analog self-interference cancellation filter for simultaneous transmit and receive system," 2017 IEEE International Symposium on Antennas and Propagation USNC/URSI National Radio Science Meeting, July 2017, pp. 933-934.

18. A. Hovsepian, S. B. Venkatakrishnan, E. A. Alwan and J. L. Volakis, "Wideband, scanning array for simultaneous transmit and receive," 2018 International Applied Computational Electromagnetics Society Symposium (ACES), Denver, CO, 2018, pp. 1-2.

19. H. Holma, S. Heikkinen, O. A. Lehtinen, and A. Toskala, "Interference considerations for the time division duplex mode of the UMTS terrestrial radio access," *IEEE Journal on Selected Areas in Communications*, **18**, 8, August 2000, pp. 1386-1393.

20. H. Haas and G. J. R. Povey, "The effect of adjacent channel interference on capacity in a hybrid TDMA/CDMA-TDD system using UTRA-TDD parameters," Vehicular Technology Conference, 1999, VTC 1999 - Fall, IEEE VTS 50th, **2**, 1999, pp. 1086-1090.

21. E. A. Etellisi, M. A. Elmansouri, and D. S. Filipovi´c, "Broadband Full-Duplex Monostatic Circular-Antenna Arrays: Circular Arrays Reaching Simultaneous Transmit and Receive Operation," *IEEE Antennas and Propagation Magazine*, **60**, 5, October 2018, pp. 62-77.

22. X. Yang, Y. Liu, Y. Xu and S. Gong, "Isolation Enhancement in Patch Antenna Array with Fractal UC-EBG Structure and Cross Slot," *IEEE Antennas and Wireless Propagation Letters*, **16**, 2017, pp. 2175-2178.

23. H. Saeidi-Manesh and G. Zhang, "High-Isolation, Low Cross-Polarization, Dual- Polarization, Hybrid Feed Microstrip Patch Array Antenna for MPAR Application," *IEEE Transactions on Antennas and Propagation*, **66**, 5, May 2018, pp. 2326-2332.

Dual-Focal Metalenses Based on Complete Decoupling of Amplitude, Phase, and Polarization

He-Xiu Xu[1,2], Menghua Jiang[2], Guangwei Hu[2], Lei Han[2], Ying Li[2], and Cheng-Wei Qiu[2]

[1]Air Force Engineering University
Xi'an, 710051, China
E-mail: hxxuellen@gmail.com

[2]Department of Electrical and Computer Engineering
National University of Singapore
Singapore 117583, Singapore

Abstract

The simultaneous control of amplitude and phase via metasurfaces affords us an unprecedented degree of freedom in manipulating electromagnetic waves. However, currently most designs suffer from low efficiency, which raises certain concerns for real-world applications. Moreover, complete amplitude, phase, and polarization modulation is particularly challenging. This typically requires a combination of attenuators, optically thick wave plates, and large dielectric lenses. Here, we propose an alternative scheme by introducing vertical-mode cross-coupling for polarization control and high efficiency, while involving spatially-varied orientations and structures for independent amplitude and phase modulation. The vertical-mode cross-coupling is synthesized by stacking triple-layer twisted split-ring resonators (SRRs) operated in a transmissive scheme. Such tight cross-coupling and chirality-assisted coherent multiple resonances facilitate high cross-polarization conversion efficiency (~100%) and a broadband transmission window with full phase coverage. As a proof of concept, two dual-focal metalenses that are challenging to be actualized through conventional metasurfaces were designed and studied numerically and experimentally, with a total thickness of $\lambda_0/12$ at microwave frequencies. Desirable dual-focusing behavior with axial and lateral alignment of two foci were demonstrated. Our findings, not confined to microwave operation, open up an alternative way to the fine control of light, and can stimulate novel and high-performance versatile photonic metadevices.

1. Introduction

The explosive field of metasurfaces has afforded extraordinary capabilities for manipulating electromagnetic (EM) waves [1-7]. Metasurfaces, composed of a mass of sub-wavelength-spaced meta-atoms, has generated huge interest from both the physics and engineering communities, due to their exotic behavior and promising applications. The local amplitude, phase, and polarization are three types of important information for the control of the output EM wavefront. In general, previous pursuits of metasurfaces can be divided into these three categories. However, the simultaneous modulation of the above three items has rarely been reported. In recent years, we have witnessed some progress toward simultaneous amplitude and phase control [8-10]. However, most attempts were either in reflection geometry or with low conversion efficiency, the maximum of which was fundamentally restricted to 25%, which may seriously hinder real-world applications. Moreover, all these designs left the polarization control totally irrelevant or essentially unaddressed. On the other hand, much attention has been paid to high-efficiency operation, which is critically important for high-performance photonic devices [11]. However, all these designs were confined to phase- or polarization-only modulation, making kaleidoscopic wavefront control particularly challenging.

Here, we propose a scheme [12] that is capable of *complete* amplitude, phase, and polarization modulation with high efficiency in transmission geometry, opening up fascinating opportunities to go beyond what is achievable by available metasurfaces. By introducing a set of vertical coupling modes, near 100% efficiency is actualized by a *total* cross-polarization conversion between the incident and transmitted beam. Most importantly, the transmission amplitude can be continuously tuned by altering the orientation angle without changing the local phase response. Such exotic merit allows decoupling of the fixed relationship between the phases and magnitudes, which can be engineered for kaleidoscopic wavefront shaping.

2. Principle and Properties of the Anisotropic Meta-Atom

For full-space EM wave manipulation by a thin metasurface (the left panel of Figure 1a), four parameters – r_{uu}, r_{vu}, t_{uu}, and t_{vu}, with u and v denoting the two principle axes – are typically involved to completely describe the metasurface's reflection and transmission properties. Because of symmetry requirements, half of the coupled energy is radiated back, leading to a fundamentally limited cross-polarized efficiency below 25% for single-layer metasurfaces. Although inclusion of effective magnetic responses to the meta-atom assists high co-polarized transmissions [11], it is inefficient for polarization modulation due to the coherent electric and magnetic response. Completely different from previous methods, we here propose a scheme by introducing vertical interlayer mode cross-coupling and coherent multiple resonances. Full cross-polarization conversion can be engineered with the three residual components completely suppressed, facilitating a near 100% transmission rate, as shown in the right panel of Figure 1a.

To realize complete cross-polarization conversion, the planar meta-atom should exhibit strong local chirality, without any mirror or rotational symmetry or the three-dimensional chiral architectures [13]. Such structural chirality yields strong cross-coupling between electric and magnetic fields that occurs at resonances. Having these aspects in mind, the basic building block for complete decoupling of amplitude, phase, and polarization was designed and is shown in Figure 1b. The transmissive meta-atom consists of triple-twisted split ring resonators (SRRs) sandwiched by two dielectric spacer layers with a dielectric constant (ε_r) of 4.5 and a thickness (h) of 1.5 mm. Each pair of neighboring SRR metallic patterns has a mutual twist angle of $\Phi = 45°$. Such a judicious choice as discussed in the following offers resonance hybridization and interlayer coupling, which are the keys for polarization transformation. By shining the composite meta-atom from the bottom with a y-polarized plane wave, triple resonant modes can be coherently excited, accounting for the three resonant peaks with almost 100% efficiency and dips manifested across the $|t_{yy}|$ or $|t_{xx}|$ (Figure 1c) spectrum. These coherently excited resonant modes, identified from the field/current distributions shown in the inset of Figure 1c, in order

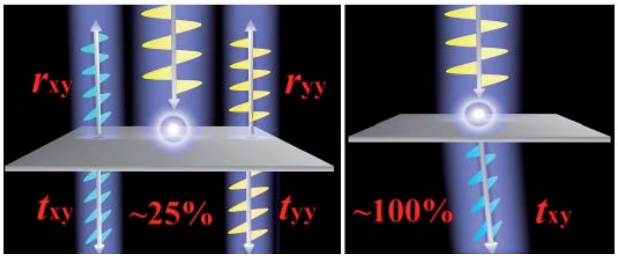

Figure 1a. A conceptual illustration to overcome the low efficiency in previous single-layer metasurfaces and a characterization of the proposed transmissive triple-layer meta-atom with 90° polarization conversion: a schematic diagram.

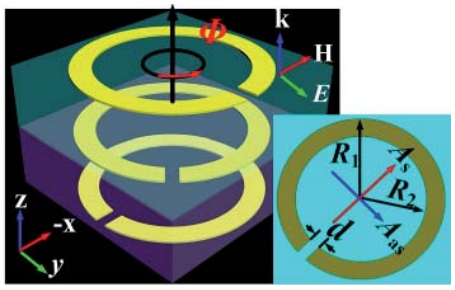

Figure 1b. The topology and a parametric illustration for the case of Figure 1a.

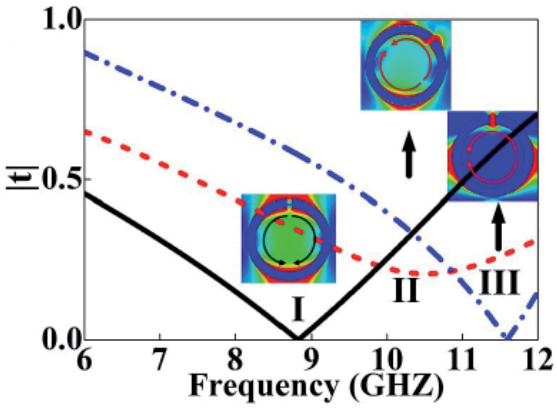

Figure 1c. The FDTD simulated co-polarization transmission spectrum and field/current distributions of three individual SRR_1, SRR_2, and SRR_3 cases to identify three fundamental resonant modes.

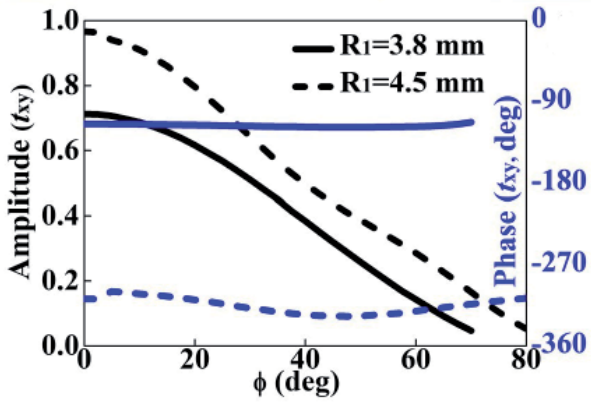

Figure 1d. The FDTD-calculated transmission amplitude and phase responses of t_{xy} as a function of the orientation angle, Φ. The results of both meta-atoms with $R_1 = 4.5$ mm and $R_1 = 3.8$ mm are given.

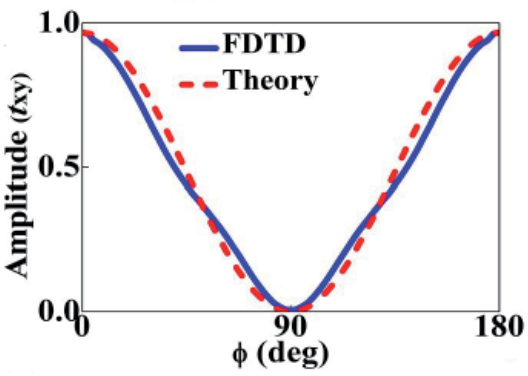

Figure 1e. The theoretically calculated transmission amplitude and phase responses of t_{xy} as a function of the orientation angle, Φ. Only the meta-atom with $R_1 = 4.5$ mm was selected for verification.

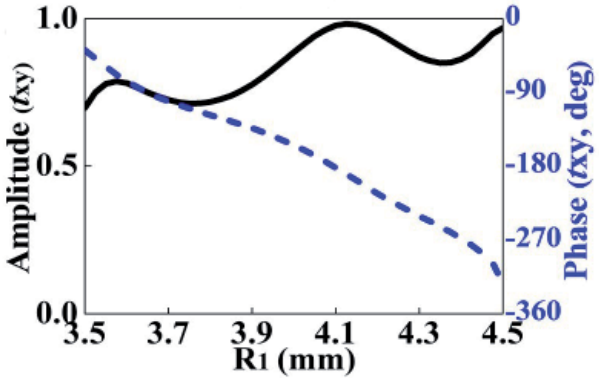

Figure 1f. The FDTD-calculated transmission amplitude and phase as a function of R_1 at 9.45 GHz.

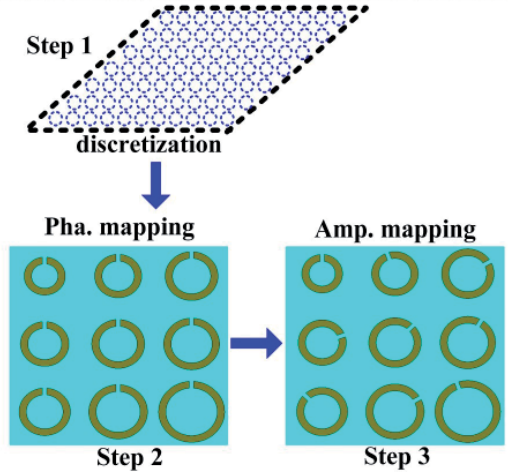

Figure 1g. An illustration of the three-step design process. In all cases, the meta-atoms had $d = 0.6$ and a square lattice constant of 10 mm × 10 mm.

correspond to the symmetric dipolar-resonant (I), hybrid (II), and asymmetric (III) LC-resonant modes of three SRRs with $\Phi = 0°$ (SRR_1), $\Phi = 45°$ (SRR_2), and $\Phi = 90°$ (SRR_3), respectively from low to high frequencies.

The cascading and superposition of these multiple resonant modes facilitates the broadband cross-polarization transmission window, and also increases the discontinuous phase coverage without affecting the constant transmission amplitude. By coherently varying the radii (R_1 and R_2) of the above triple SRRs, the desirable full phase coverage of t_{xy} can be engineered. Here, the width of the SRRs, $w = 1$ mm, is kept constant for a simple design. Most importantly, continuous amplitude variation is actualized from zero to unity by tuning the orientation angle, Φ, of the SRRs without altering the phase response in the transmission window. The merit of this – which may fin critical applications in the synthesis of complex wave fields, novel beam shaping, and high-quality holographic images – was further proven from the results shown in Figure 1d, where the transmission spectrum is plotted as a function of Φ and a maximum phase change of 22° was demonstrated. Such a Φ-immune phase response brings extreme flexibility in reshaping the wavefront through individually altering the orientation angles and structure parameters. We obtained the $\varphi - R_1$ relationship based on full-wave FDTD simulations, since the transmission phase of t_{xy} as a function of R_1 was fully numerical. Intriguingly, we found that the transmission amplitude of t_{xy} could be derived analytically as a function of Φ (see the following). Such theoretical prediction avoids much time-consuming parametric analyses in metadevice design.

The analytical derivation starts with the symmetric and anti-symmetric mode analysis of a single-layer SRR with an open split directed toward Φ relative to the x axis. For a normally incident x-polarized plane wave, symmetric ($E_s^{out} = E_x^{in} \cos\Phi A_s e^{i\varphi_s}$) and anti-symmetric ($E_{as}^{out} = E_x^{in} \sin\Phi A_s e^{i\varphi_{as}}$) modes are simultaneously excited, and are decoupled into x- and y-polarized components as

$$E_x^{out} = E_x^{in}\left(A_s e^{i\varphi_s}\cos^2\Phi + A_{as}e^{i\varphi_{as}}\sin^2\Phi\right), \quad (1)$$

$$E_y^{out} = \frac{1}{2}E_x^{in}\sin 2\Phi\left(A_s e^{i\varphi_s} - A_{as}e^{i\varphi_{as}}\right). \quad (2)$$

Similarly, the output x- and y-polarized components under a normally incident y-polarized plane wave can be expressed as

$$E_x^{out} = \frac{1}{2}E_y^{in}\sin 2\Phi\left(A_s e^{i\varphi_s} - A_{as}e^{i\varphi_{as}}\right), \quad (3)$$

$$E_y^{out} = E_y^{in}\left(A_s e^{i\varphi_s}\sin^2\Phi + A_{as}e^{i\varphi_{as}}\cos^2\Phi\right). \quad (4)$$

By taking Φ as $\Phi = 0°$, $\Phi = 45°$, and $\Phi = 90°$ we immediately obtain the output components for the three individual single-layer SRRs. The output components for the whole bottom-to-top SRRs can then be derived by cascading these transmission matrixes and taking the outputs of the former SRRs as new inputs of the latter SRRs. After a complicated derivation, we eventually obtain the output *x*- and *y*-polarized components of the triple-layer meta-atom under *x* polarization as

$$E_y^{out} = \frac{1}{8} E_x^{in} A\left[\cos 2\Phi\left(A^2 + B^2\right) + 2AB\right], \quad (5)$$

$$E_x^{out} = \frac{1}{8} E_x^{in}\left[-\left(AB^2 + A^3\right)\sin 2\Phi + B^3 - A^2 B\right]. \quad (6)$$

Here, $\alpha = A_s e^{i\varphi_s}$, $\beta = A_{as} e^{i\varphi_{as}}$, $A = \alpha - \beta$ and $B = \alpha + \beta$. Based on the same procedure, the *x* and *y*-polarized outputs under *y*-polarized excitation are formulized as

$$E_y^{out} =$$

$$\frac{1}{8} E_y^{in}\left[\left(B^2 - A^2\right)B - \left(B^2 A - A^3\right)\sin 2\Phi - 2A^3 \sin^3 2\Phi\right] (7)$$

$$E_x^{out} =$$

$$\frac{1}{8} E_y^{in} A\left[-2AB - 2A^2 \cos^3 2\Phi + \left(3A^2 + B^2\right)\cos 2\Phi\right] \quad (8)$$

For verification, we theoretically calculated the output components of the triple-layer meta-atom with $R_1 = 4.5$ mm and compared them with the full-wave FDTD simulation results in Figure 1e. Satisfactory agreement and accuracy of the analytical results was observed, which offers a quick way to relate rotation angles of the meta-atom to specific transmission amplitudes.

With the above results and features of our meta-atom, the design of the metasurface with arbitrary amplitude and phase distribution for prescribed functionality is simple. This typically involves three steps, as shown in Figure 1g. First, the required two-dimensional amplitude and phase profiles across the aperture at the operating frequency f_0 are determined. Second, the metasurface layout is mapped out by determining R_1 for each meta-atom according to the target phase profile and $\varphi - R_1$ relation shown in Figure 1f. Third, the design is finalized by spatially rotating each meta-atom with Φ by following the destined amplitude profile and analytical $t - \Phi$ relation. Our strategy with full Φ-dependent amplitude modulation, even in a cascaded profile, is still very thin, with a thickness of only $\lambda_0/12$, which is very suitable for integrated flat photonic devices.

Figure 2a. The design, theoretical, and numerical characterization of the first bifocal metalens with lateral alignment of two foci: a top view of half the metalens layout with a total of $M \times N = 16 \times 1$ pixels distributed along the *x* and *y* axes.

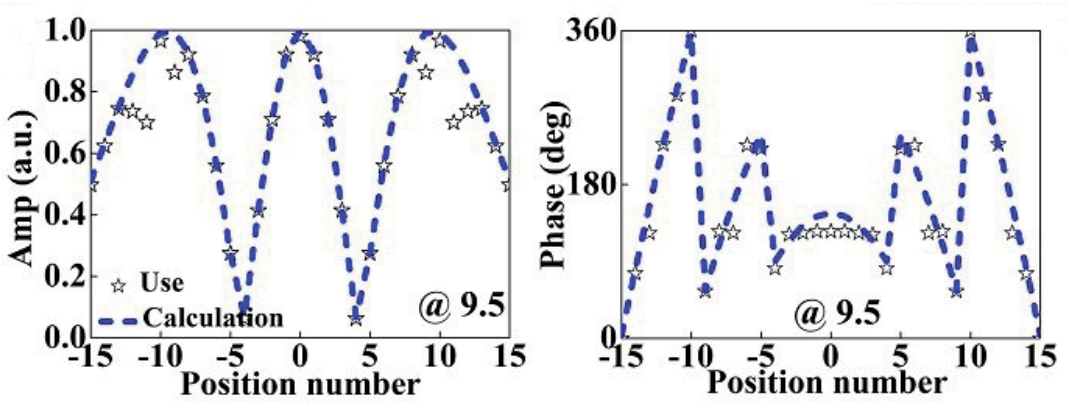

Figure 2b. The required (blue dashed) and digitized (pentacle) normalized amplitudes (left) and phases (right) of the designed lateral bifocal metalens in the one-dimensional case.

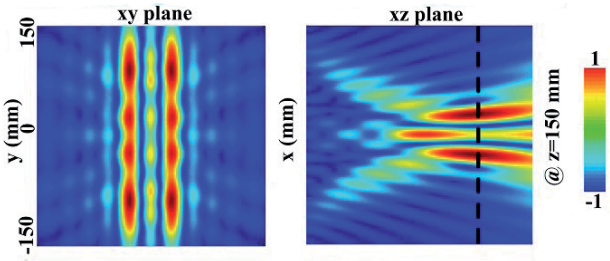

Figure 2c. The theoretically calculated E-field distributions in the *xy* (left) and *xz* (right) planes for the one-dimensional case at 9.5 GHz.

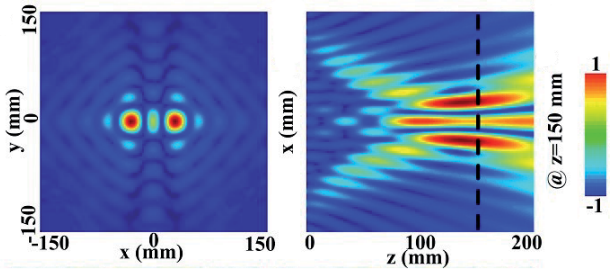

Figure 2e. The theoretically calculated E-field distributions in the *xy* (left) and *xz* (right) planes for the two-dimensional case at 9.5 GHz.

3. Bifocal Metalens with Lateral or Axial Alignment of Two Foci

We demonstrated the possible applications of our flexible metasurface by designing and examining two bifocal metalenses with lateral or axial alignment of two foci. For these purposes, the required phase and amplitude profiles across the aperture should fulfill the following conditions:

$$\sigma(x,\lambda) = \alpha_1 e^{j\frac{2\pi}{\lambda}\left[\sqrt{(x-d/2)^2+F^2}-F\right]} + \alpha_2 e^{j\frac{2\pi}{\lambda}\left[\sqrt{(x+d/2)^2+F^2}-F\right]}, \quad (9a)$$

$$\sigma(x,\lambda) = \alpha_1 e^{j\frac{2\pi}{\lambda}\left(\sqrt{x^2+F_1^2}-F_1\right)} + \alpha_2 e^{j\frac{2\pi}{\lambda}\left(\sqrt{x^2+F_2^2}-F_2\right)}. \quad (9b)$$

Here, λ was the designed wavelength at $f_0 = 9.5$ GHz, α_1 and α_2 were the strengths of the two foci, $F = 150$ mm was the focal point, $d = 60$ mm was the lateral distance between the two foci of the first metalens, and $F_1 = 55$ mm and $F_2 = 130$ mm were the two axial focal points of the second metalens. Both lenses were targeted at 9.5 GHz with $\alpha_1 = \alpha_2 = 0.5$.

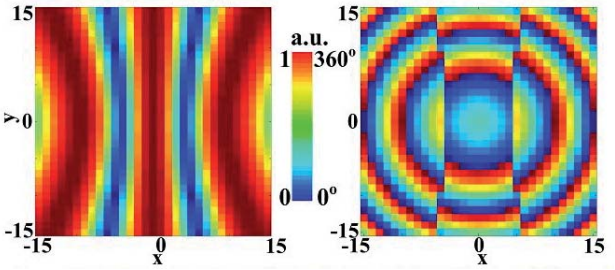

Figure 2d. The required (blue dashed) and digitized (pentacle) normalized amplitudes (left) and phases (right) of the designed lateral bifocal metalens in the two-dimensional case.

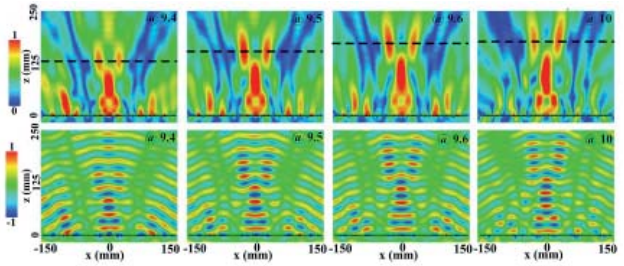

Figure 2f. The numerically simulated E_x distributions for both $\mathrm{Mag}(E_x)$ (top row) and $\mathrm{Re}(E_x)$ (bottom row) at several representative frequencies.

Figure 2 plots the layout and exotic properties of the first metalens exhibiting dual lateral foci based on performing both theoretical predictions and full-wave FDTD simulations, where we illuminated the metalens with normally a incident *y*-polarized plane wave along the *z* direction and recorded the scattered *x*-polarized radiation. Since it is not easy to realize all-level amplitude and phase patterns, we utilized six-level (pentacle) phase modulation to digitize the required full profiles (dashed) in the one-dimensional case. Each level corresponded to a meta-atom with specific radius, as portrayed in Figure 2a, and the orientations of these were determined with minimum amplitude tolerances as shown in Figure 2b. More design details for each pixel can be found in Table 1. Consistent amplitude and phase profiles could be appreciated between the full and digitized values. As could be seen from Figures 2c, 2e, and 2f, the prescribed dual-focusing behavior with lateral alignment of two foci along the *x* direction with $d = 59$ mm were evidently obtained from the theoretical results of both the one-dimensional and two-dimensional metalenses. Due to the passive dispersion, the FDTD simulated foci (dashed line) continuously increased, and the two focal intensities became slightly asymmetric as the frequency went beyond f_0. The beamwidth of the two foci measured by the FWHM of the field patterns along the dashed line was approximately 22 mm at 9.5 GHz.

Figure 3 shows the properties of the second bifocal metalens with axial alignment of two foci. Both one-dimensional and two-dimensional metalenses were theoretically designed with their amplitude and phase patterns shown in Figure 3b and 3d. More design details for

Table 1. Detailed design information for the bifocal metalens I with lateral alignment of two foci.

Amplitude	0.6	0.64	0.68	0.7	0.76	0.78	0.78	0.78	0.73	0.65	0.49	0.23	0.16	0.6	0.95	0.9
Phase	109°	206°	301°	34.5°	125°	212°	295°	12.9°	84.6°	149°	203°	247°	99.3°	118°	124°	119°
Types	5	7	9	2	5	7	9	1	3	6	7	8	4	5	5	5
***R* (mm)**	4.18	3.78	3.5	4.45	4.18	3.78	3.5	4.49	4.29	4.08	3.78	3.6	4.23	4.18	4.18	4.18
Φ	38°	16°	0°	26°	28°	0°	0°	20.8°	26°	33°	31°	50°	67°	37°	0°	0°
Amplitude	0.6	0.65	0.7	0.73	0.75	0.7	0.7	0.78	0.73	0.65	0.5	0.23	0.17	0.6	0.97	0.97
Phase	120°	209°	285°	24.5°	115°	209°	285°	9 °	81.4°	145°	206°	233°	96.7°	114°	118°	118°

Note: The theoretically required amplitude and phase profiles are given in the top two rows while, the practically utilized profiles are listed in the bottom two rows. Moreover, the spatially varied R and Φ for each meta-atom are marked in yellow. As shown, reasonable agreement of amplitude and phase patterns was observed between the two cases, enabling a simple design without severely sacrificing the performance of these metalenses.

each pixel can be found in Table 2. In the realization of the one-dimensional lens with the layout shown in Figure 3a, nine-level (pentacle) phase modulations were cautiously performed to digitize the required full one-dimensional phase profile (dashed) depicted in Figure 3b. Again, both theoretical (Figures 3c and 3e) and FDTD (Figures 3f-3h) results agreed well, implying desirable dual focusing from the two localized spots with maximum intensity along the

Figure 3a. The design, theoretical, and numerical characterization of the second bifocal metalens with axial alignment of two foci: the top view of the metalens layout with a total of $M \times N = 31 \times 1$ pixels distributed along the x and y axes.

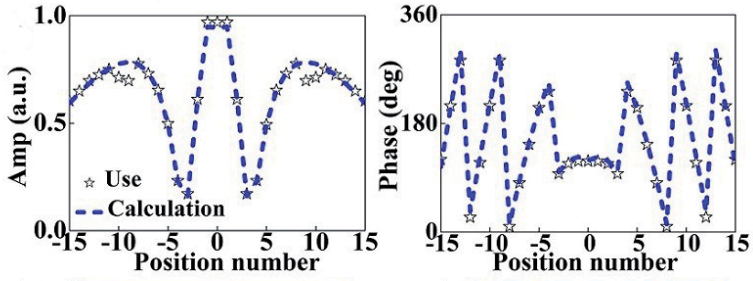

Figure 3b. The required (blue dashed) and digitized (pentacle) normalized amplitudes (left) and phases (right) of the designed lateral bifocal metalens in the one-dimensional case.

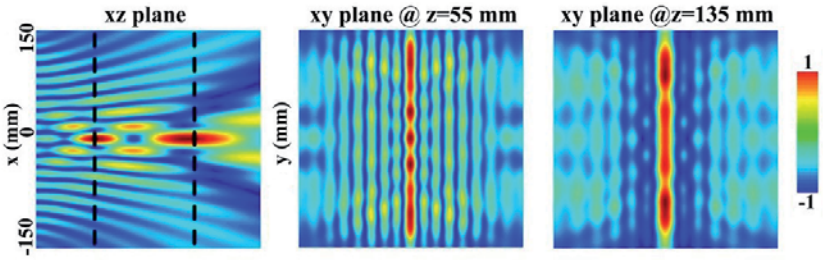

Figure 3c. The theoretically calculated E-field distributions in the *xz* (left) and *xy* (right) planes for the one-dimensional case at 9.5 GHz.

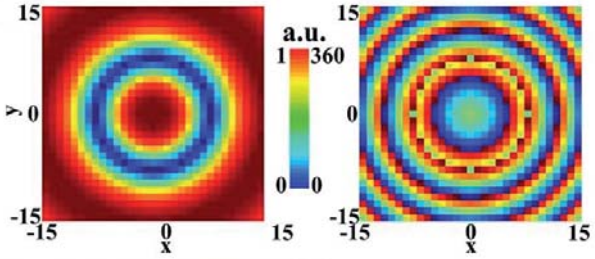

Figure 3d. The required (blue dashed) and digitized (pentacle) normalized amplitudes (left) and phases (right) of the designed lateral bifocal metalens in the two-dimensional case.

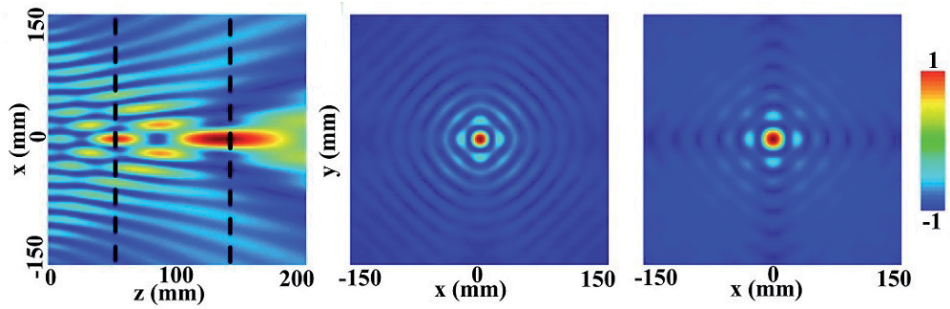

Figure 3e. The theoretically calculated E-field distributions in the *xz* (left) and *xy* (right) planes (at $z = 55$ mm and $z = 135$ mm) for the two-dimensional case at 9.5 GHz.

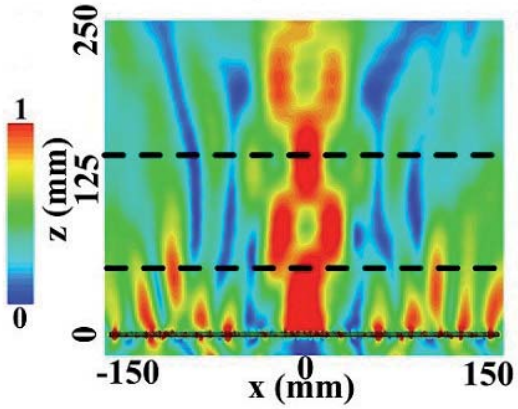

Figure 3f. The numerically simulated E_x distributions for both $\mathrm{Mag}(E_x)$ (top row) and $\mathrm{Re}(E_x)$ (bottom row) at 9.4 GHz and 9.5 GHz.

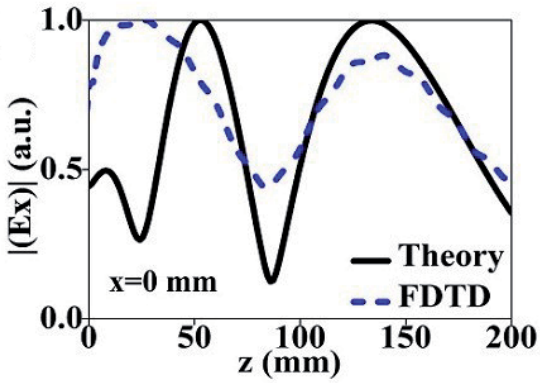

Figure 3g. A comparison of E_x between theoretical and FDTD calculations at 9.4 GHz and 9.5 GHz.

optical axis (*z* axis). Some deviations observed in the FDTD calculations, especially for the non-identical focal intensity at the two foci, were probably induced by the inherently different focusing capability of the finite-size lens at different positions, and the phase/amplitude discrepancies between the utilized meta-atoms and the ideal meta-atoms.

We finally fabricated the first metalens to prove the dual-focusing capability. The metalens sample with the photograph shown in Figure 4a was composed of $M \times N = 31 \times 25$ pixels, with spatially varied structures and orientations. Figure 4b depicts the measured two-dimensional contour of the near-field E_x by scanning an area of 90 mm × 180 mm in steps of 5 mm. All fields were normalized to their maximum. As expected, two focal spots with extremely localized intensity were obtained near $z = 150$ mm at the observed frequencies. As shown in Figure 4c, good agreement could be observed between

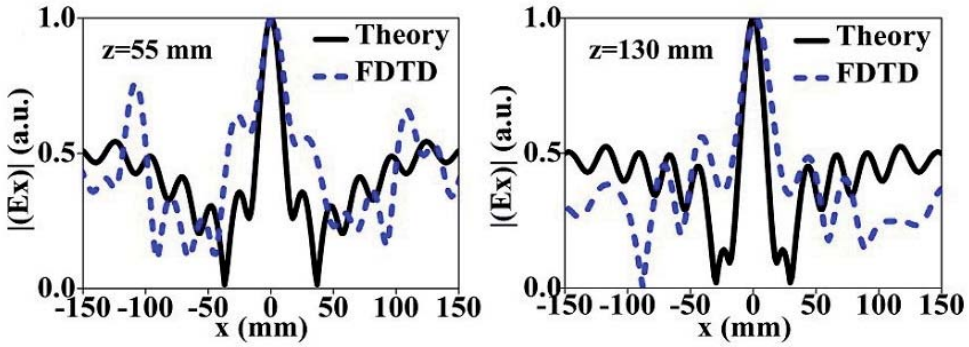

Figure 3h. A comparison between theoretical and FDTD calculations of E_x at the two values of z shown by dashed lines in Figure 3f.

Table 2. Detailed design information for the bifocal metalens II with axial alignment of two foci.

Amplitude	0.51	0.63	0.75	0.86	0.94	0.99	0.99	0.93	0.79	0.57	0.27	0.07	0.41	0.72	0.93	1
Phase	3.3°	80.8°	155°	226°	294°	357°	55.8°	110°	159°	202°	239°	90.1°	114°	132°	143°	146°
Types	1	3	4	5	6	1	2	4	4	5	5	3	4	4	4	4
***R* (mm)**	4.5	4.29	4.15	3.67	3.5	4.5	4.4	4.15	4.15	3.67	3.67	4.29	4.15	4.15	4.15	4.15
Φ	40°	34.5°	28.5°	0°	0°	0°	0°	13.5°	25.5°	27°	47.5°	77°	50°	31°	13.5°	0°
Amplitude	0.5	0.62	0.75	0.74	0.7	0.97	0.86	0.92	0.79	0.56	0.28	0.06	0.41	0.71	0.92	0.98
Phase	0°	76.1°	123°	227°	285°	360°	55.2°	125°	123°	226°	222°	82°	121.4°	123°	125°	125°

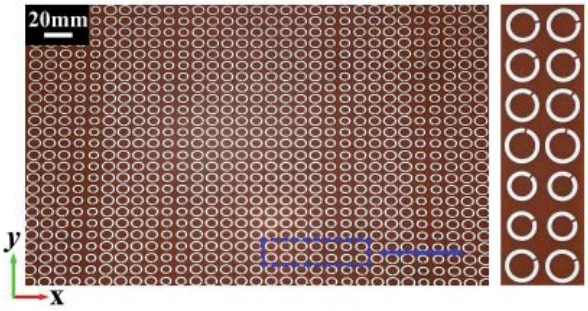

Figure 4a. The experimental characterization of the one-dimensional bifocal metalens with lateral alignment of two foci: a photograph of the fabricated sample with a total of $M \times N = 31 \times 25$ (top view).

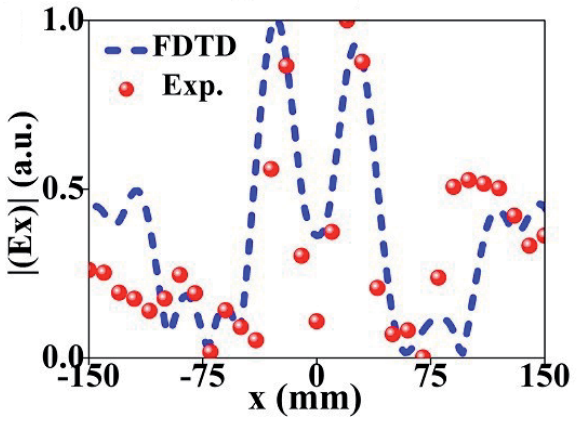

Figure 4c. A comparison of the simulated and measured E_x intensities along the line $z = 150$ mm at 9.5 GHz.

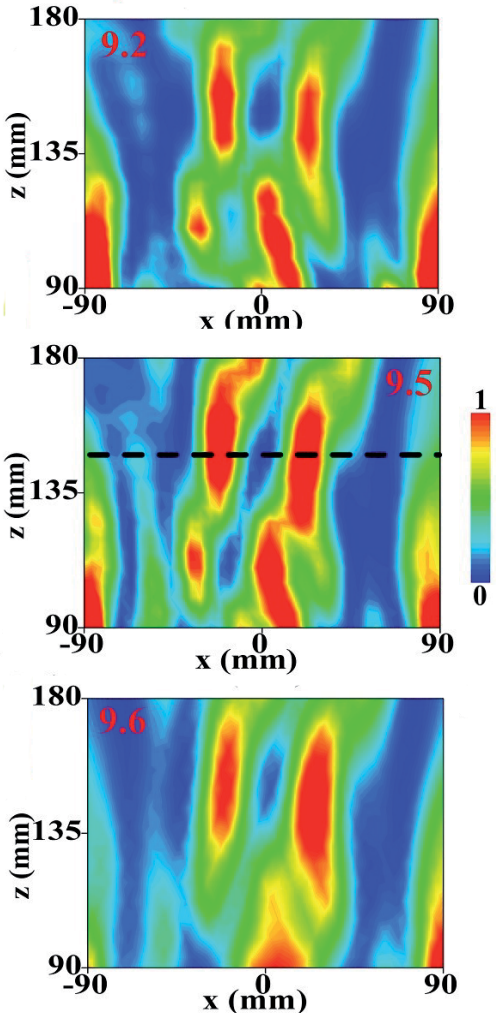

Figure 4b. The experimentally measured E-field (E_x) distributions at 9.2 GHz, 9.5 GHz, and 9.6 GHz.

the theoretical, numerical, and experimental E_x along $z = 150$ mm, indicating measured FWHM beamwidths of 20 mm and 21 mm ($0.63\lambda_0$) for the two foci. The non-ideal alignment of the metalens and the exciting horn gave rise to the slight distortion of the fields, especially for the oblique manifestation of the two foci. Nevertheless, this had little effect on identifying the high-resolution dual-focusing behavior.

4. Conclusion

To sum up, we have proposed and demonstrated an efficient approach for simultaneous manipulation of transmissive polarization, amplitude, and phase with high efficiency from the perspective of analytical derivation, numerical simulation, and experimental demonstration. By stacking triple-layer SRRs with a specific twist angle, vertical-mode cross-coupling was achieved, and thus complete cross-polarization transmission could be engineered within a broad window. Most importantly, the decoupling of changing radius (phase) and orientations (amplitude) afforded us unprecedented degrees of freedom (DOF) for EM wavefront control. For verification, two metalenses that are impossible to realize through phase-only control of conventional metasurfaces were numerically and experimentally investigated with elegant performance.

5. Acknowledgements

This work was supported by the Key Program of Natural Science Foundation of Shaanxi Province (2017KJXX-24); Youth Talent Lifting Project of the China Association for Science and Technology (17-JCJQ-QT-003); China Scholarship Fund (20173059).

6. References

1. N. F. Yu, P. Genevet, M. A. Kats, et al., "Light propagation with phase discontinuities: Generalized laws of reflection and refraction," *Science*, **334**, 2011, pp. 333-337.

2. L. Li, T. J. Cui, W. Ji, S. Liu, J. Ding, X. Wan, Y. B. Li, M. Jiang, C. Qiu, and S. Zhang, "Electromagnetic reprogrammable coding-metasurface holograms," *Nat. Commun.*, **8**, 2017, p. 197.

3. H.-X. Xu, G. Hu, Y. Li, L. Han, J. Zhao, et al., "Interference-assisted kaleidoscopic meta-plexer for arbitrary spin-wavefront manipulation," *Light: Sci. Appl.*, **8**, 2019, p. 3.

4. H.-X. Xu, L. Han, Y. Li, Y. Sun, J. Zhao, et al., "Completely spin-decoupled dual-phase hybrid metasurfaces for arbitrary wavefront control," *ACS Photonics*, **6**, 2019, pp. 211-220.

5. H.-X. Xu, L. Zhang, Y. Kim, G.-M. Wang, K.-X. Zhang, et al., "Wavenumber-splitting metasurfaces achieve multi-channel diffusive invisibility," *Advanced Optical Materials*, **6**, 2018. p. 1800010.

6. H.-X. Xu, S. Tang, C. Sun, L. Li, H. Liu, et al., "High-efficiency broadband polarization-independent super-scatterer using conformal metasurfaces," *Photonics Research*, **6**, 2018, pp. 782-788.

7. H.-X. Xu, S. Ma, X. Ling, X.-K. Zhang, S. Tang, et al., "Deterministic approach to achieve broadband polarization-independent diffusive scatterings based on metasurfaces," *ACS Photonics*, **5**, 2018, pp. 1691-1702.

8. L. Liu, et al. "Broadband metasurfaces with simultaneous control of phase and amplitude," *Adv. Mater.*, **26**, 2014, pp. 5031-5036.

9. Z. Li, H. Cheng, Z. Liu, S. Chen, and J. Tian, "Plasmonic airy beam generation by both phase and amplitude modulation with metasurfaces," *Adv. Opt. Mater.*, **4**, 2016, pp. 1230-1245.

10. Y. Zhu, et al., "Fine manipulation of sound via lossy metamaterials with independent and arbitrary reflection amplitude and phase," *Nat. Commun.*, **9**, 2018, p. 1632.

11. C. Pfeiffer and A. Grbic, "Metamaterial Huygens' surfaces: tailoring wave fronts with reflectionless sheets," *Phys. Rev. Lett.*, **110**, 2013, p. 197401.

12. H.-X. Xu, G. Hu, Y. Li, L. Han, M. Jiang, et al., "Chirality-assisted high-efficiency metasurfaces with independent control of phase, amplitude and polarization," *Advanced Optical Materials*, **7**, 2019, p. 1801479.

13. Y. Zhao, M. A. Belkin, and A. Alù, "Twisted optical metamaterials for planarized ultrathin broadband circular polarizers," *Nat. Commun.*, **3**, 201 2, p. 870.

In Memoriam: Tatsuo Itoh
1940 - 2021

It is not easy to describe the shock and pain of our community after receiving the sad news of the passing of Prof. Tatsuo Itoh. It is so unfortunate that Prof. Itoh accepted giving an invited talk after the Covid-19 pandemic at GASS 2021. It is very hard to find anyone else who has contributed so much, so deeply, and inspired so many people in microwave engineering. Prof. Itoh continuously introduced revolutionary breakthroughs, one after another, until his passing. His gigantic work, remarkable for its quality and diversity, constitutes an extraordinary asset that will guide our explorations and investigations for decades to come. We express our endless recognition and respect for his legendary life and integrity. We express our deepest and sincere condolences to his family.

Tatsuo Itoh received the PhD in Electrical Engineering from the University of Illinois, Urbana, in 1969. After working for the University of Illinois, SRI, and the University of Kentucky, he joined the faculty at the University of Texas at Austin in 1978. There, he became a Professor of Electrical Engineering in 1981. In September 1983, he was selected to hold the Hayden Head Centennial Professorship of Engineering at the University of Texas. In January 1991, he joined the University of California, Los Angeles, as Professor of Electrical Engineering and holder of the TRW Endowed Chair in Microwave and Millimeter Wave Electronics (currently, the Northrop Grumman Endowed Chair). He received a number of awards, including the IEEE Third Millennium Medal in 2000 and the IEEE MTT-S Distinguished Educator Award in 2000. He received the Nikola Tesla Award in 2001. He was elected a member of the US National Academy of Engineering in 2003. He received an honorary doctorate from the Universitat Autonoma de Barcelona. He also received the 2018 Electromagnetics Award from the IEEE for "contributions to electromagnetic modeling, artificial materials, microwave electronics, and antennas."

Dr. Itoh was a Fellow of URSI, a Life Fellow of the IEEE, a member of the Institute of Electronics and Communication Engineers of Japan, and Commissions B and D of USNC-URSI. He served as the Editor-in-Chief of the *IEEE Transactions on Microwave Theory and Techniques* for 1983-1985. He was President of the IEEE Microwave Theory and Techniques Society in 1990. He was the Editor-in-Chief of the *IEEE Microwave and Guided Wave Letters* from 1991 through 1994. He was elected as an Honorary Life Member of MTT Society in 1994. He was the Chair of Commission D of International URSI for 1993-1996. He served on advisory boards and committees of a number of organizations. He served as Distinguished Microwave Lecturer on Microwave Applications of Metamaterial Structures of IEEE MTT-S for 2004-2006. He had 450 journal publications, 900 refereed conference presentations, and had written 48 books and book chapters in the area of microwaves, millimeter-waves, antennas, and numerical electromagnetics. He generated 80 PhD students.

Testimonies

Prof. Makoto Ando
URSI President 2017-2021

I was informed of the sad news about the death of Prof. Tatsuo Itoh. His academic and industrial contributions had been really great and wide enough to cover all of radio science. He served as the Commission D Chair of URSI, and inspired many young radio scientists. He frequently visited Japan and stimulated the microwave community also in Japan. Many students with his guidance are leading the microwave community in Japan. The Microwave Workshop and Exhibition (MWE), being supported by him, has grown up to be the among the most important events in the IEICE Japan, where academia and industry collaborate. I personally remember his visit on my invitation to and a lecture at Tokyo Institute of Technology in March 2006, for advising how to encourage graduate students, especially in the doctoral course. His experience in engineering education has thus been surviving in the future of Tokyo Tech, as well. We shall continually pray for Prof. Tatsuo Itoh and his family.

Dr. Gregory Lyons
2021 MTT-S President

Members of the IEEE Microwave Theory and Techniques Society (MTT-S) feel great sadness over the loss of Prof. Tatsuo Itoh. Tatsuo was one of our cherished leaders, and truly one of the pillars of our Society. He was an educator, mentor, colleague, and friend to so many of us. He was a Life Fellow of the IEEE, served as 1990 MTT-S President,

and received the 2001 Nikola Tesla Award, IEEE Third Millennium Medal, and the 2018 IEEE Electromagnetics Award. The MTT-S named a best journal paper award after him. Tatsuo was active as a voting Honorary Life Member of our MTT-S Administrative Committee until his passing. A biographical journal article captures Tatsuo's life from childhood through the evolution of his career ("Terahertz Pioneer: Tatsuo Itoh," *IEEE Trans. THz Sci. Technol.*, **4**, May 2014, pp. 298-306). Tatsuo's inspiration will live long within MTT-S.

Dr. Apostolos Georgiadis
Chair of URSI Commission D

I saw Prof. Itoh for the first time when I began attending the IEEE MTT-S International Microwave Symposium about twenty years ago. However, I was already aware of his work from my first steps in the research world as many other students and researchers around the world. I managed to speak briefly to him several years later on a few occasions during IMS and APMC conferences. I was very nervous to finally speak to one of the greats of the microwave community. I can remember that Prof. Itoh was concise and always to the point, transmitting a great sense of respect but without being distant. Several years later, I had the pleasure to collaborate more closely with him within URSI Commission D. He was always accessible, present in all Commission D meetings, and he always contributed towards development of the Commission, concisely and meaningfully, from highlighting emerging topics, to attracting new members and to successfully merging the electronics and photonics worlds of Commission D. He has left an unparalleled legacy to the microwaves and electromagnetics communities, and I feel privileged to have met Prof. Itoh. I would like to express my deepest condolences to his family.

Prof. Smail Tedjini
University Grenoble Alpes

My first contact with Prof. Itoh was, as for many, through his publications in the 1980s. His work inspired and guided me to move forward for my PhD. I had the enormous privilege of having him as a member of my thesis jury, and of meeting him in Grenoble in November 1985. During his stay in Grenoble, we had very inspiring discussions on many subjects, not exclusively scientific! I will always remember the pleasant walk in the Vercors park around Grenoble. His intelligence and open-minded remarks had a decisive impact on my activities after my PhD. Later, it was with great pleasure that I had the opportunity to meet him during various events. My last contact was to invite him to participate in a special session for the 100th anniversary of URSI. He accepted the invitation with great reactivity and simplicity. Prof. Itoh will continue to be a reference and a shining and guiding beacon for our scientific community. May he rest in peace.

Prof. Alwyn. J. Seeds
University College London

I knew him for over 30 years, during which time I enjoyed regular visits to his group at UCLA, and worked with him on conference organization for both the IEEE Microwave Theory and Techniques Society and URSI. What distinguished everything he did was his quest for perfection. Any modeling must be accurate. Any deadline must be perfectly met. He was one of the most hard-working people I have known and inspired all who worked with him to give of their best. He had an abiding curiosity for new technology and made remarkable contributions to our field throughout his career. His legacy will long remain, both from his own work and from the work of the many PhD students who benefited from his inspiring training.

Prof. Victor Fouad Hanna
University Pierre et Marie Curie – Sorbonne University

I have known Professor Tatsuo Itoh since 1982, through meeting him nearly every year in International Microwave Symposiums (IMS), European Microwave Conferences, URSI General Assemblies, joint USA URSI AP-S Symposiums, and through participating with him in many of their subcommittees related to electromagnetism. In 1983, he accepted my invitation to visit my newly created research team on the application of electromagnetism to microwave and millimeter circuits at the French National Center of Telecommunication Studies (CNET) in the Paris area. I profited largely from his advices and remarks in defining proper orientations for the research of the team. He accepted many times my invitations to him to participate in the jury of many PhD and DSc theses submitted by my students. He also accepted my invitations several times in the period from 1988 to 1992 to give lectures to members of the newly created France MTT-S Chapter. I visited him when he invited me to his university at Austin in 1990. I summarize: I learned much from Tatsuo during nearly 40 years. My thoughts go to his wife and his daughter, to whom I express my deepest, heartfelt condolences and most heartfelt sympathy.

Prof. Jenshan Lin
University of Florida

Prof. Itoh was my PhD advisor. I was fortunate to be the first UCLA student joining his group in December 1990, when he moved from UT Austin to UCLA. He took me in and trained me, even though I knew nothing about microwave circuits. His generosity and philosophy of education changed a young student's life and shaped his career. His research vision is something I always tried to learn. Whatever he did, whether theoretical or experimental, eventually would lead to significant impacts. I was watching

his online APMC2020 plenary talk, trying to get some ideas of applying metasurfaces to future microwave systems and applications. Sad to know that this was his last conference presentation. He told me 30 years ago that he would never retire. Indeed, he continued to work and contribute to this world until his last moment. He has left us, but his impacts will live forever.

Prof. Dr. Peter Russer

I am saddened to hear of Tatsuo Itoh's death. Tatsuo has been an outstanding member of our MTT family for decades. His achievements combined excellence in numerous fields. Among the international community of engineers, he was known as a leading thinker and a driver of research in the area of microwaves, millimeter-waves, microwave circuits, metamaterials, antennas, and numerical electromagnetics. In all these areas, he was a creative and skilled problem solver with a lot of innovative ideas, and he contributed significantly to the sum of knowledge in microwave theory and techniques. I remember many encounters at conferences and in the context of mutual visits, and the fruitful discussions that took place. With Tatsuo, we have lost a good friend and a significant member of our community. I will miss Tatsuo.

Dr. Nasimuddin
Institute for Infocomm Research A*STAR

I am very saddened to hear of Prof. Tatsuo Itoh's death. He has been an outstanding member of our MTT-S/AP-S family for decades. His achievements combined excellence in the passive to active microwave/millimeter-wave components and systems. He will be a role model for MTT-S/AP-S related engineers and researchers as he was a leading researcher in the area of microwaves, millimeter-waves, microwave circuits, metamaterials, antennas, and numerical electromagnetics. I started my research with reading his research works and was highly motivated. I recall many encounters with him at conferences, most recently in APMC 2019 Singapore, Singapore visits as a visiting professor, and had wonderful discussions. We have lost a good friend, great professor, and a key member of our community. I will miss Prof. Tatsuo.

Prepared by

Smail Tedjini
Past Chair of URSI Commission D
Université Grenoble-Alpes
Grenoble-INP/LCIS
LCIS, 50 Rue Laffemas, BP 54,Valence 26902 France
E-mail: Smail.Tedjini@grenoble-inp.fr

Apostolos Georgiadis
Chair, URSI Commission D
Institute of Sensors, Signals and Systems
Heriot-Watt University
Edinburgh EH14 4AS, United Kingdom
E-mail: apostolos.georgiadis@ieee.org

Book Review

George Trichopoulos
Electrical, Computer & Energy Engineering ISTB4 555D
Arizona State University
781 E Terrace Road, Tempe, AZ, 85287 USA
Tel: +1 614 364 2090
E-mail: gtrichop@asu.edu

Surface Electromagnetics With Applications in Antennas, Microwave, and Optical Engineering, edited by Fan Yang and Yahya Rahmat-Samii, Cambridge, Cambridge University Press, 2019; ISBN: 9781108556477 (online); ISBN: 9781108470261 (print)

This is a fascinating book, presenting an exciting and timely set of topics in surface electromagnetics (SEM). With contributions from prominent and pioneering scientists and engineers in this field, the book covers a wide range of subject matter related to electromagnetic field and wave interaction with a variety of structures categorized as "surfaces." The editors, Profs. Yang and Rahmat-Samii – two of the most outstanding and innovative pioneers in electromagnetics – have assembled and compiled a comprehensive set of topics, ranging from fundamental aspects of wave-surface interaction, such as modeling, analysis, and synthesis of SEM, to guided waves, leaky waves, plane wave features of such surfaces to various applied areas, e.g., cloaking and transparency, to orbital angular momentum, and microwave, THz, and optical applications.

In Chapter 1, Fan Yang and Yahya Rahmat-Samii give an informative introduction and overview of the subject matter. They set the stage by providing the reader with the definition, development, and importance of surface electromagnetics, along with some research frontiers in this topic. They aptly state that the electromagnetic surface paradigm is indeed part of the natural progression in the classification of EM phenomena from zero-dimensional (0D – circuits), to one-dimensional (1D – transmission line), to two-dimensional (2D – surface electromagnetics, this book), and to three-dimensional (3D – general EM problems). This is indeed the spatial categorization of EM interaction with matter, analogous to the temporal categorization based on the frequency of operation, such as dc, RF, microwave, THz, IR, visible, and UV, etc. Another classification of electromagnetic surfaces, as described in Chapter 1, is based on the nature of the surface in terms of spatial variation of surface features along the surface, i.e., from uniform surfaces (e.g., flat surfaces and interfaces between different media), to periodic surfaces (e.g., frequency-selective surfaces, soft/hard surfaces, and EBG surfaces), to quasi-periodic surfaces (e.g., reflectarrays and transmitarrays). One of the important features of electromagnetic surfaces is the possibility of their being tailored to achieve specific functionalities. Such specially engineered surfaces, often called metasurfaces, can provide platforms for desirable electromagnetic responses. This may include engineered responses based on the magnitude, phase, and/or polarization of incoming waves. Examples such as the soft/hard surfaces, high-impedance ground planes, and electromagnetic bandgap surfaces are among the well-known cases.

Chapter 2, by Viktar Asadchy, Ana Diaz-Rubio, Do-Hoon Kwon, and Sergei Tretyakov, discusses analytical models and tools useful for handling the wave interaction with electromagnetic surfaces. It describes the polarizability-based model, the susceptibility-based model, and the equivalent-impedance-matrix-based model. Other topics, such as bi-anisotropy, bi-isotropy, and non-reciprocity, along with the functionality of metasurfaces in shaping and controlling waves in transmission and reflection, are presented in this chapter.

Christopher Holloway and Edward F. Kuester describe the techniques of Generalized Sheet Transition Conditions (GSTCs) in the analysis of metasurfaces in Chapter 3. This versatile tool provides the necessary boundary conditions for wave interaction with metafilms, metascreens, and metagratings, based on which the reflection and transmission coefficients from these surfaces are obtained. From this information, the chapter presents the retrieval expressions and the methods to determine surface parameters. Several applications of GSTCs, such as guided waves along a single metasurface, reduction of resonator size, and meta-film-based waveguides, are also given in this chapter.

The synthesis of metasurfaces is presented by Karim Achouri, Yousef Vahabzadeh, and Christophe Caloz in Chapter 4. Metasurface boundary conditions and synthesis procedures are given, and the examples for negative-refraction metasurfaces, non-gyrotropic non-reciprocal metasurfaces, and time-varying half-wave absorbers are discussed. Some practical realizations are also mentioned.

Maokun Li gives the detailed modeling and analysis of quasi-periodic surfaces, with attention to reflectarrays, in Chapter 5. The reduced basis method is utilized in numerical analysis of such quasi-periodic structures. Moreover, the comparison between the reflection phase in the quasi-periodic and in infinitely periodic cases is explored.

Chapter 6, authored by Eva Rajo Iglesias, Zvonimir Sipus, and Ashraf Uz Zaman, deals with the specialized waveguides known as gap waveguides, in which customized surfaces inside parallel-plate waveguides cause desired guided modes along particular paths. Various examples, such as glide-symmetry holey waveguides and bed-of-nails guided-wave structures with ridges, grooves, inverted microstrips, and microstrip ridges, fall into this class of gap waveguides. The gap waveguide antennas are also discussed as an example of RF applications of such structures.

Metasurface antennas, as one of the "metasurfing" applications, are presented by Gabriele Minatti, David Gonzales-Ovejero, Enrica Martini, and Stefano Maci in Chapter 7. In such structures, spatial modulation of the surface features causes conversion of surface waves into leaky waves. Various parameters can be tailored in the design of such antennas, providing useful methods for the design of conformal antennas with desired properties such as shaped-beam metasurface antennas and multibeam metasurface antennas.

Fan Yang and Shenheng Xu discuss such electromagnetic surfaces as transmitarray antennas and transmission surfaces in Chapter 8. The transmission phase is an important quantity that is engineered by such properly designed transmission surfaces. Reconfigurable surfaces are also explored and presented in this chapter.

Chapter 9, by Shuo Liu and Tie Jun Cui, presents another interesting paradigm that benefits from metasurfaces, namely coding and programmable metasurfaces. Here, the two concepts of coding and metasurfaces have been merged, resulting in controllable manipulation of EM waves. Programmable metasurfaces in the presence of a point source and for imaging applications are discussed.

Giuseppe Labate, Ladislau Matekovits, and Andrea Alu discuss the cloaking concepts and applications using metamaterials and metasurfaces in Chapter 10. Plasmonic cloaking, involving volumetric metamaterial coating, mantle cloaking, and parity-time symmetry cloaking, are presented. Some of the fundamental issues, such as bounds on cloaking, bandwidth issues, and directionality, are also given.

Mehdi Veysi, Caner Guclu, Filippo Capolino, and Yahya Rahmat-Samii investigate how textured surfaces can be utilized to generate orbital-angular-momentum (OAM) beams in Chapter 11. They discuss the near-field and far-field applications of such OAM beams. They also present the reflectarrays that generate desired phase patterns needed to construct Bessel-Gaussian and Laguerre-Gaussian beams. The reflectarrays with cone-shaped patterns are also discussed in this chapter.

Finally, in Chapter 12, Daniel Binion, Lei Kang, Zhi Hao Jiang, Shengyuan Chang, Xingjie Ni, and Douglas H. Werner give descriptions of a series of applications of metasurfaces in the microwave, THz, and optical regimes, some of which include ultra-thin absorbers, antenna grounds for low-profile antennas, scattering signature control, reflectarrays and transmitarrays, THz modulators, a polarization controller, metalenses, holography, and optical invisibility cloaks.

The book also has an excellent appendix by Fan Yang, Yahya Rahmat-Samii, Xibi Chen, Xingliang Zhang, and Hongling Xu, citing many representative references that are organized based on various topics. This is a highly valuable resource for the reader.

In summary, this is a great book to have as a reference for various aspects of electromagnetic surfaces. It is an informative source, and it is inspirational to those interested in entering this exciting field of research. I am confident you will treasure your copy.

Nader Engheta
Department of Electrical and Systems Engineering
University of Pennsylvania, Philadelphia, PA, USA
E-mail: engheta@ee.upenn.edu

[Editor's Note: An earlier version of this book review originally appeared in the August 2020 issue of the *IEEE Antennas and Propagation Society Magazine*. The review is reprinted with permission from the IEEE.]

Et Cetera

Tayfun Akgül
Istanbul Technical University
Dept. of Electronics and Communications Engineering
Telecommunications Division
80626 Maslak Istanbul, Turkey
Tel: +90 212 285 3605; Fax: +90 212 285 3565
E-mail: tayfunakgul@itu.edu.tr.

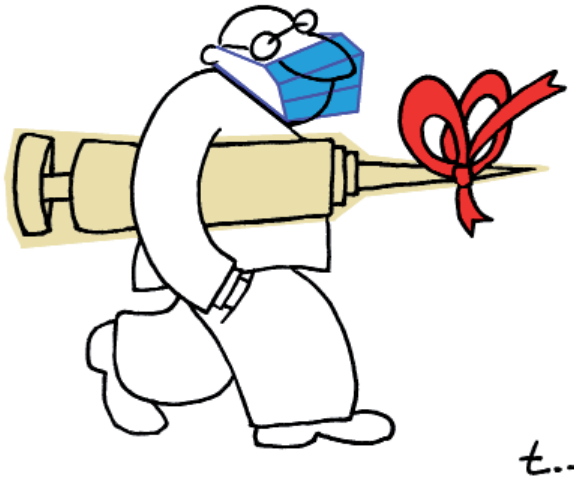

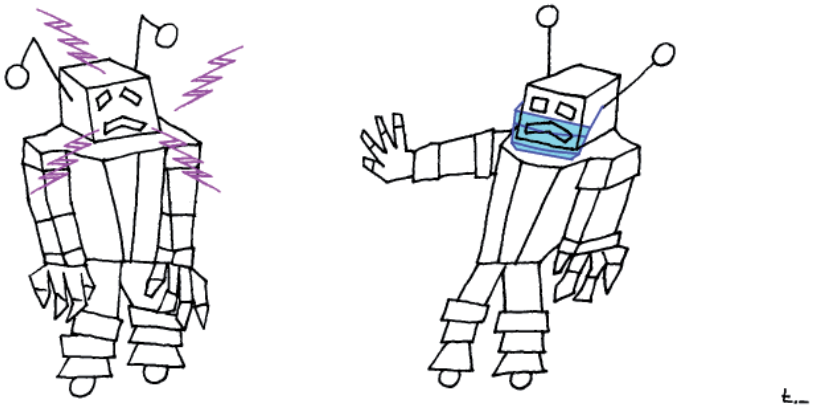

Stefan J. Wijnholds
Netherlands Institute for Radio Astronomy
Oude Hoogeveensedijk 4
7991 PD Dwingeloo, The Netherlands
E-mail: wijnholds@astron.nl

Young Scientist and Student Paper Activities at URSI GASS 2020

2020 was a challenging year, with COVID-19 measures across the globe posing severe restrictions on people moving around and meeting in person. This also affected our scientific community. Many organizers of scientific events had to cancel or postpone their events. Among them was URSI, which decided to postpone the URSI GASS 2020 to 2021, hoping that doing so would allow the URSI scientists to meet in person again or, at least, a significant fraction of them in the case of a hybrid event. As this decision was made after the submission deadline, not everything was or could be postponed by one year. In view of timeliness, all authors were given the opportunity to have their contribution included in the proceedings of the URSI GASS 2020. Young Scientist (YS) Awards were also granted, and the Student Paper Competition (SPC) was held, with the SPC finally conducted as a virtual event. In this ECR column, we feature two short reports on the YS Awards and the SPC. These reports were kindly provided by the Young Scientist Panel, consisting of Phil Wilkinson (Chair), Peter van Daele, Stefan J. Wijnholds, and Inge Lievens; and Sembiam R. Rengarajan (Chair of the SPC), respectively.

1. Young Scientist Awards at the URSI GASS 2020 (Report provided by the Young Scientist Panel)

1.1 Background

The Young Scientist (YS) Awards are presented at URSI Flagship meetings, these being the General Assemblies of URSI, the URSI Atlantic Radio Science Conferences (AT-RASC), and the URSI Asia-Pacific Radio Science Conferences (AP-RASC). The awards are presented to recognize an international group of individuals who have made innovative contributions and discoveries in multidisciplinary research related to the topics of the URSI Commissions.

In general, the three URSI Flagship meetings are held in a three-year cycle, to review current research trends, present new discoveries, and make plans for future research and special projects in all areas of radio science, especially where international cooperation is desirable. Young researchers can apply for a YS Award at any of these three URSI Flagship meetings. A YS Award is primarily a recognition of the scientific value of the work presented in the paper submitted by the young researcher. It links to financial support through waiving registration fees, in some cases also providing accommodation or even travel support when originating from specific and selected countries.

To qualify for an award, the applicant:

- must be less than 35 years old on September 1 of the year (2020) of the URSI General Assembly and Scientific Symposium;
- should have a paper, of which he or she is the principal author, submitted and accepted for oral or poster presentation at a regular session of the General Assembly and Scientific Symposium.

Applicants should also be interested in promoting contacts among developed and developing countries.

Applicants from all over the world are welcome, including from regions that do not (yet) belong to URSI. All successful applicants are expected to participate fully in the scientific activities of the URSI Flagship Meetings.

Applications are assessed by the URSI YS Panel, taking account of the national ranking of the application and the technical evaluation of the abstract by the relevant URSI Commission.

After the call for the YS Awards of the URSI GASS 2020, 247 applicants from 40 countries were received through an online application procedure.

1.2 Selection Process

The selection process was carried out in four steps:

1. The URSI Secretariat checked eligibility (first author, age limit, submission of required documents,...). Eight candidates were removed from the list in this step, as they were not eligible.

2. The Chair, Vice-Chair, and ECRs of each of the 10 URSI Commissions were asked to rank the applicants who submitted a paper in one of the sessions organized in their Commission, purely based on the scientific merit of the work presented in the paper.

3. In parallel, the Member Committees were asked to rank the applicants originating from their country or region based on local, practical, technical, or other issues.

4. The rankings by the Commissions and the Member Committees were combined in a score by the YS Panel to come to a final selection, taking into account a proper balance over the 10 URSI Commissions, a proper geographical spreading, as well as a gender balance. During this final step, it was always made sure that the selected awardee had a paper of significant technical value, and in some specific cases the YS Panel also considered the comments provided by the reviewers during the reviewing process for all submitted papers at the GASS 2020.

Finally, the YS Panel submitted a list of 121 awardees to the URSI Board. After careful consideration, the URSI Board approved the proposed selections, and all awardees were contacted. By the deadline for acceptance, 116 Young Scientists accepted their award, and indicated they would comply with the requirements to submit a presentation by 15 August.

1.3 YS Awardees

Afzal, Muhammad Usman (Australia)
Akbar, Fannush (Indonesia)
Aktepe, Aslihan (Turkey)
Albarracin-Vargas, Fernando (UAE)
Al-Behadili, Hasanain (Iraq)
Ali, Muhsin (Spain)
Ameen, Mohammad (India)
Appusamy, Sowmiyadevi (India)
Bayat, Nozhan (Canada)
Bellizzi, Gennaro Giovanni (Netherlands)
Bereta, Martin (Slovakia)
Bhandari, Shivani (Australia)
Bharali, Chandrakala (India)
Bianco, Giulio Maria (Italy)
Biswas, Sanat (India)
Borchevkina, Olga (Russian Federation)
Brizi, Danilo (Italy)
Camera, Francesca (Italy)
Chakraborty, Rohit (India)
Chowdhury, Swati (India)
Chutia, Lakhima (India)
Comite, Davide (Italy)
Cornejo Espinoza, Deysi Veronica (Brazil)
Cuadrado-Calle, David (United Kingdom)
da Silva, Caitano (USA)
Datta, Soumen (India)
Di Meo, Simona (Italy)
Diaby, Aziz (Côte d'Ivoire)
Diao, Yinliang (Japan)
Ernawan, Ferda (Malaysia)
Fabbri, Davide (Italy)
Fam, Pape Abdoulaye (Senegal)
Fan, Wei (Denmark)
Fedeli, Alessandro (Italy)
Fritz, Bruce (USA)
Fuscaldo, Walter (Italy)
Galiffi, Emanuele (United Kingdom)
Goswami, Samiddha (India)
Gu, Xiaoqiang (Canada)
Guo, Jun (China)
Gupta, Sumedha (India)
Hanzelka, Miroslav (Czech Republic)
Hartley, David (USA)
Huang, Shiyong (China)
Huang, Fuqing (China)
Jaiswal, Rahul Kumar (India)
Jha, Abhishek (India)
Jiang, Zhihao (China)
Jiang, Chunxiao (China)
Jin, Yaqi (Norway)
Juhász, Lilla (Hungary)
Kafal, Moussa (France)
Kasan, Karim (France)
Kochetova, Liudmyla (Ukraine)
Kramer, Kelsey (USA)
Kumar, Abhishek (India)
Kumar Mishra, Vikash (India)

Table 1. The distribution of YS awardees by Commission.

Commission	Total App.	Selected	Acceptance Rate (%)
A	12	6	50.00
B	71	33	46.48
C	17	8	47.06
D	24	12	50.00
E	15	7	46.67
F	31	13	41.94
G	36	16	44.44
H	16	10	62.50
J	7	3	42.86
K	18	8	44.44
Total	**247**	**116**	**46.96**

Table 2. Geographical distribution of YS awardees.

Region	Total App.	Selected	Acceptance Rate (%)
Africa	5	2	40.00
Asia-Pacific	18	10	55.56
China	37	17	45.95
Europe	73	37	50.68
India	54	21	38.89
Middle East	10	5	50.00
N. America	24	13	54.17
Russian Fed.	20	7	35.00
S. America	6	4	66.67
Total	**247**	**116**	**46.96**

Kundu, Subrata (India)
Kurita, Satoshi (Japan)
LasryBenoliel, Gabriel Abraham (Israel)
Lemey, Sam (Belgium)
Li, Yujian (China)
Li, Kun (Japan)
Liu, Moran (China)
Liu, Jake (Taiwan)
Lodi, Matteo Bruno (Italy)
Longley, William (USA)
Martynova, Valery (Russian Federation)
Merlini, Adrien (France)
M.P., Jayakrishnan (France)
Mukherjee, Anwesha (India)
N B, Lakshmi (India)
Na, Dong-Yeop (USA)
Nosikov, Igor (Russian Federation)
O'Loughlin, Declan (Ireland)
Ostafiychuk, Oleg (Russian Federation)
Pacheco-Pena, Victor (United Kingdom)
Pantoja, John (United Arab Emirates)
Pérez-Nicoli, Pablo (Uruguay)
Pratley, Luke (Canada)
Psychogiou, Dimitra (USA)
Rahmouni, Lyes (Italy)
Rajchowski, Piotr (Poland)
Rakshit, Gargi (India)
Raveendran, Athira (India)
Rawat, Harish (India)
Ryabkova, Maria (Russian Federation)
Sabbagh, Dario (Italy)
Sarkar, Debdeep (Canada)
Sarkar, Chandreyee (India)
Schwarz, Benedikt (Austria)
Shirokov, Evgenii (Russian Federation)
Shoaib, Nosherwan (Pakistan)
Singh, Rajesh Kumar (Italy)
Sofiia, Katsko (Ukraine)
Song, Qian (China)
Suclupe, Jose (Peru)
Sun, Shilong (China)
Surco Espejo, Teddy (Brazil)
Svechnikova, Ekaterina (Russian Federation)
Takabayashi, Kento (Japan)
Tao, Mingliang (China)
Teng, Shangchun (China)
Tobon Vasquez, Jorge Alberto (Italy)
Torrisi, Giuseppe (Italy)
Tzarouchis, Dimitrios (USA)
Vybostokova, Tatiana (Czech Republic)
Wang, Xiaoyi (Canada)
Wang, Dedong (Germany)
Wu, Pengde (China)
Wu, Xinglong (Italy)
Xu, He-Xiu (China)
Yue, Dong-Xiao (China)
Zhang, Xuejing (China)
Zhang, Hao (China)
Zhang, Jiayi (China)

1.4 Statistics on Diversity

Table 1 provides an overview of the distribution per Commission, indicating the applications received, the selected awardees, and the acceptance rate.

To give a overview of the geographical spread of the YS Awardees, each of them was assigned to a region, as shown in Table 2. To allow a better interpretation, some countries from which a large number of Young Scientists originated were listed separately from their region (e.g., China, India, and Russian Federation). The geographical distribution is given in Table 2.

Based on the information provided by the applicants, the gender balance given in Table 3 was obtained.

Table 3. Gender distribution of YS awardees.

Gender	Total App.	Selected	Acceptance Rate (%)
Male	181	86	47.51
Female	66	30	45.45
Total	**247**	**116**	**46.96**

1.5 Follow-Up of YS Selection

Names as well as pictures, affiliations, and a link to the submitted paper were available on the URSI Web site. From 29 August until 30 September 2020, an extra link was provided to each of the submitted presentations by the YS. In case a YS failed to submit a presentation, they were removed from the list and were considered as having turned down the award. The YS certificates were mailed to all the YS Awardees. As the GASS 2020 YS Awardees were deprived form any financial reward linked to their award, the URSI Board also decided on the following measures:

- GASS 2020 YS can also submit a modified version of their paper to the *URSI Radio Science Letters* (*RSL*) following the submission guidelines for *RSL* using the proposed reduction in page charges as for other authors of accepted papers at GASS 2020.
- GASS 2020 YS can reapply for a YS Award in 2021, but with a different paper, and they still need to qualify (age, first author, etc.).
- If they attend GASS 2021, GASS 2020 YS can register as a Student (reduced fee).
- If they attend GASS 2021, GASS 2020 YS are invited to the YS Party at GASS 2021.

1.6 Conclusions

This report provided a summary of the process and the outcome of the selection for the GASS 2020 YS. Being aware of the specific situation with respect to the postponement of the GASS 2020 as a physical conference, the URSI Board has taken specific measures to try to keep the YS program active, as this is one of the pillars of URSI and one of the activities within URSI that distinguishes us from other scientific unions. By providing these awards and publicizing this information and these awards through the Web site and social media, the URSI Board had the intention of keeping young researchers interested in URSI and the events organized and supported by URSI. The Board wishes to thank all the individuals involved in this program and selection process, and wishes to congratulate all YS Awardees.

2. Student Paper Competition at the URSI GASS 2020

(Report provided by Sembiam R. Rengarajan, Chair of Student Paper Competition)

George Uslenghi, General Chair of the URSI General Assembly in Chicago in 2008, was instrumental in motivating URSI to initiate the URSI International Student Paper Competition (SPC), and in encouraging the United States National Committee for URSI (USNC-URSI) to fund the prizes. The SPC in the URSI General Assembly and Scientific Symposium (GASS) 2020 was once again financially sponsored by the United States National Committee (USNC) for URSI. This was the seventh international URSI SPC sponsored by the USNC-URSI, five in URSI GASS and two in AT-RASC.

There were 53 eligible applicants for the SPC. The rules for the SPC were published in the URSI GASS 2020 Web site, and they are repeated here.

Rules for the SPC:

- The first author and presenter must be a full-time university student.
- The topic of the paper must be related to the field of one of the ten URSI Commissions.
- A Full Paper, not longer than 10 pages and not shorter than four pages, in single-column, single-spaced format, meeting the requirements of the URSI template, must be submitted by the date set for URSI GASS 2020.
- Submissions should be made through the online paper-submission system set up for each of the meetings, with indication of the willingness to participate in the Student Paper Competition.
- The Full Paper will be evaluated within the competition, and will not be published to ensure that there are no subsequent prior-publication issues for those students who wish to submit the work to a journal. This means that the ten-page Full Paper will not be included in the symposium proceedings.
- The student must also submit a Summary Paper or Extended Abstract on the same subject to the appropriate session. The Summary Paper or Extended Abstract will be included in the symposium proceedings.
- A paper that is submitted to a journal before submission to the student competition is ineligible.
- A letter from the student's advisor on university letterhead must be appended to the Full Paper. The letter must state that the author is enrolled as a full-time university student in a degree program. If the Full Paper is coauthored, the letter must state that all coauthors played only an advisory role. No other students are permitted as coauthors.
- Ten to twelve finalists will be chosen based upon quality, originality, and scientific merit. They will receive free access to all social activities at the URSI Flagship Meetings, and will be recognized. Prizes will be presented to the top finalists.
- The finalists will present their papers in a special SPC session at each of the URSI Flagship Meetings. They will be judged by a panel consisting of the ten URSI Commission Chairs or their authorized representatives.
- The prizes will be awarded based on the clarity of the presentation, adherence to time, accessibility to the

broad audience of the ten URSI Commissions, and the ability to answer questions on the work.

Commission Chairs or their representatives served as the jury in the process of selecting the finalists, and later in selecting the cash prize winners. Since one of the Commission Chairs was the advisor of an applicant, the Vice-Chair of that Commission served as a jury member.

Each member of the jury recommended three expert reviewers for each paper submitted to his or her Commission. Each reviewer provided a thorough review of each paper. The criteria used by reviewers were the quality, originality, and scientific merit. Each reviewer gave an overall score between 1 and 5, 5 being the best. The top-21 papers were subsequently selected based on the average reviewers' score for each paper. These 21 papers had an average score of 4.0 or better. The jury subsequently ranked these papers from 1 to 21, 1 being the best. The jury had access to reviewers' comments and scores. Twelve finalists were chosen based on the ranking of the jury. One of them withdrew from the competition.

Because of the COVID-19 pandemic, URSI GASS 2020 was postponed. However, the URSI Board and the USNC-URSI officers decided to schedule the SPC finalist presentations virtually. The URSI Secretary-General, Peter Van Daele, optimized the presentation schedule so as not to inconvenience the jury and finalists in different time zones in the United States, Europe, and the Far East. He set up the virtual-presentation sessions in the GoToMeeting platform, and gave a short orientation session to the finalists and the jury who were not familiar with that tool. The competition was held on three different days, August 31, September 1, and September 3, for the finalists in the US, Europe, and the Far East respectively. This spanned the time zones of early morning in the US West Coast to close to midnight in Japan. Each finalist had 20 minutes for the presentation of the paper and five minutes for questions and answers. The finalist presentations were ranked based on clarity of the presentation, accessibility to the broad audience of the ten URSI Commissions, and the ability to answer questions on the work.

The top five award winners were:

1. First Prize ($1500): Giulia Sacco, Sapienza University, Rome, Italy, for the paper "Vital Signs Monitoring for Different Chest Orientations Using an FMCW Radar" (Commission K)
2. Second Prize ($1250): Miroslav Hanzelka, Institute of Atmospheric Physics, Czech Academy of Sciences, Czech Republic, for the paper "Modeling the Fine Structure of Natural Discrete Plasma Wave Emissions in the Earth's Radiation Belts" (Commission H)
3. Third Prize ($1000): Benjamin Estacio, Stanford University, Stanford, CA, USA, for the paper "Dust and Atmospheric Effects on Light Gas Gun Hypervelocity Impact Experiments" (Commission G)
4. Fourth Prize ($750): Calvin Leung, Massachusetts Institute of Technology, Cambridge, MA, USA, for the paper, "Demonstration of a Synoptic VLBI Technique for Localizing a Non-Repeating Fast Radio Burst with CHIME/FRB" (Commission J)
5. Fifth Prize ($500): Navid Barani, University of Michigan, Ann Arbor, MI, USA, for the paper, "A Handheld Mechanical Antenna with Frequency Multiplication and Phase Modulation Capability" (Commission B)

The following finalists, in alphabetical order, received honorable mention:

6. Luisa Capannolo, Boston University, USA, for the paper, "Subrelativistic Electron Precipitation Driven by Electromagnetic Ion Cyclotron (EMIC) Waves: Multi-Event Analysis Using Multi-Satellite Observations" (Commission H)
7. Lakhima Chutia, Dibrugarh University, India, for the paper, "Distribution of Sulfur Dioxide Over Indian Subcontinent: Remote Sensing Observations and Model Reanalysis" (Commission F)
8. Shuang Liu, the University of Tokyo, Japan, for the paper, "Design of Multi-Locus Transcranial Magnetic Stimulation Coil with Single Driver" (Commission K)
9. Melody Pallu, LPC2E, University of Orleans, CNRS, France, for the paper, "Estimation of Radiation Doses Delivered by Terrestrial Gamma Ray Flashes" (Commission H)
10. Felipe Treviso, Politecnico di Torino, Italy, for the paper, "Machine Learning Applied to the Blind Identification of Multiple Delays in Distributed Systems" (Commission E)
11. Ziwei Wan, Beijing Institute of Technology, China, for the paper, "Multi-User Multi-Stream Hybrid Precoding for Broadband Millimeter-Wave Massive MIMO Systems" (Commission C)

Several people are to be thanked for contributing to the success of the SPC. Inge Lievens provided support throughout this process, often working in the evenings and weekends. Koyama Yasuhiro, Kazuya Kobayashi, Yves Louet, Amir Zaghloul, Apostolo Georgiadis, Frank Gronwald, Virginie Deniau, Chaouki Kasmi, V. Chandrasekar, Patricia Doherty, Jyrki Manninen, Richard Bradley, and Koichi Ito provided valuable service as the jury. Numerous reviewers provided expert reviews of all papers. Peter Van Daele set up the finalist presentations, and helped with the recording of the talks and posting the videos on the URSI Web site. Inge Heleu prepared and sent the certificates to the awardees. Ana Ferreras and James Manning of the National Academies of Science, Engineering, and Medicine in the United States processed the checks for the top five awardees.

Özgür Ergül
Department of Electrical and Electronics Engineering
Middle East Technical University
TR-06800, Ankara, Turkey
E-mail: ozergul@metu.edu.tr

SOLBOX-20: Electromagnetic Interactions with Near-Zero-Index Triangular Prisms

Özgür Eriş and Özgür Ergül

Department of Electrical and
Electronics Engineering
Middle East Technical University
TR-06800, Ankara, Turkey
E-mail: ozergul@metu.edu.t

1. Introduction

With their exotic behaviors that can be useful in a plethora of applications, near-zero-index (NZI) materials have been topics of many recent studies in electromagnetics [1-11]. Specifically, by possessing refractive index values close to zero, such materials can be employed for electromagnetic tunneling, coupling, beam steering and splitting, to name a few [1-8]. Manipulations of electromagnetic waves become possible by NZI structures as they stretch the wavelength to infinity. For example, once electromagnetic waves enter an NZI object located in an ordinary medium (e.g., vacuum), they tend to leave the object in the directions perpendicular to the surface. By then shaping the NZI object, one can create directive beams in the desired angles, even using isotopic sources as the main excitations.

Electromagnetic analyses of NZI structures naturally provide essential information for their designs [9, 10]. In fact, computational simulations of NZI structures were also considered in this column [11]. In SOLBOX-17, three-dimensional NZI structures were modeled as homogeneous objects with given permittivity and permeability values. As discussed in detail, even such homogeneous models may lead to computationally challenging problems, since using near-zero values for permittivity/permeability can easily make numerical systems unstable, resulting in inaccurate and/or inefficient solutions. In the simulations presented in SOLBOX-17, a novel surface formulation was used [9, 10], together with the Multilevel Fast Multipole Algorithm (MLFMA) [12] to handle large numbers of unknowns. It was shown that relatively simple lens geometries can be used to focus electromagnetic waves when materials of these geometries have small refractive indices.

In SOLBOX-17, the stability of simulations was demonstrated for extreme values of relative permittivity and permeability, i.e., as small as 0.001, thanks to the robust solver developed. From a computational point of view, this is necessary to reveal the limits of the solver used. In fact, even though homogeneous models are devised to represent realistic structures, there is no clear information (hence a stopping criterion for computational tools) on the achievable refractive index values in real-life practice. At the same time, as shown in the literature [4], quite small refractive indices (so the corresponding NZI capabilities) can be reached by using relatively simple arrangements of unit cells (e.g., dielectric rods), if geometric

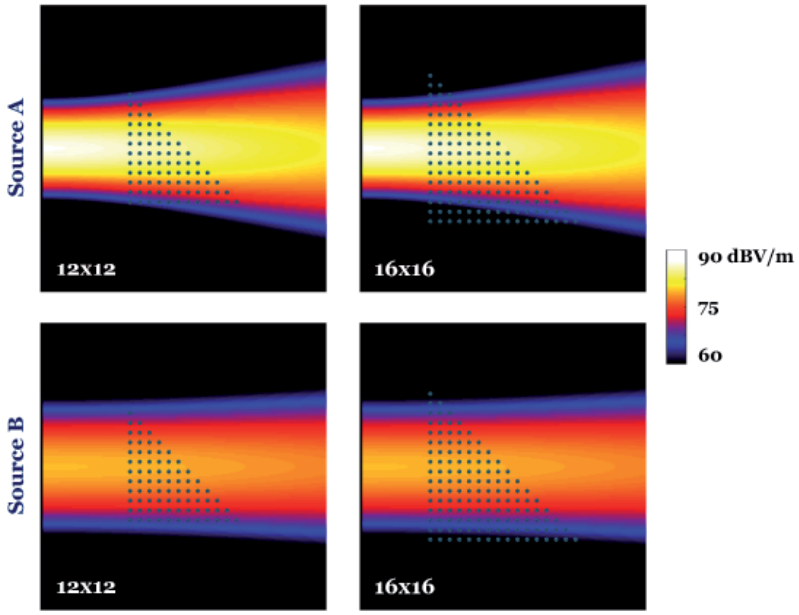

Figure 1. Dielectric rods arranged in 12×12 and 16×16 grids to create triangular prisms. Two complex-source-point beams (excitations) used in the simulations are also illustrated (without interacting with the rods).

and material properties are carefully selected. In this issue of SOLBOX, we consider computational solutions of such realistic structures that display NZI characteristics. Without homogenization, computational models do not involve extreme (and problematic) values of permittivity and permeability. However, this time relatively large numbers of unknowns in three-dimensional models bring new challenges in terms of the efficiency of simulations. In addition, strong electromagnetic interactions between unit cells make numerical systems rather ill-conditioned, leading to difficulties in iterative solutions.

Interested readers can send their solutions and results for similar problems to publish them in this column. The simulations presented in this issue were performed via a general-purpose state-of-the-art MLFMA solver. We believe that better (e.g., faster, more accurate, more visual) solutions could be achieved by using other solvers, particularly those developed for this kind of problem.

2. Problem SOLBOX-20

As shown in Figure 1, we considered arrays of dielectric cylindrical rods that were arranged in a way to create triangular prisms located in vacuum. Specifically, 78 and 136 identical rods were used in 12×12 and 16×16 grids, respectively, such that the overall structures could be used for the refraction of incoming waves, depending on the effective medium parameters induced by the rods. For the dimensions of the rods and their periodicity, as well as the materials to achieve NZI characteristics, we followed the designs in [4]. The radius of each cylinder was selected as 3.75 mm, while the center-to-center distance was set to 17 mm. If the rods were then made of alumina, an NZI behavior was expected to occur at around 10.3 GHz (when the relative permittivity of alumina was 8.8). Specifically, at this frequency, the prisms (made of rods) were expected to operate as epsilon-and-mu-near-zero (EMNZ) structures. Considering realistic simulations, the rods must have had finite lengths, while the selection seemed to be less restricted in comparison to other parameters. To suppress end effects that might deteriorate the performance of the prisms, we chose sufficiently long rods, i.e., 8.74 cm corresponding to 3λ, where λ is the wavelength in vacuum. We noted that with the given dimensions, 12×12 and 16×16 grids covered 19.45 cm×19.45 cm (approximately $6.7\lambda \times 6.7\lambda$) and 26.25 cm×26.25 cm (approximately $9\lambda \times 9\lambda$) areas, respectively. The prisms were hence relatively flat structures, with their shortest dimensions in the direction of the rods.

Alternative excitations could be used to demonstrate the NZI behaviors of the prisms described above. However, results with beam-type excitations may be more illustrative, particularly for clear observations of refracted waves, to identify effective medium parameters. In the sample results included in this issue, complex-source-point (CSP) excitations were used to generate beams that exactly satisfied Maxwell's equations. Two different beams were used, namely Source A and Source B, as also depicted in Figure 1, together with the prisms. Assuming that the grids were located on the *x*-*y* plane, the beams were positioned symmetrically in the *y* (vertical) and *z* (along the rods) axes, while they propagated in the *x* direction and illuminated the prisms from the left-hand side. We noted that a complex-source-point beam was obtained by placing a Hertzian dipole at a complex position, the imaginary part of which determined the shape (beam width and expansion rate) of the beam. As shown in Figure 1, Source A had a smaller beamwidth in comparison to Source B when they emerged,

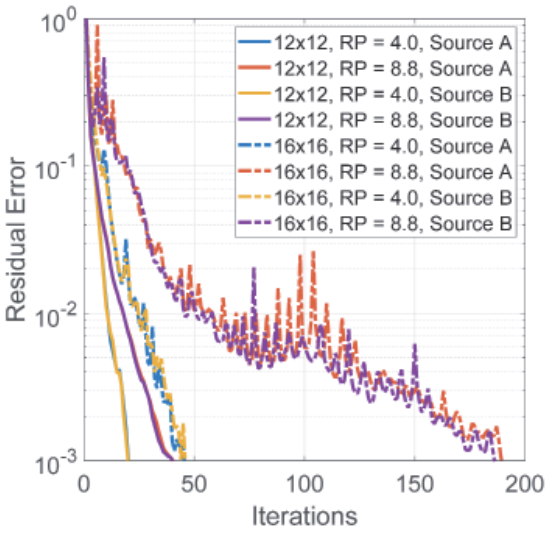

Figure 2. Iterative solutions of eight different problems involving triangular prisms made of dielectric rods.

while Source A expanded faster as propagation occurred. These sources hence interacted differently with the prisms, as illustrated in the sample results. In order to investigate the NZI characteristics of the prisms, electric/magnetic fields or power-density values could be computed at near-zone or far-zone locations. In both cases, extraction of effective refractive indices could demonstrate why these structures are so interesting, despite their simplicity.

3. Solution to Problem SOLBOX-20

3.1 Solution Summary

Solver type (e.g., Noncommercial, commercial): Noncommercial research-based code developed at CEMMETU, Ankara, Turkey

Solution core algorithm or method:
Frequency-domain MLFMA

Programming language or environment (if applicable):
MATLAB + MEX

Computer properties and resources used:
2.5 GHz Intel Xeon E5-2680v3 processors (using 16 cores)

Total time required to produce the results shown (categories: < 1 sec, < 10 sec, < 1 min, < 10 min, < 1 hour, < 10 hours, < 1 day, < 10 days, > 10 days):
< 10 hours per problem

3.2 Short Description of the Numerical Solutions

The triangular prisms with 12×12 and 16×16 grids described in SOLBOX-20 were solved in the frequency domain by using an efficient implementation of MLFMA [12]. The problems were formulated with the electric-magnetic current combined-field integral equation (JMCFIE) [13,14], and discretized by using the Rao-Wilton-Glisson functions on planar triangles. Expanding both electric and magnetic currents on surfaces, each rod was represented by 4464 unknowns. This led to 348,192 and 607,104 total numbers of unknowns, respectively, for the smaller (involving 78 rods) and larger (involving 136 rods) prisms. For efficient iterative solutions, multilayer preconditioning was used by employing a total of three layers with approximate forms of MLFMA [15]. In addition to the given value (8.8) for NZI characteristics, we tested the prisms when the relative permittivity of the rods was 4.0 at the same frequency (10.3 GHz). All electromagnetic interactions between discretization elements were computed with a maximum 1% error. Once the current coefficients were found, electric-field intensity, magnetic-field intensity, and power-density values were computed at various near-

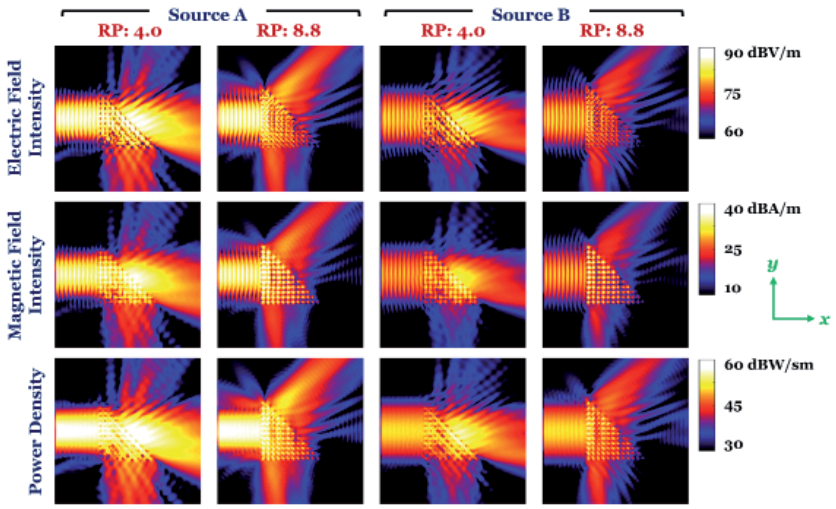

Figure 3. The near-zone electric-field intensity, magnetic-field intensity, and power-density distributions for the smaller prism structure (12×12 grid) when the relative permittivities of the rods were 4.0 and 8.8. The results are shown for both Source A and Source B, illustrated in Figure 1.

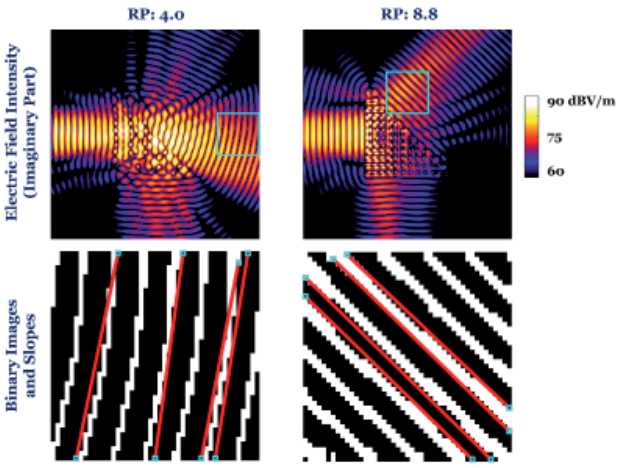

Figure 4. An investigation of the imaginary part of the electric-field intensity for the smaller prism structure (12×12 grid) when the relative permittivity of the rods was 4.0 (left) and 8.8 (right). Only Source A was considered for the excitation.

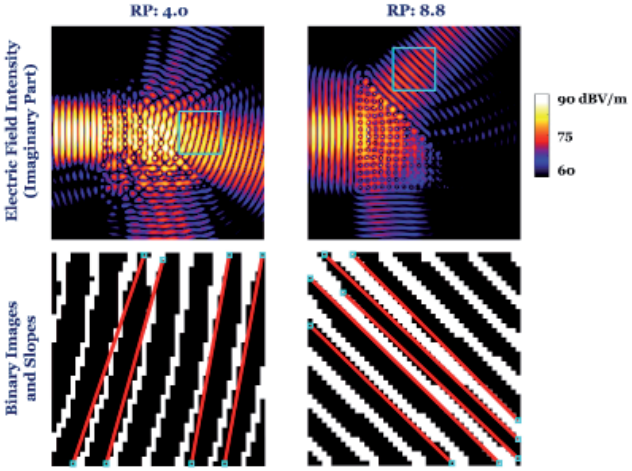

Figure 6. An investigation of the imaginary part of the electric-field intensity for the larger prism structure (16×16 grid) when the relative permittivity of the rods was 4.0 (left) and 8.8 (right). Only Source A was considered for the excitation.

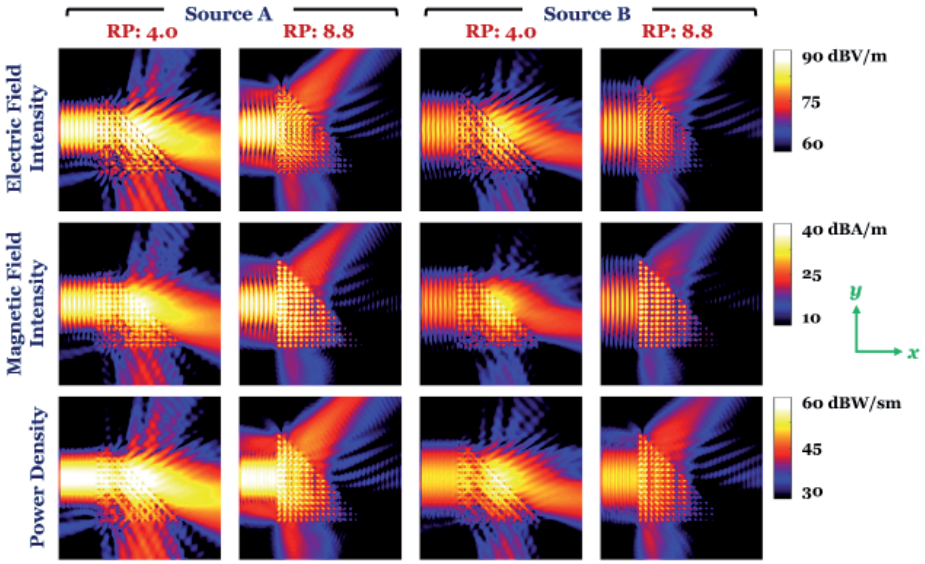

Figure 5. The near-zone electric-field intensity, magnetic-field intensity, and power-density distributions for the larger prism structure (16×16 grid) when the relative permittivity of the rods was 4.0 and 8.8. The results are shown for both Source A and Source B, illustrated in Figure 1.

zone locations in the vicinity of the prisms, as well as in far-zone directions to visualize beams. The near-zone electric-field intensity distributions were further used to extract effective refractive-index values. For this purpose, edge detection and the Hough line transform were applied, as described below.

3.3 Results

Considering two prisms (12×12 and 16×16 grids), two relative permittivity values (8.8 and 4.0), and two sources (Source A and Source B), a total of eight different MLFMA solutions were performed. Iterative convergence histories for these solutions are depicted in Figure 2. In each result, the residual error for the main solver (employing full MLFMA) was plotted with respect to FGMRES iterations. We observed that solutions became more challenging when (i) permittivity increased and (ii) the problem got larger, whereas the type of the source had little effect on the iterative convergence. As indicated in Section 3.1, each solution took less than 10 hours using 16 cores, but this limit was particularly due to the most-challenging problems (the larger prisms involving rods with 8.8 relative permittivity).

Figure 3 presents the near-zone electric-field intensity, magnetic-field intensity, and power-density distributions

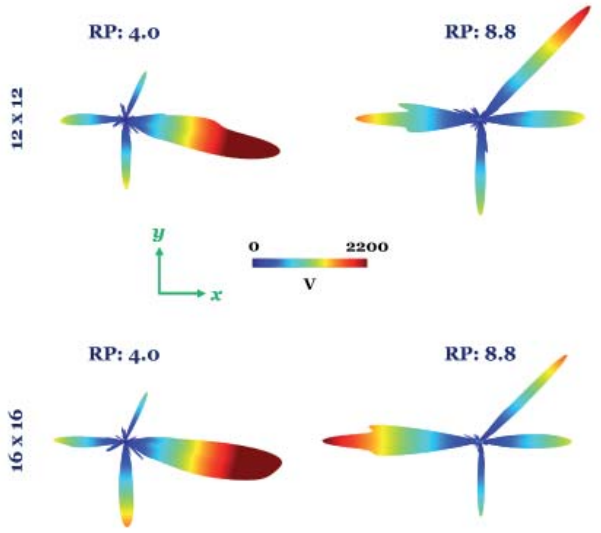

Figure 7. The far-zone electric-field intensity obtained when different prisms were excited via Source A, shown in Figure 1.

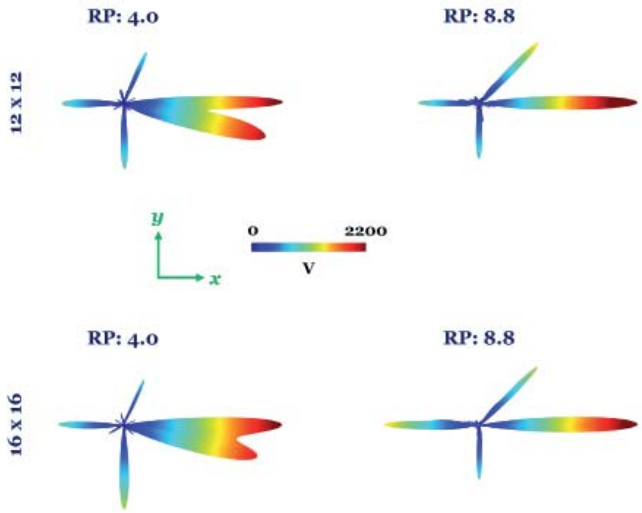

Figure 8. The far-zone electric-field intensity obtained when different prisms were excited via Source B, shown in Figure 1.

obtained for the smaller prism structure (12×12 grid). We observed that the distributions were different for Source A and Source B. However, the main characteristics directly depended on the permittivity of the rods. Specifically, when the relative permittivity was 8.8, we clearly observed the NZI behavior of the prism. After the beam entered the prism, it left in two main directions, both of which were perpendicular to the hypothetical (oblique and bottom) surfaces. The oscillatory patterns on the left-hand side of the prism indicated that there were also reflected waves, which may have been caused by direct (from the left surface) and secondary (from the internal surfaces) reflections. On the other hand, when the relative permittivity was 4.0, we observed quite an ordinary behavior. In addition to scattered waves towards many directions, a main beam occurred in a downward direction, i.e., as expected when a wave passes from a high-index region to a low-index region.

To further analyze and compare the behaviors of the prisms with different material properties, we focused on the imaginary part of the electric-field intensity in Figure 4. Specifically, we studied the oscillation patterns of the waves, while the same practice could be made with the real part of the electric-field intensity, as well as with the real/imaginary parts of the magnetic-field intensity. First, as shown in each color plot in Figure 4, a frame was automatically located on the output side based on the consistency of the consecutive peaks with the wavelength. The values inside the frame were then converted into a binary image. This allowed us to employ the Hough line transform for line fitting. Finally, the slopes of the generated lines provided reliable information on the direction of the wave. Using this procedure, we computed the effective refractive indices as 1.15 and -0.02, respectively, when the relative permittivity of the rods was 4.0 and 8.8. Consequently, in addition to the interpretation of the visual data, we quantitatively verified the NZI behavior of the structure with 8.8 relative permittivity.

Figures 5 and 6 present the results for the larger prism structure using a 16×16 grid. We observed that the near-zone distributions in Figure 5 were similar to those in Figure 3 (for the smaller prism structure), while many visible differences existed due to the increased number of rods. The imaginary part of the electric-field intensity was focused in Figure 6, where binary images and Hough lines were again displayed inside the selected regions. Considering the slopes, the effective refractive indices were calculated as 1.21 and -0.02, respectively, when the relative permittivities of the rods were 4.0 and 8.8. The results were hence consistent with those obtained for the smaller prism structure, and we verified the NZI characteristics of the prism when the material was selected as required.

We finally investigated the far-zone radiation patterns, as depicted in Figures 7 and 8, when the prisms were excited via Source A and Source B, respectively. These patterns included contributions of both excitations (complex-source-point beams) and scattered (secondary) fields, similar to the near-zone plots detailed above. Considering the results for Source A (Figure 7), we observed four major beams for both smaller and larger prism structures, whether the relative permittivity of the rods was 4.0 or 8.8. When the relative permittivity was 4.0 (for both 12×12 and 16×16 grids), the main lobe occurred in accordance with an ordinary refraction, while three other beams were created due to reflections. However, when the relative permittivity was 8.8, a large beam was generated perpendicular to the oblique surface of the prism (whether it was 12×12 or 16×16) as a result of its NZI behavior. We also noted that these patterns of NZI prisms involved forward-directed beams due to portions of incoming waves that did not interact with the prisms, as well as larger back-directed beams. NZI prisms were expected to demonstrate epsilon-and-mu-near-zero behavior (when made of dielectric rods), while their effective intrinsic impedances were not

considered in these simulations. Hence, investigation of the reflected waves may provide further information about possible differences between the effective permittivity and the effective permeability, which cause mismatches with vacuum. Considering the results obtained for Source B, we observed that the forward-directed beams were also visible for the ordinary cases, while they were even stronger for the NZI structures. Using larger prisms would possibly reduce these beams. However, the results still demonstrated the NZI characteristics of the prisms with rods having 8.8 relative permittivity, in contrast to the ordinary characteristics when the relative permittivity was 4.0.

4. References

1. R. W. Ziolkowski, "Propagation In and Scattering From a Matched Metamaterial Having a Zero Index of Refraction," *Phys. Rev. E*, **70**, October 2004, 046608.

2. M. Silveirinha and N. Engheta, "Tunneling of Electromagnetic Energy Through Subwavelength Channels and Bends Using ε -Near-Zero Materials," *Phys. Rev. B*, **97**, October 2006, 157403.

3. B. Edwards, A. Alu, M. E. Young, M. Silveirinha, and N. Engheta, "Experimental Verification of Epsilon-Near-Zero Metamaterial Coupling and Energy Squeezing Using a Microwave Waveguide," *Phys. Rev. Lett.*, **100**, January 2008, 033903.

4. X. Huang, Y. Lai, Z. H. Hang, H. Zheng, C. T. Chan, "Dirac Cones Induced by Accidental Degeneracy in Photonic Crystals and Zero-Refractive-Index Materials," *Nat. Mat.*, **10**, May 2011, pp. 582-586.

5. J. Luo and Y. Lai, "Anisotropic Zero-Index Waveguide with Arbitrary Shapes," *Sci. Rep.*, **4**, July 2014, 5875.

6. V. Pacheco-Pena, V. Torres, M. Beruete, M. Navarro-Cia, and N. Engheta, "ε -near-zero (ENZ) Graded Index Quasi-Optical Devices: Steering and Splitting Millimeter Waves," *J. Opt.*, **16**, September 2014, 094009.

7. X.-T. He, Z.-Z. Huang, M.-L. Chang, S.-Z. Xu, F.-L. Zhao, S.-Z. Deng, J.-C. She, J.-W. Dong, "Realization of Zero-Refractive-Index Lens with Ultralow Spherical Aberration," *ACS Photonics*, **3**, November 2016, pp. 2262-2267.

8. I. Liberal and N. Engheta, "Near-Zero Refractive Index Photonics," *Nat. Photon.*, **11**, March 2017, pp. 149-158.

9. B. Karaosmanoğlu, U. Özmü, and Ö. Ergül, "Novel SIE Formulations for Accurate and Stable Analysis of Near-Zero-Index Materials," Proceedings of the IEEE International Symposium on Antennas and Propagation, 2019.

10. H. İbili, Y. Koyaz, U. Özmü, B. Karaosmanoğlu, and Ö. Ergül, "Novel SIE Implementations for Efficient and Accurate Electromagnetic Simulations of Zero-Index Materials," Proceedings of Progress in Electromagnetics Research Symposium (PIERS), 2019.

11. H. İbiliand and Ö. Ergül, "SOLBOX-17: Cylindrical Lens Structures," *URSI Radio Science Bulletin*, No. 370, September 2019, pp. 58-64.

12. Ö. Ergül and L. Gürel, *The Multilevel Fast Multipole Algorithm (MLFMA) for Solving Large-Scale Computational Electromagnetics Problems*, New York, Wiley-IEEE, 2014.

13. P. Ylä-Oijala and M. Taskinen, "Application of Combined Field Integral Equation for Electromagnetic Scattering by Dielectric and Composite Objects," *IEEE Trans. Antennas Propagat.*, **53**, 3, March 2005, pp. 1168-1173.

14. Ö. Ergül and L. Gürel, "Comparison of Integral-Equation Formulations for the Fast and Accurate Solution of Scattering Problems Involving Dielectric Objects with the Multilevel Fast Multipole Algorithm," *IEEE Trans. Antennas Propagat.*, **57**, 1, January 2009, pp. 176-187.

15. C. Önol, A. Üçüncü, and Ö. Ergül, "Efficient Multilayer Iterative Solutions of Electromagnetic Problems Using Approximate Forms of the Multilevel Fast Multipole Algorithm," *IEEE Antennas Wireless Propag. Lett.*, **16**, 2017, pp. 3253-3256.

Why join us for EuCAP 2022

- **After the last EuCAP2020 and EuCAP2021 virtual events**, we are eager to meet and share. We will make this come back to a physical meeting exceptional!
- **For the high technical-scientific** conference level supported by strong regional industries and universities
- **For the venue:** Its avant-garde design has given it great versatility, with the technology and services needed for our congress.
- **For the city:** Madrid, extraordinary cultural wealth and green spaces, great facilities and accessible from Europe, America and Africa with excellent connections by air to the main cities of the world.
  - » **200 direct flight** destinations
  - » **15–20 min.** between airport, city centre and conference venue by public transport

Important dates

Call for papers:

Call:	July 2nd 2021
Deadline:	October 15th 2021 (fixed deadline). Several reminders.
Notification:	December 21st 2021

General information

Technical Secretariat

GRUPO PACÍFICO
Eucap2022@pacifico-meetings.com

Website

www.eucap2022.org

Venue

IFEMA-Feria de Madrid. Palacio Municipal de Congresos

Address

Av. Capital de España, 7, 28042 - Madrid

Randy L. Haupt
Colorado School of Mines
Brown Building 249
1510 Illinois Street, Golden, CO 80401 USA
Tel: +1 (303) 273 3721
E-mail: rhaupt@mines.edu

Amy J. Shockley
E-mail: aj4317@gmail.com

Silver Lining

The term "silver lining" originated from the 1634 poem "Comus" by John Milton. It describes the glistening edges of a cloud that blocks the sun. We use it when emphasizing the positive aspects of a very negative situation.

In 1979, I underwent military parachute training (covered in previous Ethically Speaking columns) and three weeks of survival training. I lost 7 kg while navigating with a compass between designated points in the Colorado mountains, and simultaneously evading people with guns. I slept under the stars and had very little food to eat. One night while sleeping, I was captured and taken to a prisoner-of-war camp, where I endured some "light" torture for about three days before they released me. On the last day of the training, I met a friend who was also in the program, and we walked together to our final pick-up point before heading home for leave. On the way, we found a huge patch of wild strawberries, and sat there scarfing down the berries and looking out at the mountains. That was our silver lining. While I will never forget the intensity of what I endured in that training, there was a silver lining – and I will always remember it.

Of course, right now, our very negative situation is the pandemic. Almost everyone's day-to-day life dramatically changed over the past year, with new remote-working requirements (or for many, job loss), and limited activities available during free times. It was easy to feel grief over the loss of normalcy. However, is there a silver lining during a pandemic? In the midst of the current health, political, and economic climate, we have witnessed people having more family meals, keeping in better contact with long-distance friends, and picking up new/old hobbies. As Rahm Emanuel said, "You never want a serious crisis to go to waste. It provides the opportunity to do things that were not possible to do before." While Emanuel was referring to policy making, it is a good adage to reframe your perspective on seemingly dire situations.

Dwelling on the negatives that are beyond our control (and there are a lot) results in a downward spiral of the human spirit. One can get off of that spiral by identifying aspects of the scenario that can be controlled and take actions towards improvement. It's incredibly empowering. For instance, public-health orders that closed office buildings have dramatically reduced commuting: saving time, money, and pollution. A more serious situation arises when a loved one contracts the disease. We may not be able to hug them or provide direct care/treatment, but we still can call and send cards, letters, e-mails, pictures, etc., to let them know of our love and support. By taking a step back from the larger, uncontrollable event, and identifying opportunities within your control, you can create your own silver lining.

When faced with a crisis, it is important to acknowledge the scope and outcomes in order to understand how it will impact you. After that, categorize new things in the environment as "Controllable" or "Uncontrollable," based on your ability to directly change the outcomes. Acknowledging the uncontrollable aspects of a situation helps isolate the controllable parts. Focusing your time and energy to influence the controllable aspects makes the best out of a bad situation, potentially even identifying new opportunities to exploit.

Several controllable items include relationships, personal health, finances, education, work performance,

community outreach, etc. While the pandemic is bad – very bad – several silver linings we have witnessed include:

1. Higher adoption of technology, largely eliminating locational barriers that previously existed, and creating additional opportunities for multi-tasking;
2. More time spent at home, allowing for increased family connections and/or more opportunities to finish home-improvement projects;
3. Less money spent on restaurants, events, and traveling, softening financial impacts from job loss/pay reductions, and potentially increasing savings or reducing debt;
4. Increased control over the extent of your interactions, allowing you to reduce your exposure to difficult people and increase your time spent with those you enjoy;
5. Reduced or eliminated commutes, creating more free time and lower stress levels;
6. The ability to wear more-comfortable clothes.

In *Zen and the Art of Motorcycle Maintenance* (1974), Robert M. Pirsig wrote,

> Trials never end, of course. Unhappiness and misfortune are bound to occur as long as people live, but there is a feeling now, that was not here before, and is not just on the surface of things, but penetrates all the way through: We've won it. It's going to get better now. You can sort of tell these things.

As we are getting close to turning the corner of this truly awful event, we hope that you take advantage of the items within your control and find the silver lining. You may be surprised in looking back at this time how the silver lining produced some new and positive innovations in our society and your life.

Historical Corner Column

Giuseppe Pelosi
Department of Information Engineering
University of Florence
Via di S. Marta, 3, 50139 Florence, Italy
E-mail: giuseppe.pelosi@unifi.it

Foreword

Much has been written about Heinrich Hertz and Guglielmo Marconi. In particular, two recent papers appeared in the *IEEE Antennas and Propagation Magazine* (G. Smith, **58**, 5, 2016, pp. 98-108; and T. Simpson, **60**, 4, 2018, pp. 132-140). These thoughtfully analyzed Hertz's apparatus. With such an apparatus, Hertz, within his laboratory walls in 1888, gave experimental evidence of the existence of the electromagnetic waves predicted by James Clerk Maxwell in his *Dynamical Theory of the Electromagnetic Field*, presented in 1864.

A few years later, in 1895, with his apparatus Marconi managed to build a successful radio link outdoors, over a distance exceeding 2 km, beginning a race to attain greater and greater distances. This race eventually brought him in 1901 to connect the two shores of the Atlantic Ocean, from Poldhu in Cornwall to Signal Hill, Newfoundland, in Canada (Figure 1). In this feat, which opened the route to worldwide radio communication, he was helped by the ionosphere, the existence of which he, as anyone else, was not yet aware (see among others, P. Mazzinghi and G. Pelosi, "Enrico Fermi Talks About Guglielmo Marconi," *IEEE Antennas and Propagation Magazine*, **53**, 3, June 2011, pp. 226-230).

In the contribution that follows, the apparatus used by Hertz and Marconi are analyzed to compare them in terms of frequency actually used and power effectively radiated. This shows how Marconi was successful in gaining such longer ranges.

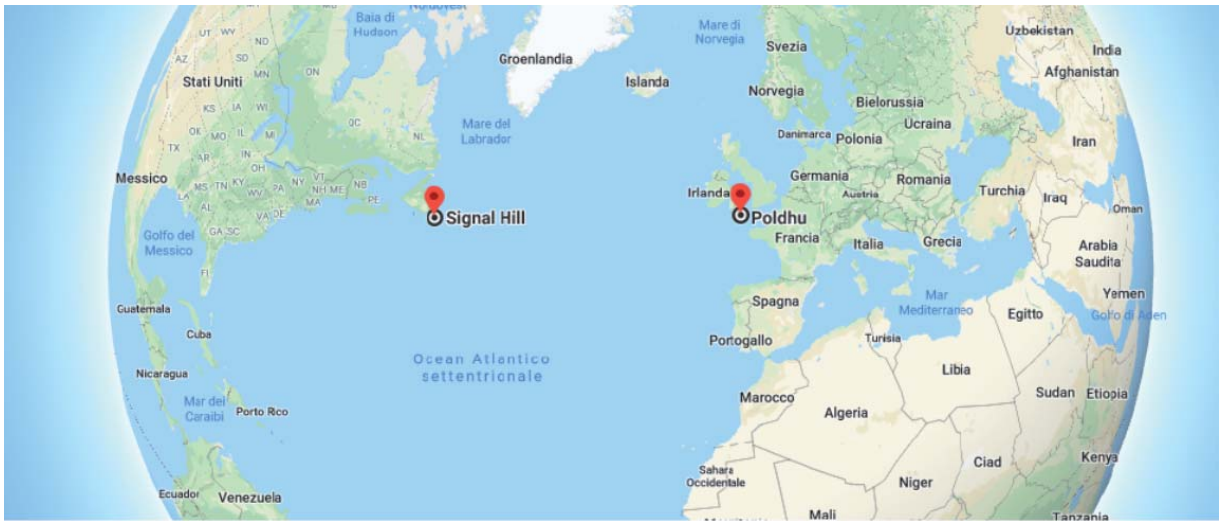

Figure 1. A map showing the endpoints of Marconi's 1901 Atlantic Ocean transmission, from Poldhu in Cornwall, England, to Signal Hill, Newfoundland, Canada.

Hertz and Marconi: A Comparison Between The Apparatus of Their Landmark Experiments

Stefano Maddio and Stefano Selleri

Department of Information Engineering
University of Florence
Via di S. Marta, 3, I-50139, Florence, Italy
E-mail: [stefano.maddio,stefano.selleri]@unifi.it

We all know that Heinrich Hertz [Hamburg, Germany, 1857 – Bonn, Germany, 1894] (Figure 1a) first proved the existence of electromagnetic waves in his laboratory. His spark-based experiments [1, 2] demonstrated not only the existence of waves by showing that the transmitter in the proximity of a conducting wall generated nodes and antinodes that were compatible only with wave propagation [3], but also confirmed the theoretical prediction by James Clerk Maxwell [Edinburgh, Scotland, 1831 – Cambridge, England, 1879] that the speed of such waves was equal to the speed of light [2, 4]. On the other hand, the phenomenon remained limited to his laboratory and, even if replicated, remained confined to scientific demonstrations or little more up to 1895. It was at that point that Guglielmo Marconi [Bologna, Italy, 1874 □ Rome, Italy, 1937](Figure 1b) managed to have his receiver buzz well over a mile away from the transmitter, and behind a hill [5, 6].

Both of these events deserved an IEEE Milestone:

- "First Generation and Experimental Proof of Electromagnetic Waves, 1886-1888" was dedicated in Karlsruhe, Germany, on December 5, 2014;
- "Marconi's Early Experiments in Wireless Telegraphy, 1895" was dedicated in Pontecchio Marconi, Bologna, Italy, on April 29, 2011.

It ought to be said that Marconi's priority in achieving long-range transmissions were contested by Nikola Tesla [Smiljan, Croatia, 1856 – New York, USA, 1943] in the USA, who claimed beginning similar experiments in 1891 [7] and claimed a successful 30-mile link "prior than 1897." It is also fairly well known that Aleksander Popov [Krasnoturinsk, Russia, 1859 – San Petersburg, Russia, 1906] obtained successful communications on March 26, 1896, seven days after Marconi's filing for his first patent in England [8]. The location of Marconi's first experiments has also been a matter of discussion [6, 9].

It is an interesting matter to understand the differences in the two devices used by Hertz and Marconi: the advancements done in those eight years that allowed the second person to bring human-generated electromagnetic waves out of a laboratory and into an enterprise that would change the world.

Figure 1a. Heinrich Rudolf Hertz [Hamburg, Germany, February 22, 1857 – Bonn, Germany, January 1, 1894].

Figure 1b. Guglielmo Giovanni Maria Marconi [Bologna, Italy, April 25, 1874 – Rome, July 20, 1937].

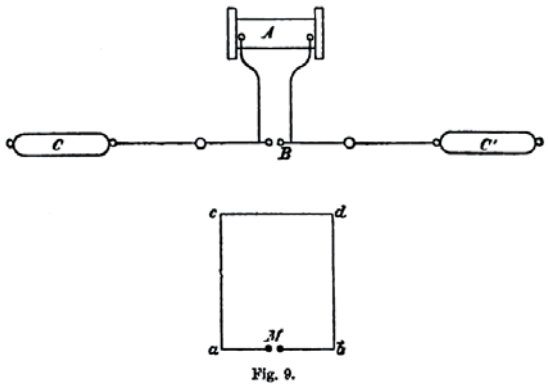

Figure 2a. A schematic of Hertz's apparatus [1].

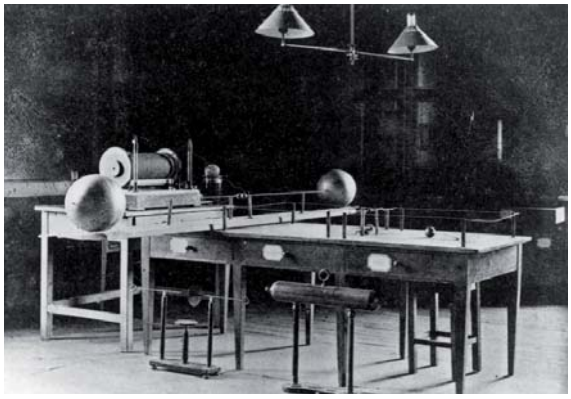

Figure 2b. A photo of Hertz's laboratory, with an apparatus such as that used in 1888 (photo made in 1901 by A. Schleiermacher [1857-1953], Hertz's assistant).

1. Hertz's Apparatus and Indoor Experiment

Hertz's experiment has been revisited very competently in a couple of recent papers [3, 10], so we will briefly recall it here. Hertz's apparatus is shown in Figure 2.

As pointed out in [1, 3, 10], the two large spheres (30 cm in diameter) placed 1 m apart formed a capacitor, while the rod connecting them, 5 mm in diameter, formed an inductance. The spark gap was defined by two spheres 3 cm in diameter. Some quick computations lead to the following estimates [10, 11]:

$$C = 9.82\,\text{pF},$$

$$L = 746\,\text{nH},$$

and hence a resonant frequency of $f = 58.77$ MHz, and a wavelength of $\lambda = 5.10$ m.

We are not aware of the voltage provided by the Rhumkorff coil, but we can assume 5 kV for the sake of comparison for both apparatus: Hertz's and Marconi's. Furthermore, we shall assume 100 Hz as the frequency of repetition of the sparks, that is, the capacitors were charged 100 times per second. Oscillations at 58.77 MHz excited by each single charge/discharge were completely damped due to radiation and losses before the next charge/discharge.

Figure 3a. The Celestini hill, as seen from the window of Marconi's laboratory at villa Griffone, looking towards the receiver location. In the foreground is the structure holding the IEEE Milestones (courtesy of Marconi Foundation).

Figure 3b. A map with the positions of the transmitter, the receiver, and the hill in between (courtesy of Marconi Foundation).

Figure 3c. The Celestini hill, seen from the receiver location, looking towards the transmitter at Villa Griffone (completely hidden by the trees) (courtesy of Marconi Foundation).

For this voltage, the capacitor stored 122.5 μJ at each charge. In continuous operation, the power was hence the energy of the 100 charges happening in one second, ideally $P = 12.25$ mW. In practice, part of this power was dissipated in the conductor and not radiated. We might safely assume that only half of this power was actually radiated, or about 6 mW.

Of these few milliwatts, a large part must have been collected to allow visible sparks in the receiver, hence Hertz and others duplicating these results could never put too much distance between the transmitter and receiver.

2. Marconi's Apparatus and Outdoor Experiment

Marconi's initial experiments were basically similar to Hertz's, but in 1895 Marconi soon shifted to outdoor experiments. There, the radiating conductors were vertical and halved, that is, just one vertical wire, the other end being grounded. He also worked with longer and longer wires, loaded at the higher end with plates or metallic cubes. The breakthrough experiment, with the receiver more than one mile away and behind the celebrated "Celestini hill" (Figure 3), used a 8 m high pole, with four metallic cubes of 1 m edges connected at the higher end, the transmitter still being based on a Rhumkorff coil and a spark gap [12] (Figure 4).

What was completely different was the receiver, which was somewhat "active," even if not in our modern sense of being capable of amplification. It contained a battery providing the energy to ring a bell once the radio-frequency signal caused the shortening of a peculiar and sensitive device named a coherer.

Here, the evaluation of the working frequency was more difficult, due to the odd antenna (Figure 4). We can approximate the four cubes, 1 m on a side, with a surface of 6 m^2 each, as four spheres of equal area, that is, a radius

Figure 4a. A reconstruction of Marconi's 1895 antenna in the garden of Villa Griffone, Marconi's house (courtesy of Marconi Foundation).

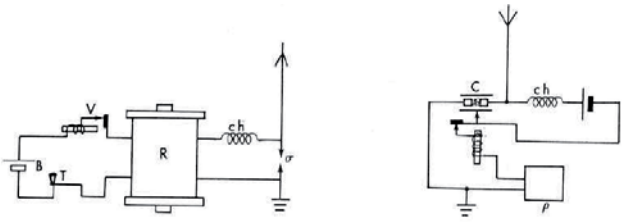

Figure 4b. Schematics of Marconi's transmitter and receiver, from [12].

of 70 cm, placed 8 m above a perfectly conducting ground, hence 16 m from their image according to the image theorem. By applying the same formula as above [11] to each pair, and considering the four pairs in parallel, one obtains

$$C = 162.9 \text{ pF}.$$

On the other hand, the 8 m wire inductance, assuming 1 mm diameter, gives

$$L = 15.0 \text{ μH},$$

which yields $f = 3.22$ MHz and a wavelength of $\lambda = 93.1$ m. Hence, in this case, the 8 m wire was indeed short.

Again, let us assume for comparison the same 5 kV and 100 Hz for the excitation. In this case, the capacitor stored 2.03 mJ, for an ideal power of $P = 203$ mW and possibly ideally 0.1 W radiated.

Absolute numbers are not really meaningful, due top the unconfirmed hypotheses of 5 kV and 100 sparks per second, but the relative values are important. Marconi managed to radiate about twenty times the power radiated

by Hertz, but, as already mentioned, this would not have been enough.

In 1884, Temistocle Calzecchi-Onesti [Lapedona, Italy, 1853 – Monterubbiano, Italy, 1920] observed a drastic reduction of resistivity in a tube filled with iron filings when a circuit with an inductor was opened and closed [13]. In 1890, Édouard Branly [Amiens, France, 1844 – Paris, France, 1940] studied the same phenomenon, independently and unaware of [13], and observed that the device switched to conductivity if a spark was generated, even at a distance. In 1894, Oliver Lodge [Penkhull, England, 1851 – Wilsford, England, 1940] repeated Hertz's experiments by using such a device, which he named a coherer, and which proved to be a much more sensitive detector than the wire loop used by Hertz. Branly and Lodge focused their research on the mechanisms of powder conductivity, neglecting the practical applications, which were, on the other hand, crystal clear in Marconi's mind.

According to Lodge, the grains became dipoles and were mutually attracted, forming conductive chains. Branly did not believe this was the mechanism, and indeed showed that grain motion was not behind the phenomenon, since particles embedded in wax or resin still behaved the same way, and indeed a column of six steel balls a few centimeters in diameter also did. However, the invention of the diode and the triode early in the XXth century made the coherer obsolete, and stopped further research. Indeed, the mechanism behind the coherer is still not fully understood [14].

However, it was in bringing this approach to the extreme, with higher vertical antennas and more and more powerful spark-based transmitters that Marconi managed to cross the Atlantic in 1901.

3. Acknowledgments

The authors wish to express their gratitude to Barbara Valotti, Curator of Marconi Museum at the Marconi Foundation, Villa Griffone, Pontecchio Marconi, Bologna, Italy, for permission to reproduce some of the images in this article.

4. References

1. H. Hertz, *Electric Waves* (English translation by D. E. Jones), New York, New York, Macmillan, 1893.

2. H. Hertz, "Ueber electrodynamische wellen im luftraume und deren reflexion [About Electrodynamic Waves in the Space and Their Reflection]," *Annalen der Physik und Chemie*, **34**, 8(a), 1888, pp. 609-623.

3. G. Smith, "An Analysis of Hertz's Experimentum Crucis on Electromagnetic Waves," *IEEE Antennas Propagation Magazine*, **58**, 5, October 2016, pp. 98-108.

4. S. Maddio and S. Selleri, "Ernst Lecher and His Wires," *URSI Radio Science Bulletin*, No. 369, 2019, pp. 10-17.

5. G. Falciasecca, "Marconi's Early Experiments in Wireless Telegraphy, 1895," *IEEE Antennas Propagation Magazine*, **52**, 6, December 2010, pp. 220-221.

6. M. Fabbri and G. Pelosi, "Guglielmo Marconi: Some New Documents Covering the Years 1894-1896," *IEEE Antennas Propagation Magazine*, **55**, 2, April 2013, pp. 291-302.

7. L. I. Anderson (ed.) *Nikola Tesla on His Work with Alternating Currents*, Breckenbridge, Colorado, Twenty First Century Books, 2002, Chapter IV.

8. M. Radovsky, *Alexander Popov Inventor of Radio*, Honolulu, Hawaii, University Press of the Pacific, 2001.

9. G. Pelosi and S. Selleri, "Recent Outcomes of the Investigations on Guglielmo Marconi's Supposed Experiments in Switzerland," HISTELCON 2019, Glasgow, Scotland, 18-19 September 2019, pp. 11-13.

10. T. Simpson, "Revisiting Heinrich Hertz's 1888 Laboratory," *IEEE Antennas and Propagation Magazine*, **60**, 4, August 2018, pp. 132-140.

11. W. R. Smythe, *Static and Dynamic Electricity, Third Edition*, Milton Park, England, Taylor & Francis, 1989.

12. G. Marconi, *Scritti di Guglielmo Marconi* [*Guglielmo Marconi's Writings*], Rome, Italy, Reale Accademia d'Italia, 1941.

13. T. Calzecchi-Onesti, "Sulla conduttività elettrica delle limature metalliche [On the electrical conductivity in metallic powders]," *Nuovo Cimento*, **16**, 1884, pp. 58-64.

14. E. Falcona and B. Castaing, "Electrical Conductivity in Granular Media and Branly's Coherer: A Simple Experiment," *American Journal of Physics*, **73**, 4, 2005, pp. 302-306.

History of Ionospheric Physics

Kristian Schlegel, past President of URSI, asked that the following open-access article on the history of ionospheric physics be brought to the attention of *Radio Science Bulletin* readers: A. Anduaga, "The Formation of Ionospheric Physics – Confluence of Traditions and Threads of Continuity," *History of Geo- and Space Sciences*, **12**, 1, 2021, pp. 57-75; available at https://doi.org/10.5194/hgss-12-57-2021. The following is the abstract from the article:

This paper examines how ionospheric physics emerged as a research speciality in Britain, Germany, and the United States in the first four decades of the 20th century. It argues that the formation of this discipline can be viewed as the confluence of four deep-rooted traditions in which scientists and engineers transformed, from within, research areas connected to radio wave propagation and geomagnetism. These traditions include Cambridge school's mathematical physics, Göttingen's mathematical physics, laboratory-based experimental physics, and Humboldtian-style terrestrial physics. Although focused on ionospheric physics, the paper pursues the idea that a dynamic conception of scientific tradition will provide a new perspective for the study of geoscience history.

James C. Lin
University of Illinois at Chicago
851 South Morgan Street, M/C 154
Chicago, IL 60607-7053 USA
E-mail: lin@uic.edu

Sonic Health Attacks on Havana-Based Diplomats Using Pulsed Microwaves

As I write this article, the US National Academies of Sciences, Engineering, and Medicine (NASEM) have just released their study report on "An Assessment of Illness in U.S. Government Employees and Their Families at Overseas Embassies" [1]. It has been about three years since the publication of my article describing the mystery of sonic health attacks on Havana-based diplomats [2]. It was first hypothesized in this paper, assuming that the reported events were reliable, that there was actually a scientific explanation for the source of sonic energy. It could well have been "from a targeted beam of high-power microwave pulse radiation."

In examining plausible causes of the described illnesses, the NASEM report [1] pronounced that among the mechanisms the study committee considered, "directed, pulsed radio frequency (microwave) energy appears to be the most plausible mechanism" in explaining these cases, especially in individuals with the distinct early symptoms.

The hypothesis of a microwave auditory effect [2] was based on years of published laboratory and theoretical research. A minuscule but rapid (~μs) rise in tissue temperature (on the order of a micro degree), resulting from the absorption of pulsed microwave energy, creates a thermoelastic expansion of brain matter. This small theoretical temperature elevation is hardly detectable by any currently available temperature sensors, let alone felt as a thermal sensation or heat. Nevertheless, it can launch an acoustic wave of pressure that travels inside the head to the inner ear. There, it activates the hair-cell nerves in the cochlea, which then relay it to the central auditory system for perception, via the same process involved in normal sound hearing [3-6].

Depending on the power of the impinging microwave pulses, the level of induced sound pressure could be considerably above the threshold of auditory perception at the cochlea: approaching or exceeding levels of discomfort (including the reported headaches, ringing in the ears, nausea, and problems with balance or vertigo), and even causing potential brain-tissue injury.

It is important to note that in recent clinical radiological examinations, compared to individuals not experiencing the loud bursts of sound, brain magnetic resonance imaging (MRI) revealed significant differences in whole-brain white-matter volume, regional gray- and white-matter volumes, cerebellar tissue microstructural integrity, and functional connectivity in the auditory and visuospatial subnetworks, but not in the executive control subnetwork [7]. However, the clinical importance of these differences is not definitive. Nevertheless, a high-power microwave-pulse-generated acoustic pressure wave can be initiated in the brain and then reverberate inside the head, and potentially reinforce the initial pressure to cause injury of brain matters [6].

While the clinical symptoms presented are concussion-like, the MRI images did not resemble usual presentations of traumatic brain injury or concussion. However, clinical experiences with concussion are mostly derived from externally inflicted impact injuries, such as a hit to the head against the ground or other rigid bodies, which may set brain tissues into violent motion against the skull. A high-

Table 1. Thresholds of microwave induced auditory sensation in adult humans with normal hearing determined in controlled laboratory studies.

Frequency (MHz)	Pulse Width (μs)	Peak Power Density (kW/m^2)	Ambient Noise Level (dB)	Reference
1245	10 - 70	0.9 - 6.3	45*	[8]
2450	1 - 32	12.5 - 400	45	[9, 10]
3000	10 - 15	2.25 - 20	45**	[11]
Pulse Width Between 10 μs and 32 μs				
1245	10 - 30	2.1 - 6.3	45*	[8]
2450	10 - 32	12.5 - 40	45	[9,10]
3000	10 - 15	2.25 - 20	45**	[11]

*Typical sound pressure level for microwave anechoic chambers lined with absorbing materials;
** With plastic foam earmuffs.

power microwave-pulse-generated acoustic pressure wave could be initiated in the brain and then reverberate inside the head (see results of computer simulations in [6]), and potentially reinforce the initial pressure to cause injury of brain matters. It is thus conceivable that the MRI images from high-power microwave-pulse-induced pressure or shock waves may have entirely different manifestations of the brain injury or concussion. The clinical importance of these differences is uncertain at present, and may demand future study for clarification.

The known near-zone thresholds determined under controlled laboratory conditions for peak microwave power density of auditory perception in human subjects with normal hearing are given in Table 1. Note that while there were wide variations in measured threshold values over the range of 1 μs to 70 μs of pulse widths involved, the subset of data for 10 μs to 32 μs fell within a narrower range. Considering that the ambient noise levels in all three experiments were essentially the same, it may be reasonable to conclude that the averaged threshold power densities of 2.1 kW/m^2 to 40 kW/m^2, or 14 kW/m^2 as a realistic threshold peak power density for induction of the microwave auditory effect in the near field of 1250 MHz to 3000 MHz microwaves with pulse widths between 10 ms and 30 ms. In other words, the 14 kW/m^2 per pulse peak power density generates a barely audible sound level of 0 dB. To generate sound at 60 dB, or the audible level for normal conversation, requires a 1000-fold higher power density per pulse. To generate a tissue-injuring level of sound at 120 dB would take another 1000-fold increase in the required peak power density, or 14 GW/m^2 per pulse. The corresponding theoretical temperature elevation would be about 1°C, which is safe by current protection guidelines.

For plane-wave equivalent exposures, the available computations provide two sets of data that are suitable for comparison with the results described above. In one case, the reported threshold peak incident power density for an anatomical head model was 3 kW/m^2 for 20 μs pulses at 915 MHz [12]. For the other, the threshold was about 50 kW/m^2 for 20 μs pulses at 2450 MHz [13]. The corresponding peak incident power densities at the 120 dB injury level are therefore between 3 GW/m^2 and 50 GW/m^2 per pulse, which bracket the 14 GW/m^2 per pulse from the above calculation for near-zone exposures. These peak power densities are close to and encompass the 23.8 GW/m^2 value for the dielectric breakdown of air. As the dielectric permittivity of all biological and physical materials is greater than that of air or free space, the intrinsic impedances are always smaller than that of air. The breakdown peak power density in skin, muscle, and brain tissues, for example, would be a factor of 6 to 7 higher, or 142 GW/m^2 to 166 GW/m^2, for a microwave pulse at 1000 MHz to 3000 MHz. If the microwave auditory effect is thus weaponized, lethal, or nonlethal, at sufficiently high powers, it is likely for the microwave pulses to cause brain-tissue injury or auditory-pathway nervous-tissue damage by the reverberating sonic shock waves. It would not be by microwave-pulse-induced hyperthermia through excessive temperature elevation in the brain, nor by dielectric breakdown of brain, muscle, or skin tissues.

Note that the units of measure of kW/m^2 or GW/m^2 per pulse refer to power per square meter (power density), not the total output power of any source.

In summary, depending on the power of the impinging microwave pulses, the level of induced sound pressure in the brain could be considerably above the threshold of auditory perception. They may thus approach or exceed levels of discomfort or cause brain-tissue injury. A high-power-microwave pulse-generated acoustic pressure wave initiated in the brain and reverberating inside the head could bolster the initial pressure to cause injury to brain matters.

Postscript

The author of this article was invited by the NASEM study committee to present on "Multidisciplinary Analysis of Microwave Pulse Induced Sound and Pressure in Human Heads." The talk was based on his extensive research in the microwave auditory effect.

References

1. National Academies of Sciences, Engineering, and Medicine, "An Assessment of Illness in U.S. Government Employees and Their Families at Overseas Embassies," Washington, DC, The National Academies Press, https://doi.org/10.17226/25889, December 2020.

2. J. C. Lin, "Mystery of Sonic Health Attacks on Havana-Based Diplomats," *URSI Radio Science Bulletin*, No. 362, September 2017, pp. 102-103.

3. J. C. Lin, "The Microwave Auditory Phenomenon," *Proc. IEEE*, **68**, 1980, pp. 67-73.

4. J. C. Lin, "Auditory Perception of Pulsed Microwave Radiation" in O. P. Gandhi (ed.), *Biological Effects and Medical Applications of Electromagnetic Fields*, New York, Prentice-Hall, 1990, Chapter 12, pp. 277-318.

5. J. C. Lin and Z. W. Wang, "Hearing of microwave Pulses by Humans and Animals: Effects, Mechanism, and Thresholds," *Health Phys.*, **92**, 6, June 2007, pp. 621-628.

6. J. C. Lin and Z. W. Wang, "Acoustic Pressure Waves Induced in Human Heads by RF Pulses from High-Field MRI Scanners," *Health Phys.*, **98**, 4, 2010, pp. 603-613.

7. R. Verma, R. L. Swanson, D. Parker, A. A. Ould Ismail, R. T. Shinohara, J. A. Alappatt, J. Doshi, C. Davatzikos, M. Gallaway, D. Duda, H. I. Chen, J. J. Kim, R. C. Gur, R. L. Wolf, M. S. Grady, S. Hampton, R. Diaz-Arrastia, and D. H. Smith, "Neuroimaging Findings in US Government Personnel with Possible Exposure to Directional Phenomena in Havana, Cuba," *JAMA*, **322**, 4, 2019, pp. 336-347.

8. A. H. Frey and R. Messenger, Jr., "Human Perception of Illumination with Pulsed Ultra-High-Frequency, Electromagnetic Energy," *Science*, **181**, 1973, pp. 356-358.

9. A. W. Guy, C. K., Chou, J. C. Lin, and D. Christensen, "Microwave Induced Acoustic Effects in Mammalian Auditory Systems and Physical Materials," *Annals NY Academy Sci.*, **247**, 1975, pp. 194-218.

10. A. W. Guy, J. C. Lin and C. K. Chou, "Electrophysiological Effects of Electromagnetic Fields on Animals," in *Fundamentals and Applied Aspects of Nonionizing Radiation*, New York, Plenum Press, 1975, pp. 167-211.

11. C. A. Cain and W. J. Rissman, "Mammalian Auditory Response to 3.0 GHz Microwave Pulses," *IEEE Trans. on Biomedical Engineering*, **25**, 1978, 288-293.

12. Y. Watanabe, T. Tanaka, M. Taki, and S. I. Watanabe, "FDTD Analysis of Microwave Hearing Effect," *IEEE Trans. Microwave Theory Techniques*, **48**, 2000, pp. 2126-2132.

13. N. M. Yitzhak, R. Ruppin, and R. Hareuveny, "Numerical Simulation of Pressure Waves in the Cochlea Induced by a Microwave Pulse," *Bioelectromagnetics*, **35**, 2014, pp. 491-496.

Asta Pellinen-Wannberg
Umeå University, Department of Physics and
Swedish Institute of Space Physics
S-90187 Umeå, Sweden
Tel: +46 90 786 7492
E-mail: asta.pellinen-wannberg@umu.se

Introduction by the Associate Editor

I met Nicole for the first time at a Spacecraft Charging Conference at ESTEC, Noordwijk, Netherlands, some 20 years ago. There at the ESTEC lunchroom, I already noticed a very engaged and colorful scientist. We later have been on the same ISSI (International Space Science Institute, Bern, Switzerland) Team on dust-plasma interactions. In March 2013, Nicole visited a workshop at the Swedish Institute of Space Physics in Kiruna, 120 km north of the polar circle, for five days. To her disappointment, the magnetometer lines were very straight, indicating no geomagnetic activity. However, late on the last night, a faint green auroral arc started to drift from the northern sky and intensify. We saw this from a car and had to stop. I remember Nicole standing there with the aurora as background in her very elegant long stocking cap in the −20° C cold to follow all the substorm phases forever. Fortunately, the rest of us could stay indoors, but felt worried about her. Afterwards, she convinced us that she had not felt any cold in her interaction with the beautiful Northern Lights.

Nicole refers in her story to the infancy of French space research, when instruments were unproven, there was some knowledge or just guesses of how space around us was, and nobody knew in advance what would be observed. Many of us remember that fascinating time, when almost every PhD student had a chance to discover new phenomena in their first measurements. Nicole describes this in a wonderful way in her contribution to Women in Radio Science.

Dr. Nicole Meyer-Vernet's research focuses on physics, especially space physics, astrophysics, and, more recently, life physics. In particular, she participated in the analysis and interpretation of data from the Voyager encounters with Saturn, Uranus, and Neptune; from the ISEE3/ICE spacecraft in the solar wind and during its encounter with comet Giacobini-Zinner; and from Ulysses' exploration of the heliosphere and Io torus as Co-I of the radio instrument URAP. She has initiated and developed the technique of quasi-thermal noise spectroscopy for measuring *in situ* electron properties in space, used on ISEE-3/ICE, WIND, Ulysses, STEREO, Cassini, Bepi-Colombo, Parker Solar Probe, and Solar Orbiter. She also developed the *in-situ* detection of dust, including nano-dust with wave instruments. As Co-Investigator of the FIELDS instrument on Parker Solar Probe, she presently participates in the analysis and interpretation of these results, and is now working part-time on life physics. She is the author of *Basis of the Solar Wind* (Cambridge University Press), has co-edited several books, and authored over 200 publications in astronomy, physics, and biology, including physics of space plasmas and dust-plasma interactions.

Freedom, Research and Serendipity: The Joy of Discovery

Nicole Meyer-Vernet

LESIA, Observatoire de Paris, University PSL,
CNRS, 5 Place Jules Janssen
92195 Meudon, France
E-mail: nicole.meyer@obspm.fr
www:https://lesia.obspm.fr/perso/nicole-meyer/

When asked to write this article, I wondered from where to start and what to write: in chronological order or by research domains? I decided to focus on how fun it is to do science, on the importance of freedom and serendipity, and to only mention subjects close to radio science.

I grew up among books, in the heart of the Paris Latin quarter, into a family that valued education and knowledge. When I was a small girl, my father – a land surveyor – sometimes took me to his office in Paris city hall, and lent me a small part of his desk, covered with maps, squares, and pencils, and a mechanical calculating machine operated by turning a handle that I could not touch. I loved Jules Verne's books, my heroes were explorers of the world, and some teachers despised me because I harassed them with questions they could not answer.

Understanding the world meant studying physics and/or biology. At the end of my studies at École Normale Supérieure, when I had to choose a PhD subject, an exceptional opportunity arose: Jean-Louis Steinberg had created a laboratory of space radio astronomy in the Observatory in Meudon (Figure 1), and was assembling a team of young physicists and engineers. Located at the edge of a forest, the Observatory in Meudon was (and still is) a wonderful and magical place, with old remains dating from Louis XIV, buildings and instruments scattered among meadows where wild orchids spring up, and a pond full of huge carp seeming nearly as old as the buildings.

Figure 1. Meudon Observatory in Winter

There started my professional career.

In the 1970s, May 1968 was close by, with the freedom brought about by those events, and French space research was in its infancy, as well as the Centre National d'Études Spatiales. My PhD subject was very exciting. I would be responsible of a mission involving three small rocket launches in the ionosphere, to solve an interesting space radio-astronomy problem. Space environments are ionized, except for the close vicinity of planets protected

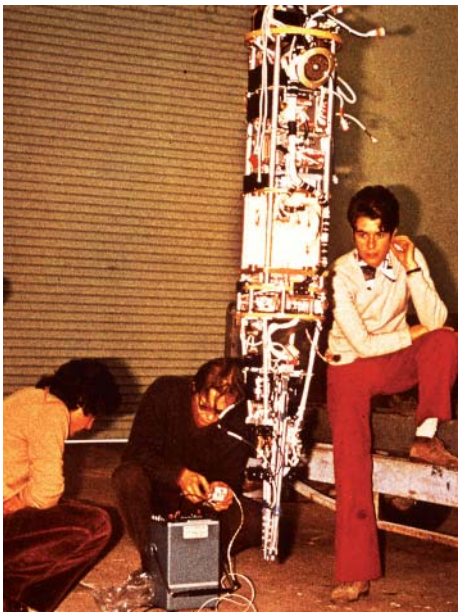

Figure 2. Tests on the payload at CEL in 1970 (l-r: P. Tilloles, R. Manning, and N. M.-V.).

Figure 3. Our office at CEL (l-r: N. M.-V. and P. Tilloles).

by their dense atmospheres. Spaceborne electric antennas are thus immersed in plasmas. How are their measurements affected at frequencies close to the plasma resonances? This question had been tackled by some pioneers, such as Keith Balmain (who was to participate in my thesis jury), but many questions still remained and no data were available.

French rockets were then launched from the "Centre d'Essais des Landes" (CEL), a military base close to Biscarosse beach. We worked there to test the instruments (Figure 2), waiting for suitable launch conditions. We were young, having much fun, and the boss (me) was a 24-year-old female scientist. We got about by bicycle, and our office was littered with a mess of electric material, papers covered with figures, and even comics (Figure 3). The military did not like it!

When space science was in its infancy, a PhD thesis based on a space mission (Figure 4) required doing almost

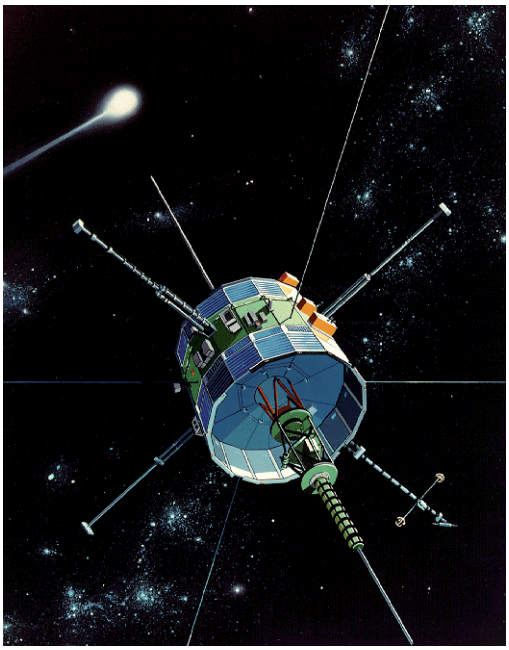

Figure 5. The spacecraft ISEE-3, later renamed to ICE.

Figure 4. The Dragon rocket with the payload EIDI 1 on its launch pad (22/10/1970, photo C.E.L.).

everything, from instrument testing to plasma-physics calculations: - marvelous school to learn space science. I had the luck of having a boss, Jean-Louis Steinberg, who gave me entire freedom... even when he did not agree with me.

These small experiments (EIDI), which measured the impedance of electric antennas in the ionosphere, would, after many peripeties, lead to a novel technique to measure plasma properties in space, and even to detect dust grains. However, we did not yet know that.

After my thesis, I began to explore several domains outside my research area. I had joined the French Centre National de la Recherche Scientifique (CNRS). They rightly wanted me to provide a research program, and were very angry when I refused to do so, since I had not yet found a suitable subject. Fortunately, my boss backed me up, asking them to let me be free. I then applied to a CNRS Biology course for physicists. Extrasolar planets had not yet been discovered, and the organizers did not understand why a young researcher in space radio astronomy wished to study biology, so they rebutted me.

I then fumbled into my PhD studies. Since Nyquist's theorem tells us that the electric noise measured by an antenna is related to its electrical resistance via the

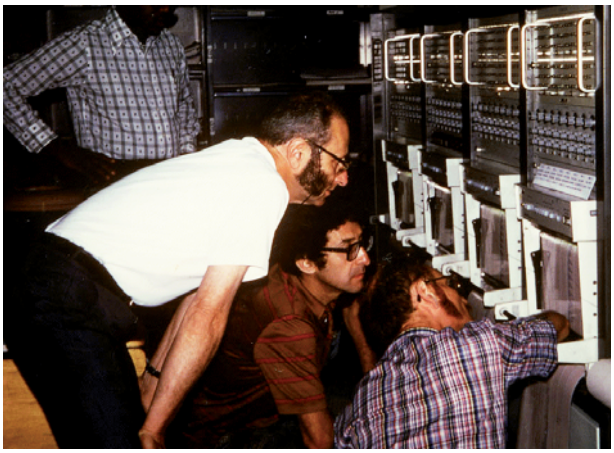

Figure 6. J. L. Steinberg, J. Fainberg, and R. Knoll looking at the first data at NASA/JSFC (8/13/1978, © S. Hoang).

temperature of the surrounding blackbody, one should measure in the interplanetary medium a weak, but detectable, noise produced by the quasi-thermal motion of the plasma electrons around the antenna, which should reveal the local electron density and temperature. In other words, an electric antenna connected to a sensitive radio receiver could serve as an *in-situ* plasma particle detector! I calculated the spectral density that should be measured in the solar wind and submitted this prediction to the *Journal of Geophysical Research*. Unfortunately, the journal rejected the paper, on the grounds that such a noise had never been measured before, and that anyway the theory was too simple to be applicable in the solar wind; the reviewer suggested that I should instead submit my manuscript to a purely theoretical journal.

Then, luck intervened.

The International Sun-Earth Explorer-3 (ISEE-3, Figure 5) had been launched a few days after the submission of my paper, and was orbiting in the interplanetary medium around the L1 Earth-Sun Lagrangian point. It carried the most-sensitive radio receiver ever flown, the data from which were becoming available. Furthermore, the investigators (Figure 6) were just discovering a weak "mysterious" radio emission, the spectrum of which turned out to agree in amplitude and shape with my predictions! This agreement prompted the immediate acceptance of the manuscript, which provided also a basic alternative explanation for observations previously interpreted as "new" emissions due to plasma instabilities.

In the beginning, this paper was badly received. Theoreticians did not like it because the early 1980s were the great epoch of plasma instabilities. Showing that emissions previously interpreted in this way were instead due to an effect as trivial as quasi-thermal noise was a crime of lèse-majesté, even though this explanation followed *Ockham's razor* prescription that "pluralitas non estponenda sine necessitate." Experimenters did not like it either, because this novel technique of measuring

Figure 7. (l-r) S. Hoang, C. Perche, N. M.-V., and P. Couturier showing their results on the day after the encounter (September 1985, NASA/GSFC).

in situ plasma properties via analysis of a noise spectrum contradicted the current paradigm that plasma detection by wave instruments should require "active" sounding. Furthermore, this simple "passive" technique could be a serious challenger in the hard battle for instrument selection on future space missions.

However, luck struck again. Halley's comet was returning soon, and space agencies were in a hurry to prepare exploring missions. The Halley's armada included the European Space Agency's Giotto, two probes built by the Soviet Union, and two Japanese probes. For once, the US would not take the lead! However, the NASA engineers discovered that they could change the trajectory of the spacecraft ISEE-3, then renamed International Cometary Explorer (ICE), to make it encounter the plasma tail of comet Giacobini-Zinnernear its 1985 perihelion, one year before the armada encounter with comet Halley. This gave us an opportunity to measure *in situ* the comet's plasma properties with the inboard radio experiment via the new method of quasi-thermal noise spectroscopy (QTN), if two

Figure 8. Bob Stone and J. L. Steinberg, ISEE-3/ ICE radio instrument PIs (© S. Hoang).

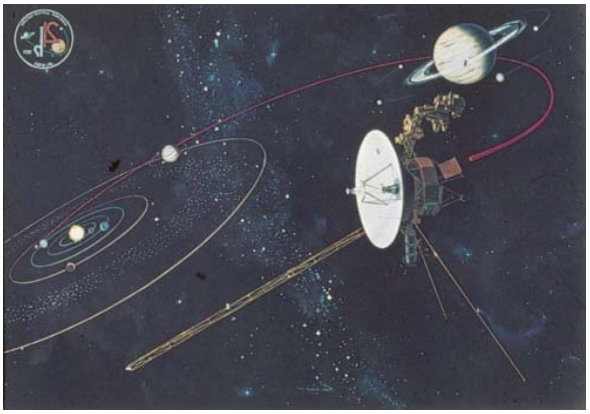

Figure 9. The mission Voyager (only Voyager 2 explored the planets Uranus and Neptune).

Figure10. The strawman payload of the space agencies (adapted from Meyer-Vernet et al., *J. Geophys. Res.*, 2017, drawing by F. Meyer).

conditions were met. First, the comet should not be too dusty, so that the fragile 0.2-mm radius electric antennas would not to be broken by dust impacts. Second, the ambient plasma Debye length should be smaller than the 45-m antenna length, for this latter length to exceed the involved (Langmuir) wavelengths. Luckily, the comet was not very dusty and the plasma tail was dense and cold, so that both conditions happened to be met.

Our small team worked night and day in the stimulating environment of NASA Goddard Space Flight Center (GSFC), and produced the first and only measurement of the electron properties in a comet's plasma tail (Figure 7).

The radio experiment that its designers (Figure 8) had originally planned for solar-burst radio mapping thus had turned out to also be an efficient plasma *in situ* detector. In contrast, the dedicated plasma detector did not work well, because the comet's tail properties were outside the range for which the instrument had been built. At the hotel near GSFC, we happened to have a discussion with an American journalist who was surprised that being a woman with two children, I could lead the QTNteam. She did not believe me when I explained that my husband was taking care of them in my absence, and that this behavior was common in France.

A few years before the comet saga, another event extended the range of *in situ* detections with radio receivers. The twin Voyager spacecraft, maybe the greatest space mission of the 20th century, carried a Planetary Radio Astronomy experiment (Figure 9). At Saturn's ring plane crossing in 1980, this instrument measured an intense power spectrum, decreasing with frequency as f^4. Where did it come from? The Voyager's did not carry dust detectors, but the plasma-wave instrument, operating at lower frequencies than the radio instrument, simultaneously measured an f^2 power spectrum, whereas its waveform receiver detected electric pulses due to the charges produced by the vaporization of dust grains impacting the spacecraft. The radio-receiver measuring frequency exceeded the inverse of the pulse rise time, itself much smaller than the relaxation time. This meant that the voltage pulses should have an f^2 Fourier transform, which explained the observed f^4

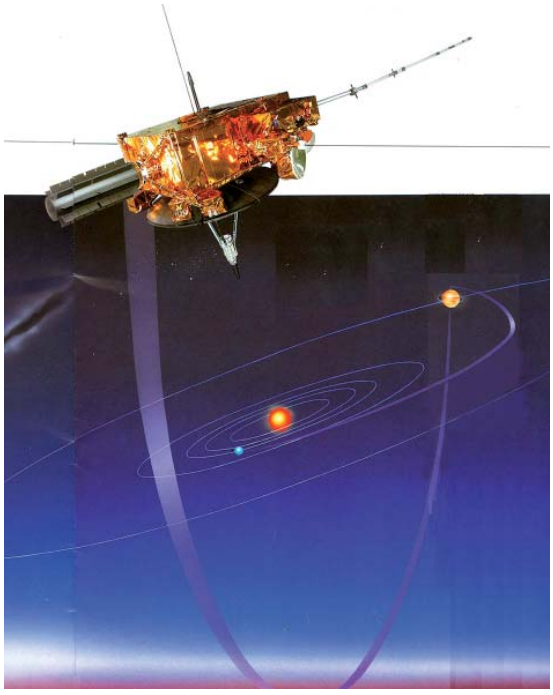

Figure 11. An artist's view of Ulysses exploring the solar wind in three dimensions (ESA).

Figure 12. The Ulysses radio.

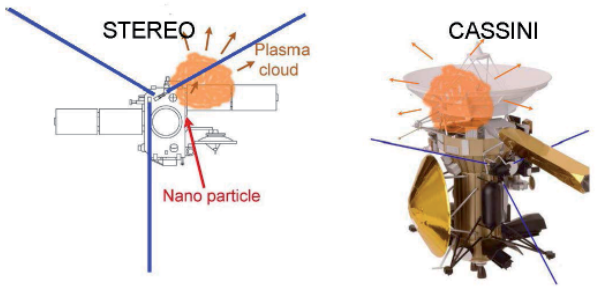

Figure 13. The principle of in situ dust detection with a radio instrument on STEREO and Cassini (electric antennas shown in blue, and impact plasma cloud shown in orange).

power spectrum. On the other hand, the plasma instrument, working at frequencies intermediate between the inverse of the rise and decay times, should see roughly step-like pulses, which explained the f^2 power spectrum. In this way, the electric antennas measured the dilute E and G rings of Saturn onboard, respectively, Voyager 1 and 2. We performed similar detections in 1986 and 1989 when Voyager 2 crossed the dilute rings of the planets Uranus and Neptune.

These results proved that long electric antennas onboard spacecraft (Figure 10), the radio receivers of which are generally designed to measure electromagnetic waves from distant sources, could be efficient *in situ* detectors for both plasma and dust. This paved the way to *in situ* measurements of plasmas and dust in various media – such as comets, planets, and the solar wind – onboard numerous spacecraft carrying radio instruments.

October 6, 1990, saw the launch of Ulysses, the outcome of thirty years of international engineering and science efforts to send a spacecraft where no probe had ever flown. Exploring the heliosphere outside the ecliptic plane was proposed as early as 1959 by a few visionary scientists, but only in the 1970s did the idea appear technically feasible by using Jupiter's gravity assist (Figure 11). The American and European space agencies then proposed the International Solar Polar Mission, a package of two spacecraft that were to be launched in 1983 and sweep towards opposite sides of the ecliptic plane, in order to achieve a stereoscopic view of the solar wind. Unfortunately, technical and financial difficulties led NASA to cancel the US spacecraft, transforming the mission into a single spacecraft built by ESA, carrying European and US instruments, to be launched by the Space Shuttle. In late 1983, the project had still to wait because the Shuttle was not ready. 1986 saw a catastrophic event: the Space Shuttle Challenger blew up, a few months before the planned launch, further delaying the mission.

Ulysses carried ten sophisticated instruments, and its three-dimensional exploration of the solar wind changed our view of the heliosphere. I had the chance to work on the results of the Unified Radio And Plasma Wave Experiment with a team of colleagues and friends at Meudon and NASA/GSFC, while leading brilliant PhD students. The radio receiver built at Meudon, despite its old technology (Figure 12) due to the numerous launch delays, worked perfectly well during the 18 years of the mission. Among many results, it produced routine solar-wind electron measurements with the new QTN technique.

Jupiter's encounter enabled Ulysses to explore the plasma torus of the satellite Io, and to measure the electron properties in this medium, therefore extending the technique to magnetized plasmas. This work showed that electric antennas in space do not always behave as expected. Electric fields are generally deduced by dividing the voltage by the antenna length, since short antennas measure a voltage proportional to their electric length and respond best to electric fields along their length. However, although the antenna was electromagnetically short, the power was not maximum when the electric field was oriented along its length. This was because the antenna measured (electrostatic) Bernstein waves, of wavelength close to the electron gyroradius, much smaller than the electromagnetic wavelength, so that the antenna was not short for these waves. These measurements also illustrated the non-Maxwellian nature of plasmas and its important consequences: a change of paradigm pioneered by Jack Scudder in another context.

Electric antennas also served to discover nanodust accelerated by the solar wind. This is a science detective story and a notable example of serendipity. This was also a striking performance of radio science, since this *in situ* detection was made with two spacecraft, STEREO and Cassini (Figure 13), carrying different wave receivers, whereas dedicated dust detectors had not seen such solar-wind particles, which were unknown when the instruments had been built.

The story began when the wave instrument on STEREO (S/WAVES) measured voltage pulses with an intense and variable power spectrum close to f^4, similar to the radio-dust measurements made by Voyager in planetary rings nearly thirty years before. However, these measurements raised a big problem. The amplitude of the pulses suggested micro dust, but the pulse rate implied a dust flux exceeding the known values by four orders of magnitude, since the spacecraft was at 1 AU, far from any planet or comet.

The solution emerged at an ISSI International Team on "Dust-Plasma Interactions," led by Ingrid Mann. She showed me her recent paper, suggesting that the solar wind carried nanodust, the large charge-to-mass ratio of which enabled the nanodust particles to be accelerated by the Lorentz force up to roughly the solar-wind speed. This work brought about the missing piece of the puzzle. Indeed, the electric charge released by vaporization and ionization of dust grains impacting a spacecraft increases with speed much faster than their kinetic energy. A nanodust

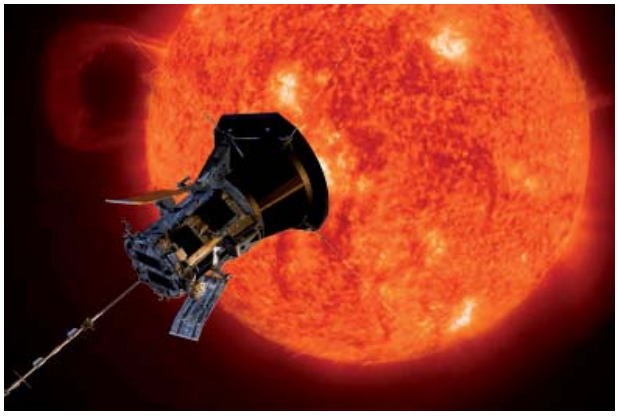

Figure 14. Parker Solar Probe (artist concept, credit: NASA/Johns Hopkins APL/Steve Gribben).

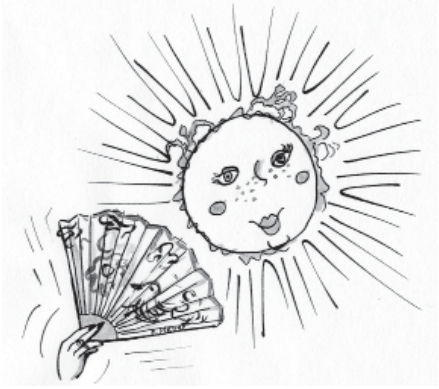

Figure 15. How does the solar wind blow? (*Basics of the Solar Wind*, Cambridge University Press 2007, drawing by F. Meyer).

impacting at solar-wind speed hence releases a similar charge as a micron-sized grain impacting at Keplerian speed. The impacts could thus be nanodust, which should solve the impact-rate problem, since their flux was expected to exceed that of microdust by several orders of magnitude; we then submitted a paper on these results. However, this was not the end of the story, since the original paper was rejected on the grounds that dedicated dust detectors had not previously observed these particles in the solar wind, and that radio instruments were not expected to be good enough to detect such dust in space.

To answer this objection, we then looked at the data of the radio receiver (Radio and Plasma Wave Science) on the spacecraft Cassini close to Jupiter, at times when the dedicated dust detector had detected fast nanodust ejected from Jupiter. We found nanodust signals at similar times with a similar rate as found by the dust detectors, proving that radio instruments were indeed capable of detecting nanodust, contrary to claims of the contrary. The final confirmation came from the Cassini radio data during the spacecraft cruise phase between 1 AU and 5 AU in the solar wind. Nanodust were there, with a variable flux compatible with both that found on STEREO at 1 AU and the theoretical simulations, and decreasing with distance as expected.

The performance of a radio receiver at the ports of an electric antenna for measuring *in situ* plasma particles and dust played an important part in the selection of the FIELDS instrument on the Parker Solar Probe mission (Figure 14). This was to carry electric antennas but no dedicated dust detector. It will approach the sun up to 9.5 solar radii in 2025, in order to understand the solar corona and the origin of the solar wind (Figure 15).

However, this is another story.

Figure 16. Some participants in the "Rencontres de l'Observatoire" at Meudon in January 2000 ("Physics of Space: Growth Points and Problems," Astrophys. Space Sci., 277, 381, 2001).

Figure 17. During a mini-symposium at the Solar-Terrestrial Centre of Excellence (l-r: E. N. Parker, J. Lemaire, and N. M.-V., Brussels, June 2009).

I will not mention a number of studies in other domains of physics and astronomy, but I wish to evoke the importance of friends and colleagues and of the international dimension of research: working together on projects and problems, laughing, exchanging ideas, learning new subjects, understanding surprising data, fighting together to make people change paradigms and accept new ideas or measurement techniques. Many people of diverse languages and cultures have influenced me (Figure 16), either personally or through their writings.

For example, the Ulysses data raised a number of new problems and were a strong encouragement to study the physics of weakly collisional plasmas, the importance of not being Maxwellian and the limitations of fluid models, in particular in the solar wind. I then had the great opportunity to meet a pioneer of kinetic solar-wind models, Joseph Lemaire, and to be involved in lively disputes between him and Eugene Parker on the importance of the electrons in accelerating the solar wind: another example of the difficulties in changing paradigms (Figure 17).

Juggling with spacecraft, planets, plasmas, and dust, while learning new subjects, is so rewarding that I always had (and still have) much fun in doing research (Figure 18). During my career I never had the impression of working, partly thanks to the support and warm environment of my laboratory, the LESIA (Observatoire de Paris, Meudon). Starting as a group focused on space radio astronomy, it now covers a wide spectrum of subjects, from solar physics to planetology, stars, galaxies, extrasolar planets, and high-resolution optical techniques with applications from astronomy to biomedicine. I am also now working part-time on the subject I wanted to address many years

Figure 18. From "Un Autre Monde" (Granville, 1844)

ago: physical biology and applications to the prospects of life on other planets. Such freedom and independence of fashion is unfortunately more and more difficult to achieve nowadays, because most institutions do not like free spirits (Figure 19).

> Theologians have their bells to ring: physicists have their laughter.
> (Bertolt Brecht in *Life of Galileo*, translated by John Willett, New York, Arcade Publishers)

Figure 19. N. M.-V. in the Observatory in Meudon.

URSI Awards 2020 - 2021

At their virtual Board meeting, based on the recommendations of the Awards Panel, the URSI Board of Officers decided to give the 2020 URSI awards to the following distinguished scientists. The URSI GASS 2020 could not take place due to Covid-19, that's why it was decided to hand them over to the awardees at the URSI GASS 2021.

Balthasar van der Pol Gold Medal

The Balthasar van der Pol Gold Medal was awarded **to Prof. Emeritus K. ITO (Japan)** with the citation,

For contributions to the research and development in the fields of medical applications of electromagnetic waves and their evaluation using human-equivalent phantoms.

Appleton Prize

The Appleton Prize was awarded to **Prof. R.B. Horne (UK)** with the citation,

For leadership and theories of charged particle dynamics in the Earth and planetary magnetospheres leading to practical space weather forecasting of their high energy particle environment

John Howard Dellinger Gold Medal

The John Howard Dellinger Gold Medal was awarded to **Prof. S. Maci (Italy)** with the citation,

For contributions on diffraction theory, metasurfaces and for impact on education in electromagnetism.

Booker Gold Medal

The Booker Gold Medal was awarded to **Prof. J. Volakis (USA)** with the citation,

For seminal contributions to electromagnetics, including small, ultra-wideband and textile antennas and arrays, low power transceivers, diffraction and for transitioning hybrid finite element methods into commercial computational toolsets.

Karl Rawer Gold Medal

The Karl Rawer Gold Medal was awarded to **Dr. R. Mittra (USA)** with the citation,

For contributions to analytical and numerical techniques in electromagnetics and to antenna theory and design.

Santimay Basu Prize

The Santimay Basu Prize was awarded to **Dr. X. Xu (USA)** with the citation :

For wave propagation and scattering in dense random media with applications to microwave remote sensing of snow.

Issac Koga Gold Medal

The Issac Koga Gold Medal was awarded to **Prof. R. He (USA)** with the citation,

For outstanding investigations of radio propagation and channel modelling in high mobility scenarios that has resulted in significant improvements in the communication system evaluation and design.

President's Award 2020

The President's Award was awarded to **Prof. K. Kobayashi (Japan)** with the citation :

For his leadership and untiring efforts in initiating, organizing and establishing AP-RASC as one of the URSI Flagship Meetings.

Certificates of Recognition
2020 - 2021

Prof. S. ANANTHAKRISHNAN
(India)

For establishing a significant and prolonged URSI activity in India.

Prof. S. RENGARAJAN
(USA)

For his leadership of the student paper competition at GASS 2017, AT-RASC 2018 and GASS 2020 & 2021.

Prof. C. CAROBBI
(Italy)

For his outstanding contributions devoted to organizing the URSI GASS 2020-2021.

Prof. G. D'INZEO
(Italy)

For his outstanding contributions devoted to organizing the URSI GASS 2020-2021.

Prof. A. SENGUPTA
(India)

For his outstanding contributions to the organization of the URSI Asia-Pacific Radio Science Conference (AP-RASC) 2019.

Prof. A. SIBILLE
(France)

For his outstanding contributions as Scientific Programme Coordinator of URSI GASS 2020 & 2021.

Prof. R. SORRENTINO
(Italy)

For his outstanding national and international contributions to URSI and in particular to both GASS 2020 & 2021 held in Rome, Italy.

Dr. P. WILKINSON
(Australia)

For his untiring efforts in editing and perfecting the contributions to the Centenary Book.

The URSI awards will be presented on-site and online to the awardees during the Opening Ceremony of the XXXIVth General Assembly and Scientific Symposium at the Basilica San Pietro in Vincoli, Rome, Italy on August 29, 2021.

Report of URSI Commission D: 2017-2021

This document provides the activities of URSI Commission D during the period 2017-2021. Due to the COVID-19 pandemic, the reporting period has been extended to cover the four-year period from 2017 to 2021. The report includes the main international conferences and workshops that received technical sponsorship or financial support from the Commission. The report further provides an overview of the scientific program scheduled for the next General Assembly, to be held in Rome, Italy, from August 28 to September 4, 2021.

1. Officers of Commission D

During the period 2017-2021, the officers of Commission D were as follows:

Chair: Dr. Apostolos Georgiadis, Heriot-Watt University, Edinburgh, UK; e-mail: apostolos.georgiadis@ieee.org

Vice Chair: Prof. Naoki Shinohara, Kyoto University, Kyoto, Japan; e-mail: shino@rish.kyoto-u.ac.jp

Past Chair: Dr. Günter Steinmeyer, Max Born Institute, Berlin, Germany; e-mail: steinmey@mbi-berlin.de

Early Career Representatives:
Dr. Arnaud Vena, Université Montpellier 2, France; e-mail: arnaud.vena@ies.univ-montp2.fr

Dr. Hossein Asghari, Loyola Marymount University, Los Angeles, USA; e-mail: Mohammadhossein.Asghari@lmu.edu

2. Terms of Reference of Commission D

The Commission promotes research and reviews new developments in:

1. Electronic systems that push beyond current frontiers.
2. Microwave, millimeter wave and THz devices, circuits and systems.
3. Nanotechnologies and nanoelectronics.
4. Combined and hybrid photonic and electronic systems.
5. Photonic devices, systems, and their applications.
6. Photonic signal processing schemes, regardless of frequency of signal processed.
7. Optoelectronic systems, plasmonics, and electro-optics.
8. Physics, theoretical modeling, and numerical simulation of all of the latter.

The Commission focuses on electronics and photonics devices, circuits, and systems for the purpose of implementing either previously inaccessible functionalities or of improving the performance of current electronic-only or photonic-only technologies.

3. Evolution of Topics and Future Planning in Commission D

During the business meeting at GASS 2017, it was decided to focus efforts on attracting more interest to ground-breaking topics in the electronics and photonics fields, and to foster collaboration with IEEE MTT-S. Several action items were taken to organize activities in Commission D:

1. Focus on topics that unite electronics and photonics, e.g., optical telecommunications, terahertz waves, plasmonics, and metrology.
2. Invitation of world-leading researchers to attend the URSI GASS.
3. Strengthen the relationship with IEEE and specifically the IEEE MTT Society. Efforts were to be led by Prof. Tatsuo Itoh and Prof. Ke Wu, in order to formulate a sister-society agreement that would involve all possible joint activities, such as mutual sponsorship of conferences and joint publications.
4. Contribution from past Chairs of Commission D to the URSI centenary book.
5. Organization of a 100 Year Anniversary of URSI Commission D session at the GASS 2021, with invited presentations from past Commission D Chairs, following the initiative of past Chair Prof. Smail Tedjini.

4. Supported Conferences and Workshops

The Commission has received several requests for either technical or financial sponsorship. Each request was considered and positively agreed to when the topic of the event had a connection with the Terms of Reference of Commission D. In total, eight sponsorships were delivered, as follows:

1. Metamaterials 2021, 15th International Congress on Artificial Materials for Novel Wave Phenomena, New York, USA, 20-25 September 2021, https://congress.metamorphose-vi.org/.
2. MAREW 2021, Microwave and Radio Electronics Week 2021, Brno, Czech Republic, 19-21 April 2021, https://www.marew.cz/.
3. ISAP2020, 2020 International Symposium on Antennas and Propagation, 25-28 January 2021, Osaka, Japan, https://www.ieice.org/cs/isap/2020/.
4. Metamaterials 2020, 14th International Congress on Artificial Materials for Novel Wave Phenomena, https://congress.metamorphose-vi.org/.
5. 2019 IEEE RFID-TA, 10th IEEE International Conference on RFID Technology and Applications, 25-27 September 2019, Pisa, Italy, http://2019.ieee-rfidta.org/.
6. URSI-JRSM 2019, 2019 URSI-Japan Radio Science Meeting, September 5-6, 2019, Tokyo, Japan, http://www.ursi.jp/conference/jrsm2019.
7. APMC 2018, Asia-Pacific Microwave Conference 2018, November 6-9, 2018, Kyoto, Japan, https://apmc-mwe.org/apmc2018/.
8. ISAP2018, 2018 International Symposium on Antennas and Propagation, October 23-26, 2018, Busan, Korea, http://isap-2018.org.

5. Flagship Conferences

Commission D participated in four flagship conferences, namely the AT-RASC in Gran Canaria, Spain, in 2018; the AP-RASC in New Delhi, India, in 2019; the 33rd URSI GASS in Rome, Italy, in 2020 (cancelled as an in-person event due to COVID-19 pandemic); and the 34th URSI GASS in Rome, Italy, in 2021.

5.1 AT-RASC

The conference was held in Gran Canaria, Spain, May 28 - June 1, 2018. There were a total of 87 papers in Commission D, arranged into three tutorial lectures, 75 oral presentations, and a further nine poster presentations. Table 1 includes an overview of the Commission D paper-submission statistics.

There were three tutorial presentations scheduled. A first tutorial talk was delivered by Prof. Mona Jarrahi, University of California, Los Angeles, USA, on "Plasmonic Antennas for Advanced THz Imaging and Sensing." A second tutorial talk was delivered by Dr. Apostolos Georgiadis, Heriot-Watt University, UK, on "Energy Harvesting and Wireless Power Transfer for RFID and Wireless Sensors." A third tutorial talk was delivered by Dr. Hossein Asghari, Loyola Marymount University, USA, on "Optical Real-Time Measurement Techniques."

5.2 AP-RASC

The conference was held in New Delhi, India, March 9-15, 2019. There were a total of 76 papers in Commission D, arranged into one Commission keynote lecture, eight oral sessions comprising 47 papers, and a further 29 poster presentations. Table 2 includes an overview of the Commission D paper-submission statistics.

A Commission keynote lecture was delivered by Prof. Tadao Nagatsuma, Osaka University, Japan, on "Terahertz-Wave Applications Enabled by Photonics."

5.3 URSI-GASS 2020 and 2021

The 33rd URSI General Assembly and Scientific Symposium, URSI GASS 2020, was originally scheduled

Table 1. Commission D paper-submission statistics for AT-RASC 2018.

Technical Topic	Number of Papers
Tutorial	3
D06 Advances in Ultrafast Pulse Characterization Techniques: Towards an Optical Oscilloscope	18
Electronics and Photonics	11
Microwave Photonics	5
Plasmonics	10
Advances in Radiative and Non-Radiative Wireless Power Transfer	6
Wireless Wearable Devices for Identification and Sensing	9
Photonic Signal Processing, Real-Time Instruments and Biomedical Imaging	9
GHz and THz Metrology	2
Advances in Leaky Wave Antenna Technologies	7
Printed Electronics and Novel Materials for Wireless Devices and Systems	7
Total	**87**

Table 2. Commission D paper-submission statistics for AP-RASC 2019.

Technical Topic	Number of Papers
Commission Keynote	1
Electronic Systems Beyond Current Frontiers Including Flexible, 3D and Inkjet-Printed Electronics	1
Microwave, Millimeter Wave and THz Devices, Circuits and Systems	13
Electronics and Photonics for 5G and Beyond	1
Microwave and THz Photonics	13
Ultrafast Optics and Photonics	18
Photonic Signal Processing, Real-Time Instruments and Biomedical Imaging	8
Optoelectronic Systems, Plasmonics, and Electro-optics	7
Wireless Power Transfer and Energy Harvesting	5
Wireless Devices and Sensors for Harsh Environments	1
DOS – Any Other Aspect of Electronics and Photonics	8
Total	**76**

to take place August 29-September 5, 2020, in Rome, Italy. There were a total of 145 accepted papers in Commission D. However, due to the COVID-19 pandemic, it was decided to cancel the 2020 conference organization as a physical event. In view of a record overall number of submitted papers at the conference in all Commissions, it was decided to publish the proceedings of the 33rd URSI-GASS [with recorded presentations of the papers being made available online]. Alternatively, the authors of accepted papers were given the option to submit their papers unchanged to the 34th URSI GASS 2021, where the papers would be considered automatically accepted.

The 34th URSI General Assembly and Scientific Symposium, URSI GASS 2021, will be held in Rome, Italy, August 28-September 4, 2021. The original submission deadline for URSI GASS 2021 was set to January 31, 2021, and subsequently extended to February 12, 2021. There were a total of 139 accepted papers in Commission D, which included 30 papers originally accepted for GASS 2020. Table 3 includes an overview of the Commission D paper-submission statistics. The final distribution of the papers into sessions differed slightly from Table 3 in order to facilitate the organization of the overall technical program of the conference. Approximately 25% of the accepted papers were allocated as flash interactive presentations (FIPs), and the rest were distributed into oral sessions.

A tutorial talk will be given by Prof. Gaetano Marrocco, University of Rome, Tor Vergata, Italy, on "How State of the Art RFID Technology and Research May Help Facing Pandemics." Furthermore, an invited talk will be given by Prof. Federico Capasso, Harvard University, USA, on "Metasurface Polarization Optics," as part of the session on metasurfaces-enabled polarization control.

Table 3. Commission D paper-submission statistics for URSI GASS 2021.

Technical Topic	Number of Papers
Tutorial	1
Photonic Signal Processing, Real-Time Instruments & Biomedical Imaging	6
Near Field Wireless Power Transfer	7
Far-Field Wireless Power Transfer and Energy Harvesting	16
Substrate Integrated Circuit for 5G and Beyond	9
RFID and Backscatter Communication and Sensing Technologies	8
Antennas & Electronics for Wearable, Epidermal, & Implantable Devices	11
Chipless RFID	7
Integrated Terahertz Electronic and Photonic Devices and Systems	9
Microwave and Photonic Subsystems for Beyond 5G/6G Communications	7
Plasmonics and Metamaterials	12
100 Year Anniversary of URSI Commission D, Electronics & Photonics	7
Open Session – Electronics and Photonics	8
Meas. and Instr. Technologies for mm and THz Waves (with Commission A)	6
Metasurfaces-Enabled Polarization Control (with Commission B)	16
THz Communications (with Commission C)	3
Bio-Effects and EM Interference of Wireless Power Transfer (with Commission K)	5
Wearable and Textile Antenna for WBAN (with Commission K)	1
Total	**139**

6. Working Groups within Commission D

D.1 RFID Technologies and Privacy of Data

Chair: Dr. S. Tedjini (France); e-mail: smail.tedjini@lcis.grenoble-inp.fr

Vice-Chair: Dr. G. Marrocco (Italy); e-mail: marrocco@disp.uniroma2.it

Apostolos Georgiadis
Chair, URSI Commission D
Heriot-Watt University
Edinburgh, UK
E-mail: apostolos.georgiadis@ieee.org

Report URSI Commission J: 2017-2021

This is a brief summary of the activities of Commission J and the developments in radio astronomy during this triennium. This report covers four years, due to the worldwide COVID-19 pandemic that forced the postponement of URSI GASS 2020 until 2021. All officers agreed to serve an additional year of their terms.

1. Officers of Commission J for this Triennium

Chair: Richard F. Bradley, NRAO, United States

Vice Chair: Douglas Bock, CSIRO, Australia

Past Chair: Willem Baan, ASTRON, The Netherlands

ECR: Stefan Wijnholds, ASTRON, The Netherlands
Jacki Gilmore, Stellenbosch U., South Africa

2. Terms of Reference for Commission J

The activities of the Commission include:

- Observation and interpretation of cosmic radio emissions from the early universe to the present epoch and
- Radio reflections from solar system bodies

Emphasis is placed on:

- The promotion of science-driven techniques for making radio-astronomical observations and data analysis,
- Support of activities to protect radio-astronomical observations from harmful interference.

3. Finances

The budget for Commission J was used to support travel for officials and for support of a few workshops/meetings to provide YS participation (budget 24,185 Euros, expenditures 17,632 Euros). The surplus was 6953 Euros.

4. Support of Meetings and Workshops

The meetings and workshops shown in Table 1 were provided with technical and/or financial support.

5. Vice Chair and Early Career Representative Nominees

Drs. Yuri Kovalev (Russia) and Stefan Wijnholds (The Netherlands) were the two nominees for Vice Chair of Commission J. Dr. Ruan Duan (China, nominated by Prof. Dr. Yihua Yan) and Dr. Jin Fan (China, nominated

Table 1. Meetings and workshops provided with technical and/or financial support by Commission J.

Meeting	Country	Date	Support for YS
History of SKA from 1980s to 2012, Jodrell Bank	UK	April 3-5, 20219	1,000 Euros
RFI 2019 Workshop	France	September 23-26, 2019	2,000 Euros
e-Workshop at Stellenbosch and Eindhoven	South Africa and Netherlands	Planned but delayed due to COVID-19	Technical support

Table 2. A summary of the sessions and papers per session for Commission J at AT-RASC 2018.

Session	Session Topic	Papers
J1	Software Enabled Radio Astronomy	15
J2	Large N Aperture Arrays	13
J3	Pattern Recognition Applications in Radio Astronomy	6
J4	Novel Instrument Concepts and Observational Challenges	6
J5	Detecting Hydrogen Near and Far	10
J6	Instruments for Education	4
J8	Radio Telescopes	7
J9	Radio Astronomy	6
S-JB	Polarimetry of Advanced Antenna Systems in Radio Astronomy	8
S-J	Photonics in Radio Astronomy	5
S-EACFJ	Spectrum Management and Utilization	workshop

by Prof. Dr. Yihua Yan), Dr. Danielle Fenech (UK), and Dr. Lucy Oswald (UK) were nominated for Early Career Representative (ECR).

6. AT-RASC 2018 at Gran Canaria, Spain

There were 12 sessions with 80 papers presented in regular and special sessions. A workshop was also held. A summary of the sessions and papers per session is given in Table 2.

Commission J attendance was satisfactory and increased over that of AT-RASC 2015. The atmosphere of the venue made it very easy/pleasant for participants to discuss and collaborate. Travel to Gran Canaria was not so easy for some participants from the Atlantic region: the organization needs to make it easier (more transparent) the next time for those participants. The format of the AT-RASC meetings should remain flexible and should allow holding URIS-related workshops in connection with the meetings.

7. AP-RASC in New Delhi, India

From March 9 through March 14, 2019, the Asia-Pacific Radio Science Conference (AP-RASC) was held in the India Habitat Centre in New Delhi, India. Commission J had 91 oral presentations in 16 sessions and 34 posters. The Commission J keynote lecture was delivered by Ron Ekers on the topic of "Paths to Discovery in Radio Astronomy – The Role of Technical Innovation and Serendipity." Young scientists could apply for a Young Scientist Award (YSA) or take part in the Student Paper Competition (SPC). There were three applications for a YSA and two submissions for the SPC from the Commission J community. Unfortunately, none of these was successful. Table 3 summarizes the program for Commission J at AP-RASC 2019.

8. Rome, Italy, URSI GASS 2021 Scientific Sessions (Planned)

There are 141 oral talks and approximately 60 posters (FIPs) planned (see Table 4). A workshop and tutorial

Table 3. A summary of the Commission J program at AP-RASC 2019.

Session	Session Topic	Papers
J01	Evolution/latest results from the uGMRT, in honour of Govind Swarup	5
J02, J03	Updates from exiting radio astronomy facilities	11
E02, E03	RFI mitigation in radio astronomy (with Commission E)	12
J04	VLBI: current status and future prospects	6
H04	Radio science for space weather (with Commission H)	6
J09, J10	Recent scientific results on solar, solar wind and space weather observations	10
J05	Recent scientific results on Galactic, extra-Galactic star formation and transients	6
J06	The Early Universe (EoR experiments and related results)	5
J07	Future radio astronomy facilities (including SKA)	6
J11, J12	Radio astronomy instrumentation & techniques – I. Receiver systems: analog/digital/optical fibre	12
J08, J13	Radio astronomy instrumentation & techniques – II. Data processing: Imaging, Big Data	12

Table 4. The planned Commission J program for URSI GASS 2021.

Session	Session Topic	Papers
J01	New Telescopes on the Frontier	9
J02	Recent and Future Space Missions	12
J03	Single-Dish Instruments	9
J04	Very Long Baseline Interferometry	15
J05	Millimeter and Sub-Millimeter Arrays	6
J06	Antennas and Receivers: Simulation, Design and Calibration	9
J07	Digital Signal Processing: Algorithms and Platforms	6
J08	Short Duration Transients, FRBs and Pulsars: observations, techniques and instr.	15
J09	The Impact of Radio Astronomy on Technology and Society	6
J10	Latest News and Observatory Reports	6
J11	Big Data: Algorithms and Platforms	18
J12	Open Session	6
J13	Calibration Techniques and Instrumentation for Observational Cosmology	9
J-IAU	Next Generation Radio Astronomy Science and Technologies	9
JG1	Mutual Benefit between Radio Astronomy and Ionospheric Science	6

are also being organized. Note that the Student Paper Competition (SPC) was held virtually in 2020. Two students are participating in the 2021 SPC from Commission J. The unique, inter-Union session (J-IAU) will bring together the International Astronomical Union (IAU) and URSI at the GASS.

9. Communication and Membership

Discussions continued about the "average youth" of the URSI membership and the role for URSI in the life and career of the radio scientists. It is clear that URSI can be attractive for radio scientists as an organization providing places for discussions, presentations, and for meeting colleagues. While there may be some overlap in covering certain radio-science research fields with other organizations, URSI covers the broad radio science fields like no other. Still, it is important to make URSI more a part of the "daily life of the radio scientists." In addition, the new generation of radio scientists needs to be attracted to URSI. The answers to such issues are complex, but the leadership of Commission J has been discussing these issues and considering changes that may be made within URSI.

In a attempt to improve communications and raise awareness of URSI, a Commission J *Newsletter* was introduced and distributed to the membership on a monthly basis. The format includes the latest news, announcements/information on upcoming meetings, a short article highlighting research or other activities by members, and a "Photo from the Field" showing an activity or instrument. The *Newsletter* received very positive feedback. It was monthly over the first 2.5 years, but became more sporadic thereafter due to the lack of input from the membership.

Commission J participated in the discussions regarding the UTC leap second, and assisted in drafting the URSI Resolution on the need for continuous reference time scale.

Dr. Richard Bradley agreed to serve as the Associate Editor for Commission J of the URSI *Radio Science Bulletin*.

Richard Bradley
National Radio Astronomy Observatory, USA
E-mail: rbradley@nrao.edu

URSI Conference Calendar

August 2021

Bioelectrodynamics webinars
Various subjects in electromagnetics and biophysics: microwave sensors and microfluidics, molecular modelling and experimental research of electromagnetic field effects on biological systems, dielectric properties of biological material
Worldwide via Teams, recurrent webinar every 2 weeks, from June 2021 onwards
Contact : Dr. Michal Cifra & Dr. Daniel Havelka, members of the Bioelectrodynamics research team: http://bioed.ufe.cz https://bit.ly/32cUpgv , https://bit.ly/3tjjVfD , https://bit.ly/2QqqWgp

Metamaterials 2021
Fifteenth International Congress on Artificial Materials for Novel Wave Phenomena
New York, NY, USA, 2-5 August 2021 (online format)
Contact : Dr. Richard W. Ziolkowski, E-mail: contact@metamorphose-vi.org, https://congress.metamorphose-vi.org/index.php/8-general-information/1-metamaterials-20161

ICEAA - IEEE APWC 2021
22th International Conference on Electromagnetics in Advanced Applications (ICEAA 2021) and 10th IEEE-APS Topical Conference on Antennas and Propagation in Wireless Communications (IEEE-APWC 2021)
Honolulu, Hawaii, USA, 9-13 August 2021
Contact : E-mail: iceaa21@iceaa.polito.it
https://www.iceaa-offshore.org/

URSI GASS 2021
Rome, Italy, 28 August – 4 September 2021
Contact: URSI Secretariat, Ghent University – INTEC, Technologiepark-Zwijnaarde 126, B-9052 Gent, Belgium, E-mail gass@ursi.org, http://www.ursi2021.org

September 2021

Kleinheubacher Tagung 2021
Annual meeting of the Germany URSI committee
Miltenberg, Germany, 28 - 30 September 2021
Contact : Prof. Dr. Madhu Chandra, Chair of High-Frequency Engineering and Electromagnetic Theory, Faculty of Electrical Engineering and Information Technology, Chemnitz University of Technology, E-Mail: kht2021@etit.tu-chemnitz.de , https://kh2021.edas.info

October 2021

ISAP 2021
2021 International Symposium on Antennas and Propagation
Taipei, Taiwan, 19-22 October 2021
Contact : http://www.isap2021.org/

December 2021

IEEE AP-S/URSI 2021
2021 IEEE International Symposium on Antennas and Propagation and USNC-URSI Radio Science Meeting
Marina Bay Sands, Singapore, 4-10 December 2021
Contact : Secretary: Xinyi Tang aps2021.secretary@gmail.com , https://2021apsursi.org

March 2022

EuCAP 2022
16th European Conference on Antennas and *Propagation*
Madrid, Spain, 27 March - 1 April 2022
Contact : Dr. Manuel Sierra Castañer, EuCAP2022 Conference Chair, EuCAP2022 email-service@euraap.org, http://www.eucap2022.org

May 2022

AT-RASC 2022
Third URSI Atlantic Radio Science Conference
Gran Canaria, Spain, 30 May - 4 June 2022
Contact: Prof. Peter Van Daele, URSI Secretariat, Ghent University – INTEC, Technologiepark-Zwijnaarde 126, B-9052 Gent, Belgium, E-mail: peter.vandaele@ugent.be, http://www.at-rasc.com

July 2022

COSPAR 2022
44th Scientific Assembly of the Committee on Space Research (COSPAR) and Associated Events
Athens, Greece, 16-24 July 2022
Contact : GREECE COSPAR 2022 Secretariat, Fax: +30 2103643511, E-mail: info@cosparathens2022.org , https://www.cospar-assembly.org/assembly.php

September 2022

EMC Europe 2022
Gothenburg, Sweden, 5-8 September 2022
Contact : EMC Europe 2022 Secretariat: info@emceurope2022.org, Conference Chair: Prof. Jan Carlsson jan.carlsson@emceurope2022.org
https://www.emceurope2022.org/

August 2023

URSI GASS 2023
XXXVth URSI General Assembly and Scientific Symposium 2023
Sapporo, Hokkaido, Japan, 19 - 26 August 2023
Contact: URSI Secretariat, c/o INTEC, Tech Lane Ghent Science Park - Campus A, Technologiepark-Zwijnaarde 126, B-9052 Gent, Belgium, E-mail info@ursi.org

August 2025

AP-RASC 2025
Asia-Pacific Radio Science Conference 2025
Sydney, Australia, August 2025
Contact: Prof. Paul Smith, Macquarie University, Australia, E- mail paul.smith@mq.edu.au

A detailed list of meetings is available on the URSI website at http://www.ursi.org/events.php

Information for Authors

Content

The *Radio Science Bulletin* is published four times per year by the Radio Science Press on behalf of URSI, the International Union of Radio Science. The content of the *Bulletin* falls into three categories: peer-reviewed scientific papers, correspondence items (short technical notes, letters to the editor, reports on meetings, and reviews), and general and administrative information issued by the URSI Secretariat. Scientific papers may be invited (such as papers in the *Reviews of Radio Science* series, from the Commissions of URSI) or contributed. Papers may include original contributions, but should preferably also be of a sufficiently tutorial or review nature to be of interest to a wide range of radio scientists. The *Radio Science Bulletin* is indexed and abstracted by INSPEC.

Scientific papers are subjected to peer review. The content should be original and should not duplicate information or material that has been previously published (if use is made of previously published material, this must be identified to the Editor at the time of submission). Submission of a manuscript constitutes an implicit statement by the author(s) that it has not been submitted, accepted for publication, published, or copyrighted elsewhere, unless stated differently by the author(s) at time of submission. Accepted material will not be returned unless requested by the author(s) at time of submission.

Submissions

Material submitted for publication in the scientific section of the *Bulletin* should be addressed to the Editor, whereas administrative material is handled directly with the Secretariat. Submission in electronic format according to the instructions below is preferred. There are typically no page charges for contributions following the guidelines. No free reprints are provided.

Style and Format

There are no set limits on the length of papers, but they typically range from three to 15 published pages including figures. The official languages of URSI are French and English: contributions in either language are acceptable. No specific style for the manuscript is required as the final layout of the material is done by the URSI Secretariat. Manuscripts should generally be prepared in one column for printing on one side of the paper, with as little use of automatic formatting features of word processors as possible. A complete style guide for the *Reviews of Radio Science* can be downloaded from http://www.ips.gov.au/IPSHosted/NCRS/reviews/. The style instructions in this can be followed for all other *Bulletin* contributions, as well. The name, affiliation, address, telephone and fax numbers, and e-mail address for all authors must be included with

All papers accepted for publication are subject to editing to provide uniformity of style and clarity of language. The publication schedule does not usually permit providing galleys to the author.

Figure captions should be on a separate page in proper style; see the above guide or any issue for examples. All lettering on figures must be of sufficient size to be at least 9 pt in size after reduction to column width. Each illustration should be identified on the back or at the bottom of the sheet with the figure number and name of author(s). If possible, the figures should also be provided in electronic format. TIF is preferred, although other formats are possible as well: please contact the Editor. Electronic versions of figures *must* be of sufficient resolution to permit good quality in print. As a rough guideline, when sized to column width, line art should have a minimum resolution of 300 dpi; color photographs should have a minimum resolution of 150 dpi with a color depth of 24 bits. 72 dpi images intended for the Web are generally *not* acceptable. Contact the Editor for further information.

Electronic Submission

A version of Microsoft *Word* is the preferred format for submissions. Submissions in versions of T_EX can be accepted in some circumstances: please contact the Editor before submitting. *A paper copy of all electronic submissions must be mailed to the Editor, including originals of all figures.* Please do *not* include figures in the same file as the text of a contribution. Electronic files can be send to the Editor in three ways: (1) By sending a floppy diskette or CD-R; (2) By attachment to an e-mail message to the Editor (the maximum size for attachments *after* MIME encoding is about 7 MB); (3) By e-mailing the Editor instructions for downloading the material from an ftp site.

Review Process

The review process usually requires about three months. Authors may be asked to modify the manuscript if it is not accepted in its original form. The elapsed time between receipt of a manuscript and publication is usually less than twelve months.

Copyright

Submission of a contribution to the *Radio Science Bulletin* will be interpreted as assignment and release of copyright and any and all other rights to the Radio Science Press, acting as agent and trustee for URSI. Submission for publication implicitly indicates the author(s) agreement with such assignment, and certification that publication will not violate any other copyrights or other rights associated with the submitted material.

Become An Individual Member of URSI

The URSI Board of Offi cers is pleased to announce the establishment of categories of individual membership of URSI. The purpose of individual membership of URSI is to secure professional recognition of individual radioscientists and to establish their better connection with the URSI Board of Offi cers, Scientifi c Commissions, and URSI Member Committees. Three categories of individual membership (URSI Corresponding Member, URSI Senior Member and URSI Fellow) have been established.

URSI Corresponding Membership is the fi rst step into the URSI community and provides:

- Access to the proceedings of URSI Flagship Conferences via the Web site
- Notifi cations of new editions of URSI publications.

In addition, URSI Senior Members and URSI Fellows benefi t from the following:

- Reduced registration fees at URSI Flagship Meetings.
- Reduced registration fees at some meetings organized by partnering organizations such as (but not limited to) IEEE AP-S and EuCAP.
- A page charge reduction from 175 USD to 150 USD for papers published in the URSI journal, Radio Science Letters.
- An invitation to receive their individual membership certifi cate at an URSI Flagship meeting.

Fellowship is by invitation only; Senior Membership can be by invitation or application. Corresponding Membership is a streamlined, instant process. Details, and an online application for URSI Senior Membership, are available at http://www.ursi.org/membership.php#tab-sectionA1.